博士論文

Sheet Shaped Airborne Ultrasonic Phased Array for Nonlinear Effect Applications
（非線形音響用途に利用可能な
シート状空中超音波フェーズドアレイ）

神垣貴晶

Abstract

The goal of this research is to realize a thin sheet shaped airborne ultrasound phased array (AUPA) which can induce a non-linear acoustic phenomenon with high energy conversion efficiency.

A high-intensity airborne ultrasound has developed unique applications such as tactile presentation in non-contact. Existing AUPA with the piezoelectric transducer is thick and bulky. In addition, its energy conversion efficiency is not enough in practical uses. On the other hand, a capacitive type device driven with an electrostatic force ESF can achieve reducing the thickness and the high energy conversion efficiency. Existing capacitive device can not generate high-intensity ultrasound because the diaphragm with large displacement is difficult.

This paper proposes the capacitive type devices which can generate high-intensity airborne ultrasound with high energy conversion efficiency. The author organizes the problems in the capacitive type device when enhancing the diaphragm displacement to generate high-intensity ultrasound. After that, the solutions for the problems are described. In this paper, the author proposes two structure according to the solutions. In the experiments, the first proposed device emitted acoustic intensity 85 % of the piezoceramic transducer. The second proposed device emitted acoustic intensity one and half times of the piezoceramic transducer.

Acknowledgements

I have been given much thoughtful support from many people in my doctoral course and wish to thank them. First of all, I am deeply grateful to Professor Hiroyuki Shinoda who is my supervisor for 3 years in the doctoral course. His intuition for physics always impressed me and helped me to solve a lot of problems in this research.

Secondly, I am grateful to Associate Professor Yasutoshi Makino. I was indebted to the comments after the presentation at the conference etc. In addition, the quantity of his research ideas impressed me.

Thirdly, I am grateful to Akihito Noda who is now Associate Professor at Nanzan University. His sound advice and suggestions helped me over and over. In addition, his attitude towards research impressed me.

I am grateful to Keisuke Hasegawa who is now Assistant Professor at the University of Tokyo. His advice and comments encouraged me to notice the importance of seeing things deeply. Masahiro Fujiwara is now Project Assistant Professor in Shinoda-Makino laboratory. His technical advice was very clear and easy to understand. I am grateful to Yasuko Konagai who is secretary in Shinoda-Makino laboratory. She supported the laboratory members by purchasing goods and administrative procedures etc.

From here, I would like to express my gratitude to my colleagues. Yuichi Masuda is a doctoral student in the same grade and in the same lab. He is a very funny person. He has a habit of escaping from the real world when he faced problems. Thus, I worried him in each time. I spent a lot of time with Takuro Furumoto and Shun Suzuki. In addition, I spent time with Seki Inoue who already graduated from the same lab. His advice helped me when I faced problems. The above people could discuss researches and a silly talk easily. It enriched my doctoral course.

I would like to express my appreciation to the companies cooperated in this research: Toplas Engineering Co.,Ltd., ShinseiDenshiSangyo Co.,Ltd., Sogyo Co.,Ltd., Shinko Shoji Co.,Ltd., SHIN-EI SANGYO Co.,Ltd.

Finally, I would like to thank my parents.

Contents

List of Tables

List of Figures

Chapter 1

Introduction

1.1 Needs for a new type airborne ultrasound: Non-liner effect applications

Applications using nonlinear acoustic effects in the air have attracted attention and the researches have been becoming active. The applications include not only parametric speakers already in practical uses[5, 6, 7, 8] but midair tactile displays[1, 2, 9, 10], measurement instruments[11], an air flow control[12], object manipulation[13, 14]. In addition, social needs for them are increasing in recent years. Specifically, in the tactile displays, automobile manufactures such as BMW and BOSH announced concept cars with aerial touch panel at International Consumer Electronics Show 2017[15, 16].

Most devices applied for the above applications are airborne ultrasound phased arrays (AUPAs) as shown in Fig. 1.1. The typical AUPAs are composed of piezoelectric-actuated airborne ultrasound transducers which are commercially available. Since the devices are driven by electronically controlling the phases of each element, the AUPAs provide high time responsiveness.

The existing AUPAs have two practical problems. One is their thickness. The other is low electric-acoustic energy conversion efficiency. Nonetheless, these performance characteristics

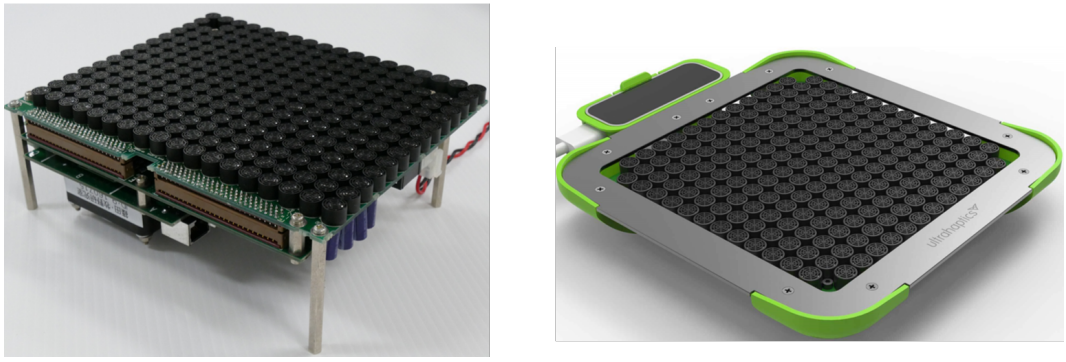

Figure 1.1: Photo of existing AUPAs. (left): Referred in [1], (right): Ultrahaptics product [2].

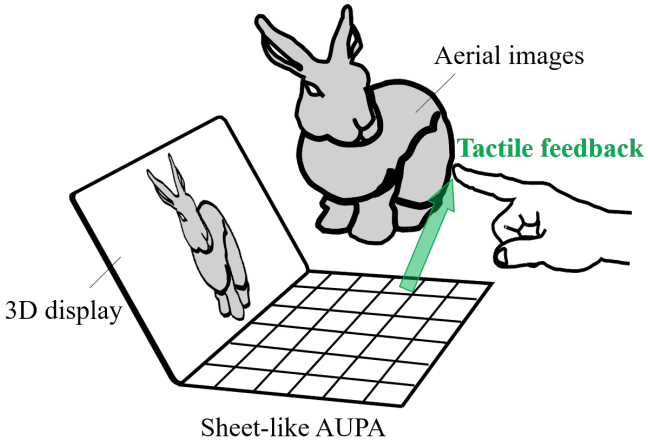

Figure 1.2: One example of a thin sheet-shaped AUPA applications.

have not made progress over the last ten years. The reason is that it is originally difficult to generate high-intensity ultrasound in the air because the acoustic load of the air is smaller than that of solid and liquid. For instance, the acoustic impedance of water, representative of liquid, is about $1.5\times10^6\mathrm{N}\cdot\mathrm{s/m}^3$ while the acoustic impedance of the air is about $400\mathrm{N}\cdot\mathrm{s/m}^3$ which is 3000 times smaller than that of water.

Reducing the thickness of AUPAs and improving the efficiency are pressing demands in order to put the above applications to practical uses and create original applications. For example, a foldable handheld mid-air visuo-tactile display as shown in Fig. 1.2 is one of potential applications combined with a glasses-free three-dimensional (3D) display. This device enables users to interact with aerial images with tactile feedback without choosing

time or place.

1.2 Current status of related technology

Many airborne ultrasound transducers have been proposed. In this section, the author classifies them by driving methods and describes their basic structures and features.

Piezoelectric type

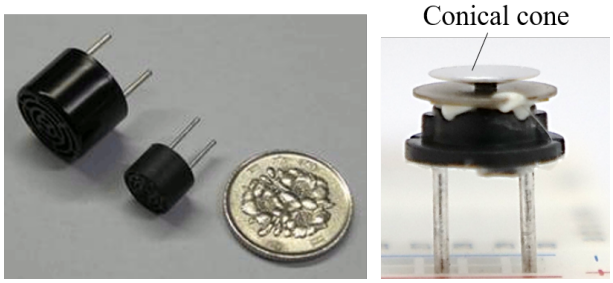

Figure 1.3: Photograph of piezoelectric type transducer applied for existing AUPA. (left): Appearance (cited from http://www.nicera.co.jp/pro/ut/ut-02.html), (right): Actual structure in the housing. The conical cone matches impedance against the air.

This type employs materials with piezoelectric properties, especially piezoceramics. This method is constituted by using electrodes and piezoelectric bodies and utilizes the transverse distortion of the piezoelectric body for generating ultrasound. Various structures such as a monomorph structure in which a piezoelectric body is attached to one side of an electrode and a bimorph structure in which a piezoelectric body is attached on both sides have been proposed. In recent years, devices based on piezoelectric Micromachined Ultrasound Transducers (pMUTs)[17] and organic transistors [18] have been proposed in order to make devices downsized and flexible.

In addition, this type can generate high-intensity airborne ultrasound by attaching impedance matching structures such as a horn, a radiation plate, and a cone[19]. The acoustic transducers used in existing AUPAs are the bimorph structure with the conical cone as shown in Fig. 1.3. Since the cone provides a resonance structure with high

Q-value, the transducers can generate high-intensity airborne ultrasound at a certain frequency. In typical transducers for AUPAs, the resonant frequency is set to about 40 kHz. On the other hand, this cone has been a bottleneck to reduce the thickness of transducers.

Capacitive type

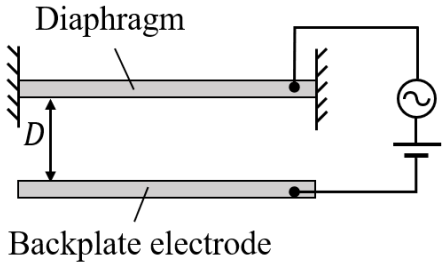

Figure 1.4: Illustration of capacitive type transducer.

This type device is basically a parallel-plate structure composed of a diaphragm and a fixed backplate electrode as shown in Fig. 1.4. This element generates ultrasound by electrostatic force (ESF) generated by applying AC voltage with DC voltage between electrodes[20, 21, 22, 23].

This type can generate ultrasound with high energy conversion efficiency without the impedance matching structure because the diaphragm is extremely thin. In addition, this type can cover broadband frequency. Thus, this type have been expected as alternative manners to piezoelectric type. However, it is difficult to generate high-intensity ultrasound in this system due to the problems described in Chapter 3, the existing device based on this type are used for sensing applications. A typical example is a condenser microphone[20]. In recent years, Capacitive Micromachined Ultrasound Transducers(cMUTs)[22] have attracted attention as suitable manners for downsizing the devices. The cMUTs can also make the devices transparent[24] and flexible[25, 26]. Phased array device with these characteristics have been proposed[27], however the time fabrication cost is high.

Thermal type

The method utilizes heat contraction and expansion of the air. One example method utilizes the thermal effect in the air of the silicon porous surface[28]. This device can generate 1 kPa sound pressure and has flat frequency characteristic up to 1 MHz, however the improvement of energy conversion efficiency is a problem. The other example for speaker utilizes graphene[29]. This device can generate complex and controllable sound signals, however the maximum acoustic emission property is out of the scope.

Electric Spark type

The method discharging between a pair of opposite electrode and generates ultrasound [30]. The instantaneous generated sound pressure was 10 Pa observed at 1 m from the device and its directivity can be regards as a point sound source. These characteristics are ideal as a sound source for sensing applications. On the other hand, this method is difficult to apply for phased array because temporal control of the frequency and the phase is hard.

Table 1.1 summarizes the characteristics of above each transducer. This table shows that sheet-shaped devices with high energy conversion efficiency to apply for the nonlinear applications have not been realized.

Table 1.1: Characteristics of existing airborne ultrasound transducer.

	Thinness	Sound pressure	Efficiency	Phase control
Piezoelectric type	○	×	×	○
Capacitive type	○	×	○	○
Thermal type	○	○	×	○
Electric Spark type	×	○	unknown	×

1.3 Purpose and contents of the paper

The purpose of this paper is to realize the sheet-shaped AUPA with a high efficiency to apply for nonlinear acoustic applications. In particular, this paper aims to use it as a tactile presentation display.

The author proposes capacitive type devices for the purpose. From Tab. 1.1, capacitive type devices are only lack of generated sound pressure. The novelty of this paper is increasing sound pressure generated in capacitive type up to either equaling to typical piezoceramic transducers applied for the nonlinear acoustic applications.

The proposed devices can be fabricated by laminating flexible materials. Therefore, the fabrication is based on flexible printed circuit (FPC) technology, which enables a low-cost fabrication and large-area fabrication easily compared with that of existing AUPAs.

This paper consists of following chapters. Chapter 2 describes nonlinear acoustic phenomena and the requirement specifications for the proposed AUPA as the tactile display. Chapter 3 reveals problems in capacitive type to increase sound pressure. Chapter 4 describes outline of solutions for each problem described in Chapter 3. Chapter 5 proposes airborne ultrasound devices with two kinds in accordance with the solutions and describes assessments of these devices.

Chapter 2

Requirements for applications

This chapter describes the principle of the tactile presentation using acoustic radiation pressure and the specifications required for the proposed AUPA as the tactile display.

2.1 Typical non-linear effects

Nonlinear acoustic effects include acoustic radiation pressure, acoustic streaming, and waveform distortion. This section describes acoustic radiation pressure utilized for the tactile presentation.

Acoustic radiation pressure P_{rad} [Pa] is induced at an object surface, when the propagation of the ultrasonic wave is disturbed by the object. P_{rad} is proportional to acoustic density and expressed as follows.

$$P_{rad} = \alpha E = \alpha \frac{p_{rms}^2}{\rho c^2} \tag{2.1}$$

where α [-] is a coefficient determined by the reflection of ultrasound on the object surface. The range of α is from 1 to 2. $\alpha = 1$ means full absorption and $\alpha = 2$ means full reflection. E [J/m^3] is acoustic energy density, p_{rms} [Pa] is the root-mean-square (RMS) sound pressure of ultrasound, ρ [kg/m^3] is the density of the air, and c [m/s] is the speed of sound in the

air. From Eq. (2.1), control of force distribution on the object surface can be achieved by controlling E because acoustic radiation pressure P_{rms} is proportional to E.

2.2 Phased array as a tactile display

The radiation pressure induced by the AUPAs can provide the tactile sensations from a remote position in a non-contact manner[9]. This method enables user to feel the tactile sensations without touching or wearing devices though presented. In addition, this method can provide the tactile sensation to many and unspecified users without a particular request [31, 32]. Note that presenting force at the skin by AUPAs is smaller than contact or wearable devices.

Existing tactile presentations with AUPAs include manners using a single stationary focal point[9, 10] or scanning it on the skin[33, 34], manners using two focal points[35], manners to present object shape using multi-focal points[36, 37], and time division method[38]. Any methods described above utilize acoustic radiation pressure at the focal point.

Therefore, let consider the case where the device, consists of N elements, forms a single focal point at a certain point in space as shown in Fig. 2.1. It is assumed that the amplitude of ultrasound waves emitted by each element is sufficiently small and linear superposition is established. The generated sound pressure of all elements is the same and let $q_i(t) = q_t e^{j(\omega t+\theta_i)}$ be the sound pressure of the i-th element at position $\boldsymbol{r_i} = [x_i, y_i, 0]$. where θ_i is a given phase to drive i-th element. Assuming that each element is a point sound source, RMS sound pressure at the position $\boldsymbol{r} = [x, y, z]$, where is on the plane parallel to the device surface, is expressed as follows.

$$p(\boldsymbol{r}) = \sum_{i=1}^{N} \frac{1}{\|\boldsymbol{r} - \boldsymbol{r_i}\|} e^{jk\|\boldsymbol{r}-\boldsymbol{r_i}\|} q_i e^{j\theta_i} A(\|\boldsymbol{r} - \boldsymbol{r_i}\|) D(\phi_i) \tag{2.2}$$

where $D(\phi_i)$ is directivity of the element, $A(\|\boldsymbol{r} - \boldsymbol{r_i}\|)$ is attenuation with propagating in the air and is expressed as following equation depending on logarithmic decay rate β [Np/m].

$$A(\|\boldsymbol{r} - \boldsymbol{r_i}\|) = e^{-\beta(\|\boldsymbol{r}-\boldsymbol{r_i}\|)} \tag{2.3}$$

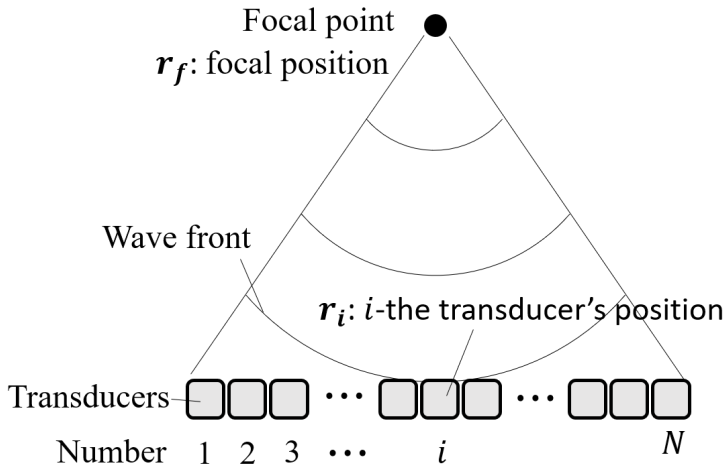

Figure 2.1: Illustration of a phased array making a focal point in the air.

β depends on the ultrasound frequency propagating in the air and its value rises with an increase of the frequency[39]. Forming the single focal point where is at $\boldsymbol{r_f} = [x_f, y_f, z_f]$ is achieved by giving θ_i as follows.

$$\theta_i = \frac{2\pi}{\lambda}\|\boldsymbol{r} - \boldsymbol{r_i}\| \tag{2.4}$$

Where λ [m] is wavelength of emitted ultrasound. The focal diameter generated by the typical AUPAs is about 10 mm as the same size as the fingertips because these device use 40 kHz ultrasound. A finer tactile presentation using the AUPAs can be achieved by using ultrasound higher than 40 kHz, e.g., 100 kHz. A device of 70 kHz has already been proposed for the purpose of finer tactile presentation[40].

2.3 Required specifications

This section describes the required specifications for the proposed AUPAs as the tactile display. First, the author describes four essential specifications and after that, describes three preferred specifications for developing the applications using the AUPAs.

The first essential specification is that the device is thin. The term ”thin” in here means

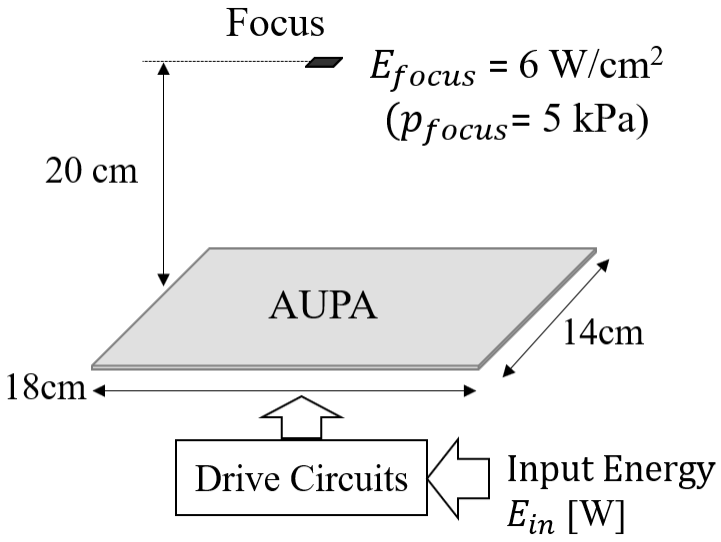

Figure 2.2: Outline figure for tactile presentation with a single existing AUPA.

thickness to be applicable for applications described in Section1.1 such as the portable device.

The second essential specification is acoustical power (or sound pressure) generated by sounder elements. In typical current researches using 40 kHz ultrasound, the acoustical power of about 6 W (RMS sound pressure is about 5 kPa) is concentrated on the area of about $1cm^2$ as shown in Fig. 2.2. The size of the existing single AUPA is 14 cm × 18 cm, and if it is simply calculated assuming that all radiation power concentrates on 1 cm^2, an acoustic output of 24 mW/cm^2 is required. This value is equivalent to 500 Pa in RMS sound pressure at 40 kHz. In order to present the tactile sensation with the AUPA, 1 kPa in the RMS sound pressure (0.24 W in acoustical power) at the focal point is needed at least[41]. In this paper, the author targets that acoustical power emitted from the proposed AUPA is equivalent to or higher than the existing one because there are individual differences in tactile perception.

The third essential specification is to improve the electro-acoustic energy conversion efficiency of the device. In the existing devices, sounder elements and driving circuits emanate heat. The suppression of the heat generation is necessary for the applications. The energy

conversion efficiency η is expressed as

$$\eta = \frac{E_{acoustic}}{E_{in}} \tag{2.5}$$

where E_{in} [W] is an input electrical power for the single device and $E_{acoustic}$ [W] is an acoustical power emitted form the device. In the existing single AUPA, η is 12 % because $E_{focus} = 6\,\mathrm{W}$, $E_{in} = 50\,\mathrm{W}$ [41]. This η is determined by the multiplication value of the energy conversion efficiency of sounder elements and that of the driving circuits. In this paper, the author targets that the efficiency of proposed AUPA is higher than that of the existing AUPA, specifically, the efficiency of the sounder element is higher than 50 %, and the driving circuit is as high as possible.

The forth essential specification is spatial resolution, that is, ultrasound frequency emitted from the device. As the author mentioned previously, spatial resolution of the existing AUPAs using 40 kHz is as same as a fingertip and higher frequency can provide a finer tactile presentation. It is considered that the upper limit of frequency is up to 100 kHz because the focal point can be localized in a fingertip. In this paper, the author targets that the device emits ultrasound in the range of 40 kHz to 100 kHz. Assuming that radiant energy from the device is constant regardless of frequencies, higher frequency makes the acoustical power at the focal point smaller, because the acoustical energy loss increases with the increase of the frequency in the course of acoustical propagation through the air. This problem can be solved by following two methods. The one is that reducing the presentation distance compared to the current device when the radiant energy from the device is as same as the existing 40 kHz device. The other is to increase radiant energy from the device than that of the existing 40 kHz device according to the increasing frequency.

The fifth essential specification is a sounder element size. A broad directivity of the sounder element is necessary because ultrasound emitted from each element must interfere in order to form the focal point. The directivity is determined by the multiplied value of frequency and element radius. The directivity becomes broader with decreasing the multiplied value. The directivity of the sounder element of the existing AUPA (T4010A1, Nippon Ceramic Co. Ltd.), whose drive frequency is 40 kHz and the 10 mm diameter, is half bandwidth

100 deg. In this paper, the author targets directivity equivalent to the sounder element of the existing AUPA at least in the case of 40 kHz.

Next, the author describes preferred specifications for the device.

The first preferred specification is an interval between the sounder elements. The interval contributes to the existence of grating lobes. The grating lobes are formed when the interval between elements is larger than the wavelength of emitted ultrasound, and are obstacles in case of generating an ideal sound field by the AUPAs. In order not to form grating lobes, the interval between elements must be lower than the wavelength.

The second preferred specification is flexible sounder elements. The existing AUPAs for nonlinear acoustic applications are rigid due to the transducers. If the device become flexible, it can ease the spatial restriction so far, and can be used in curved surfaces, e.g, curved walls.

The third preferred specification is transparency of sounder elements. If the sounder elements are transparent, it can be mounted on any device surface with the auto-stereoscopic display.

The required specifications for the AUPA as the tactile display described above are summarized below.

- Essential specifications
    1. Device thickness: thinness applicable for applications described in Section 1.1
    2. Out put acoustical power: 24 $\mathrm{mW/cm^2}$ or more
    3. Improvement of electro-acoustic energy conversion efficiency: desirable that soun -der element is higher than 50 % and driving circuit is as high as possible
    4. Ultrasound frequency: 40 kHz $\sim$ 100 kHz
- Preferred specifications
    1. Interval between sounder elements: lower than wavelength of emitted ultrasound
    2. Flexible sounder elements
    3. Transparent sounder elements

This paper proposes a sheet-shaped device which can satisfy all above specifications theoritically. As the first step, this paper aims to satisfy the above essential specifications.

Chapter 3

Problems in intensity enhancement of ESF

This chapter describes problems in the parallel-plate structure when aiming to increase generated sound pressure.

Fig. 3.1 shows the basic structure of the proposed devices. D is the air layer thickness between the diaphragm and the backplate electrode. In this parallel-plate structure, the ESF generated per unit area P_{ESF} [Pa] is expressed as follows.

$$P_{ESF} = \frac{1}{2}\varepsilon \left(\frac{V}{D}\right)^2 \tag{3.1}$$

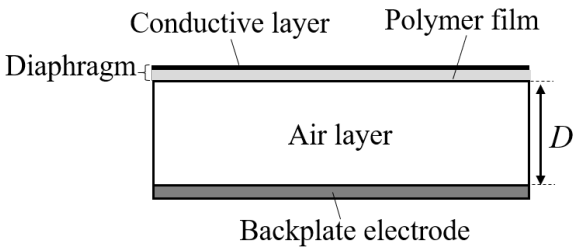

Figure 3.1: Parallel-plate structure with electrode distance D which is basic of the proposed structure.

where V [V] is the applied voltage between electrodes, ε [F/m] is the air dielectric constant. When P_{ESF} is constant and works without loss, and all of them converts to acoustic power, the maximum generated sound pressure is P_{ESF}. For example, D= 10 μm, V=300 V which is maximum applied voltage described in Section 3.1, P_{ESF} is 4 kPa. Therefore, in theoretical, capacitive type device can sufficiently generate target sound pressure e.g., 500 Pa at 40 kHz. But this sound pressure have not been achieved due to the the following problems.

Three requirements to increase generated sound pressure are as follows.

1. Strengthening the EF.
2. Suppressing energy loss in the structure.
3. Securing a diaphragm displacement.

The following each section describe the detail of the problem for each requirement.

3.1 Discharge

The generated sound pressure increases with increasing the ESF. The ESF between the diaphragm and the backplate electrode is determined by D and applied voltage because ESF depends on the square of the EF $E = V/D$. Although ESF can be increased by the increase of V when D is fixed at a certain value, the upper limit of the voltage V that can be applied between the electrodes is determined by D. If V is beyond the limit of the voltage, discharge occurs.

The discharge starting voltage V_S [V] in gases obeys Paschen's law in general. Paschen's law is based on Townsend's mechanism including impact ionization by electron (α action), electron avalanche, and secondary electron emission of a cathode (γ action). This law assumes that the EF formed between the electrodes is uniform. V_B is determined by the value multiplied gas pressure p [Pa] and the distance between electrodes D [m], and V_B is expressed as follows.

$$V_B = \frac{BpD}{ln(ApD) - lnln(1 + \frac{1}{\gamma})} \tag{3.2}$$

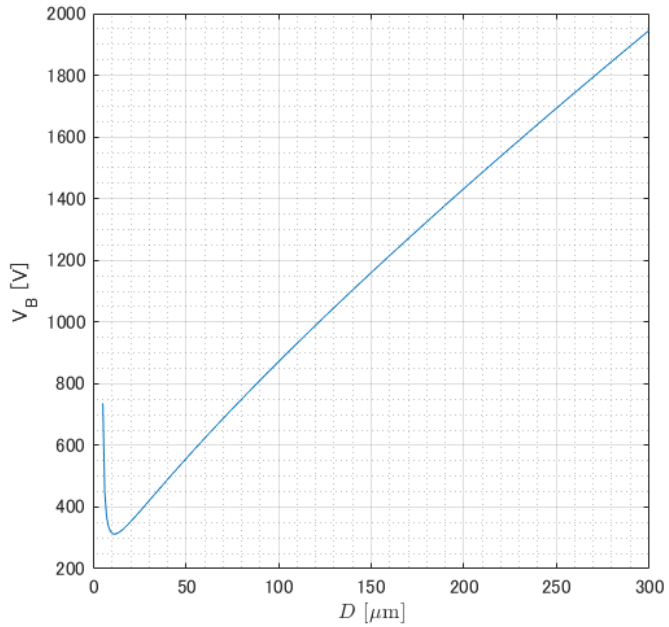

Figure 3.2: Numerically calculated discharge voltage V_B against the air gap D.

where A, B $\left[(\mathrm{Pa}\cdot\mathrm{m})^{-1}\right]$ are the constant determined by the gas between the electrodes, γ means that the number of electrons emitted from the cathode by γ action, which is a number of incident ions times γ.

Fig. 3.2 shows the result of numerical calculation based Eq. (3.2). The discharge occurs when the applied voltage between electrodes is over the voltage. Fig. 3.3 shows the EF when discharge occurs, i.e., V_B/D in Fig. 3.2. This graph shows that EF can be increased by decreasing D.

3.2 Loss in air compression

The energy loss in the structure occurs in the air layer and the diaphragm. The author ignores the loss in the diaphragm to simplify problem. The loss in the air layer is divided into viscous loss and heat conduction loss. Here, the author describes the viscous loss because it is dominant compared with the heat conduction loss as described in Appendix.

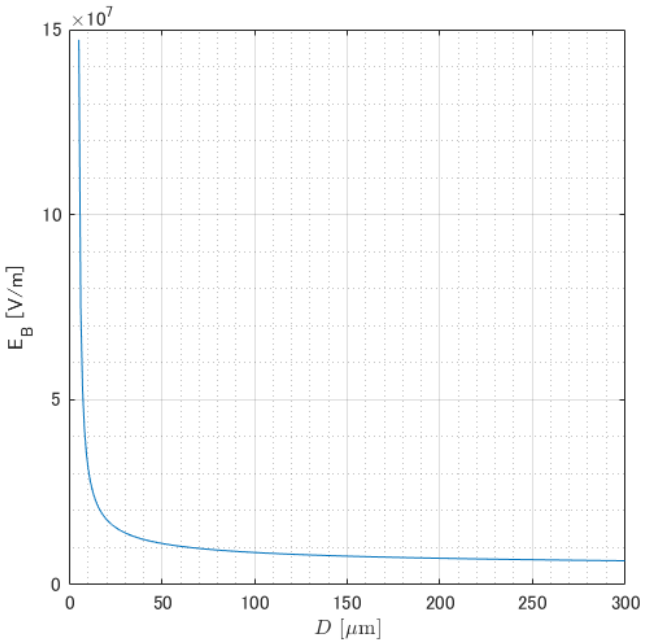

Figure 3.3: Numerically calculated discharge electric field V_B/D against the air gap D.

The theoretical upper limit value of the generated sound pressure in the parallel-plate structure is determined by the EF after getting rid of the mechanical structure impedance by constructing resonance system composed of the mass of the diaphragm and the air layer stiffness. From Fig. 3.3, EF can be increased by decreasing D within the range where no discharge occurs. On the other hand, the viscous loss in the air layer increases because the air layer needs to expand and contract with a high expansion ratio when the interval D is made extremely small without air escape place. In other words, the shear deformation of the air layer causes the viscous loss Unidirectional expansion and contraction of the air layer are a superposition of isotropic deformation and shear deformation although the air layer vibrates in the thickness direction mainly. The shear deformation of the air layer causes viscous loss. Thus, the impedance equivalent to the viscous loss remains even though suppressing apparent impedance by constructing resonance system described above. The high energy efficiency is achieved by suppressing sufficiently the impedance equivalent to the viscous loss compared with the acoustic radiation impedance ρc.

For example, D must be more than 100 μm at 40 kHz in order to set the elastic impedance

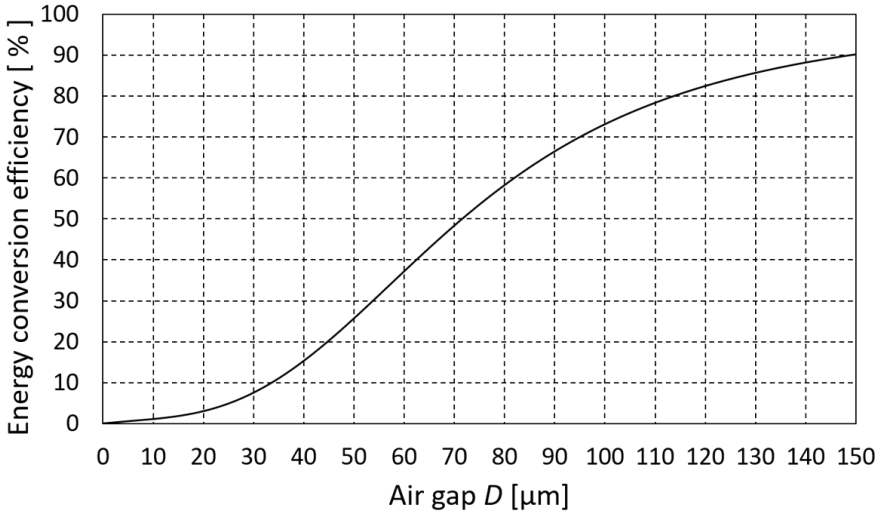

Figure 3.4: Numerically calculated energy conversion efficiency at 40kHz against a air gap D for a 6.4 mm diaphragm in diameter. This figure is the same as Fig.A.3.

of the air layer within 1/10 of ρc. In the preliminary experiments where D was more than 100 μm as described in Appendix, the emitted sound pressure was about one digit smaller than piezoceramic transducer at 40 kHz, for the same radiation area 1 cm^2. When D is set to 10 μm, ESF applied to the diaphragm can be raised to about 13 ($= 3.61^2$) times of $D =$ 100 μm. However, the electro-acoustic energy conversion efficiency η drops to 1 % at $D =$ 10 μm as shown in Fig. 3.4.

This trade-off relationship contributes to the intensity limit of the capacitive type device.

3.3 Pull-in phenomenon

The diaphragm must vibrate to generate sound pressure. The considerable problem here is a pull-in phenomenon. A pull-in phenomenon is a well-known problem in the parallel-plate structure. This phenomenon make the diaphragm immobile by sticking to the backplate electrode when applying voltage to the structure as shown in Fig.3.5. This is caused by collapsing of the force balance acting on the diaphragm at a certain point. For example, the ESF becomes lager than a reaction force generated in the diaphragm such as a restoring force due to the diaphragm rigidity.

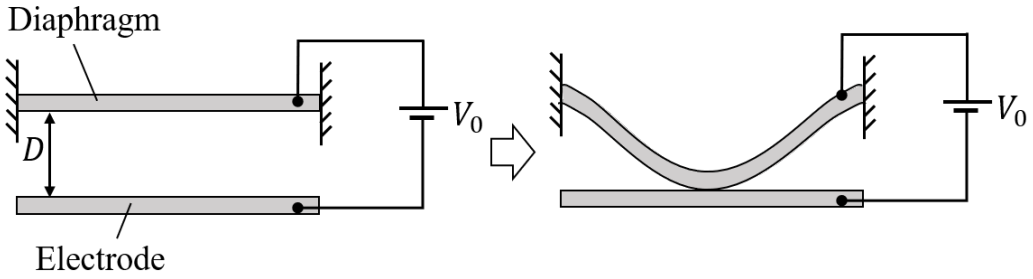

Figure 3.5: Illustration of the pull-in phanomenon. The backplate electrode is fixed and the diaphragm is supported on both sides.

In the parallel-plate structure, the pull-in occurs when the diaphragm displacement is beyond $D/3$[42]. The applied voltage at the time of pull-in is called a pull-in voltage V_{po}.

Several methods have been developed to extend the travel range of the diaphragm without the pull-in phenomenon. They are roughly divided into electrical control manners and manners by improving the mechanical structure.

In the electrical control manners, examples are restriction of charge stored in the diaphragm using an external capacitor. The method in [43] is that the capacitor C_s was inserted in series with the parallel-plate structure. Since the charge stored in the parallel-plate is smaller than that without C_s, pull-in does not occur when V_{po} is applied. This means that higher voltage is necessary to move the diaphragm and the displacement does not exceed $D/3$ in the stable condition. The other method [44] is that the capacitor C_p was inserted in parallel with the parallel-plate structure as shown in Fig. 3.6. Supposed that the parallel-plate structure with capacitance C_0 at the initial state is connected to the power supply voltage V_0 in a very short time, and is disconnected at t_1 before the diaphragm moves as shown in Fig.3.6. Since the charge stored in the system is constant, the pull-in does not occur even if the displacement exceeds $D/3$. For example, in the case of $C_0 = C_p$, the displacement is $2D/3$ without the pull-in, and pull-in voltage is $\sqrt{2}V_{po}$.

The methods improving the mechanical structure include the leveraged bending method for a polychromator [45] and the method with micro-cantilever and external electrode [46]. In the leveraged bending structure as shown in Fig. 3.7, the diaphragm can travel up to full gap without the pull-in phenomenon by generating ESF in a part of the structure. The

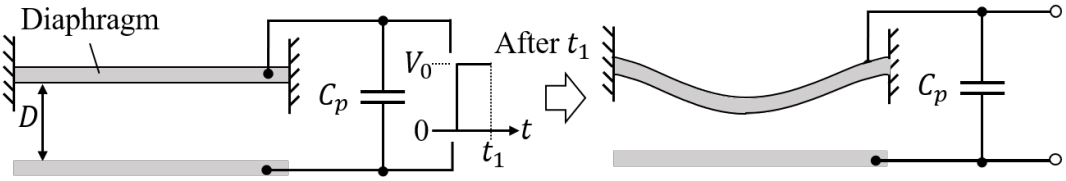

Figure 3.6: Schematic diagram of charge driving method using C_p inserted parallel with the parallel-plate structure.

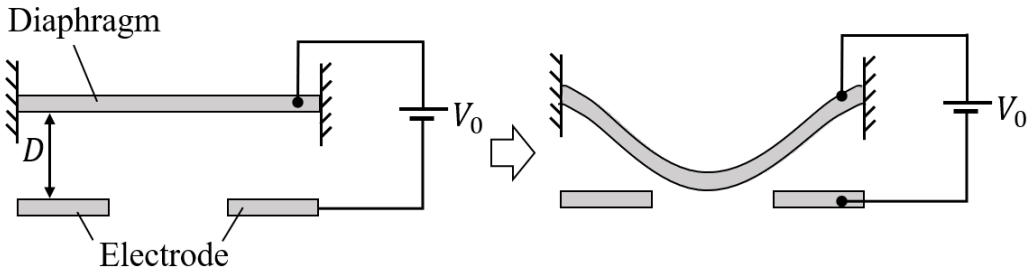

Figure 3.7: Leveraged bending method to extend the travel range of the diaphragm without pull-in phenomenon.

method with micro-cantilever and external electrode can also provide travel up to full gap without the pull-in effect.

The pull-in phenomenon is a problem as the author mentioned so far, but methods for generating ultrasound using pull-in phenomenon have been proposed[3][4] as shown in Fig. 3.8. Their methods causes pull-in phenomenon intentionally and the diaphragm contacted to the backplate electrode generates ultrasound at the end portion of the structure. The sound pressure generated by the methods is higher than that of the typical capacitive devices which does not occur pull-in, but it does not reach the target sound pressure in this paper.

Section 4.3 will propose a electric circuit concept to prevent the pull-in effect similar to the method using C_p.

3.4 Geometrical problem

In this section, the author ignores the pull-in phenomenon. The sound pressure generated is also determined by the amplitude of the diaphragm displacement. The capacive type

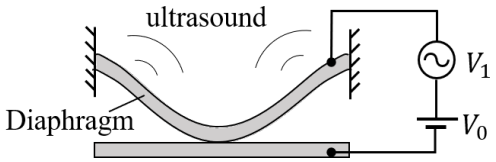

Figure 3.8: Collapse mode using pull-in. [3][4] .

device can emit 4 kPa when the diaphragm displacement is not restricted as the author mentioned. D in typical capacitive type devices with parallel-plate structure is several μm or less. Therefore, the diaphragm displacement is limited due to the structure.

The single sounder element of existing AUPA generates $|p_0| \approx 500\,\mathrm{Pa}$ at 40 kHz. Assuming that radiation impedance is ρc [$\mathrm{N \cdot s/m^3}$], the diaphragm simply oscillates with RMS vibration velocity v [m/s], and the RMS displacement of the diaphragm is ξ_0, the generated RMS sound pressure on the diaphragm surface p_0 [Pa] is expressed as follows.

$$|p_0| = \rho c v = |\rho c j \omega \xi_0 e^{j\omega t}| \tag{3.3}$$

From Eq. (3.3), ξ_0 is about 5 μm in the single sounder element of existing AUPA. Therefore, at 40 kHz, D must be more than 10 μm and the diaphragm displacement needs more than 5 μm.

Chapter 4

Outline of the solution

Table 4.1 shows correspondence between the requirements for increasing generated sound pressure and the concrete problems. This chapter describes the outline of the solution for each problems.

Table 4.1: Correspondence table between the requirements and the problems.

Requirements to increase sound pressure	Problems
Strengthening the EF	Discharge
Suppression of energy loss in the structure	Loss in air compression
Securing a diaphragm displacement	Pull-in phenomenon

4.1 Preventing discharge

The solution for prevent discharge in this paper is reducing the distance between the diaphragm and the backplate electrode. Note that the applied voltage is lower than 312 V (d = 11 μm), which is minimum voltage of V_B in Paschen's curve as shown in Fig. 3.2.

Other possible solutions is replacing the air layer with another medium. One example is flexible solids with resistant to high voltage. The flexible solids with elastic modulus comparable to air can be realized by foams having fine bubbles in principle. But such foams have not been found until the present time at least. The other examples are vacuum or

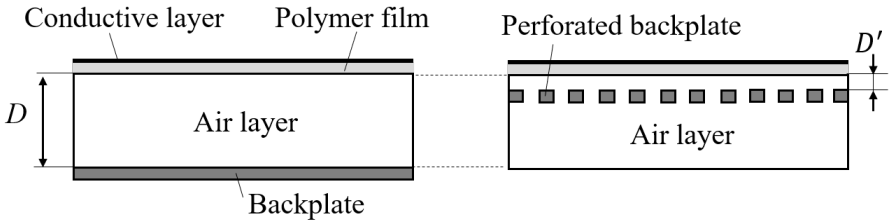

Figure 4.1: (left): Basic parallel-plate structure. (right): Proposed parallel-structure with a perforated backplate electrode.

gases with small ionization coefficient such as SF_6.

4.2 Closely aligned and perforated backplate electrode

Section 3.2 described the trade-off relationship between EF and the energy loss due to the air viscosity. In order to achieve target sound pressure, the structure which increases the EF with avoiding viscous loss is needed. The author proposes the structure with perforated backplate electrode which is closely placed on the diaphragm as shown in Fig. 4.1. The air between the electrodes can pass freely through perforations in the backplate electrode when the diaphragm vibrates. Note that the value of $D^{'}$ is to be more than the desired diaphragm displacement because generated sound pressure relates to the displacement as the author mentioned in Section 3.4.

4.3 Electrical circuit to prevent pull-in and energy loss

Preventing the pull-in phenomenon is needed to secure vibration displacement of the diaphragm. The pull-in phenomena occurs as a result of the fact that balance between ESF and the mechanical force collapses. The diaphragm displacement is basically restricted to $D/3$ as described in section 3.2. The author mentioned the method using C_p inserted parallel with C_0 which can extend the diaphragm displacement without the pull-in. In this method, stored charge does not change in the whole system composed of C_0 and C_p.

In this paper, the author proposes a driving method using only capacitor C_0 of parallel-plate

structure to prevent pull-in. Fig. 4.2 shows the temporal variation of the charge stored in the diaphragm assuming that the charging and discharging time of the electric charge is negligible with respect to the movement of the diaphragm. Fig. 4.3 shows the state of diaphragm corresponding to the electric charge state as shown in Fig. 4.2.

At the time $t = 0$, supposed that the parallel-plate structure with the initial gap D [m], area S [m^2] is connected to the power voltage V [V] in a very short time. After that the power supply disconnected before the diaphragm moves, the generated ESF F_e[N] is expressed as

$$F_e = \frac{1}{2}\varepsilon \left(\frac{V}{D}\right)^2 S \tag{4.1}$$

Here, assuming that the electric charge Q [C] generated by V is constant, the following relationship holds.

$$Q = C_0 V = \varepsilon \frac{S}{D} V = const. \Leftrightarrow \frac{V}{D} = \frac{\varepsilon Q}{S} = const. \tag{4.2}$$

Assuming a parallel-plate structure, F_e takes a constant value and is determined by D and V, although the stored electric charge should concentrate at the center of the diaphragm as the diaphragm deforms. At the time $t = T/2$, the parallel-plate structure discharge the all electric charge by shorting to the ground. Repeating the above process enables to drive the device without the pull-in phenomenon.

The proposed driving method is realized by a electric circuit. The pulse-width modulation (PWM) to drive the circuit contributes to suppression of loss in the circuit when switching during charging and discharging of the electric charge.

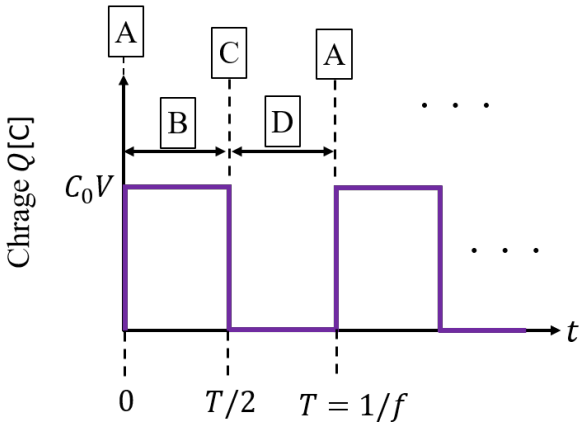

Figure 4.2: Temporal waveform of the electric charge accumulated in the diaphragm.

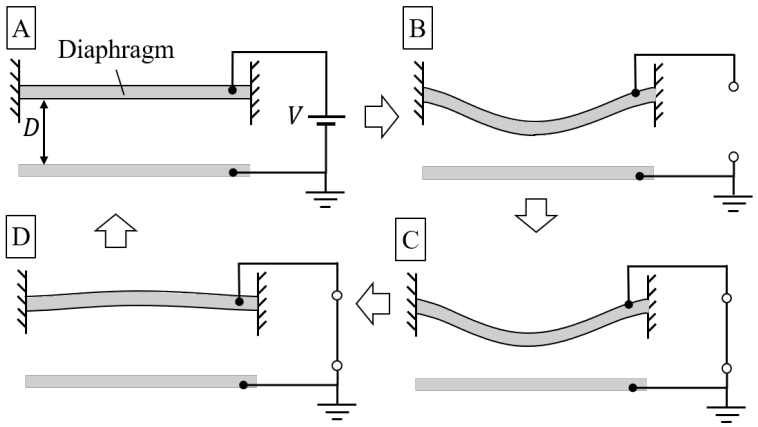

Figure 4.3: Diaphragm state corresponding to the electric charge described in Fig. 4.2. The states A, B, C, and D correspond to that in Fig. 4.2.

Chapter 5

Transducer design and results

There should be many structures that satisfy the solutions described in Chapter 4. This chapter shows two structures as examples of them. Each device adopts the solutions as shown in Table 5.1. Each device is describes respectively below.

Table 5.1: Correspondence table between the problems and the solutions.

Solutions	Proposed device type	
Decrease electrode distance	Mesh electrode type	Perforated electrode type
Perforate backplate electrode		
Driving circuit	——	

5.1 Mesh electrode type device

This section describes the mesh elctrode type device.

5.1.1 Structure

Fig. 5.1 shows the proposed structure composed of a polymer film coated with metal, a metal mesh electrode, and an insulator. The polymer film is a diaphragm with several μm-thickness. The metal mesh is made by knitting several tens of μm diameter conductive

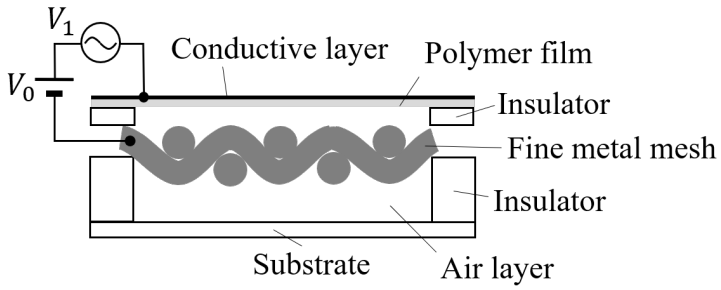

Figure 5.1: Proposed transducer with fine metal mesh electrode.

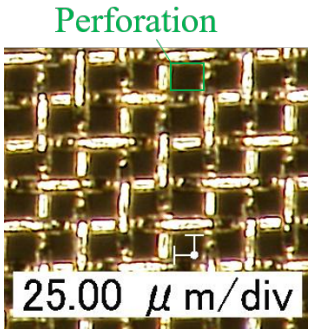

Figure 5.2: Photograph of the metal mesh used in section 5.1.3.1 and 5.1.3.

fibers as shown in Fig. 5.2, which can transfer air to the backward. This element generates ultrasound by applying AC voltage V_1 [V] with DC voltage V_0 [V].

The ESF generated by V_0 leads the diaphragm contacted to the mesh electrode. Fig. 5.3 shows the around contact point between the diaphragm and the metal mesh surface having a finite curvature. Thus, the average height of the upper mesh surface is closer than several tens of μm below the diaphragm, which generates a large ESF. At the same time, the air can travel freely through the perforations of the mesh when the diaphragm vibrates.

Note that it is still nonobvious whether the proposed structure can generate stronger sound pressure than the parallel-plate structure. The opening area cannot have the electric charge, which is a negative factor in the total ESF. In addition, the viscous and heat conduction loss around the small air gap might be considerable. Since the theoretical and numerical evaluation of these effects is not straightforward, the author fabricated the prototype transducer and experimentally evaluated the generated sound pressure and the electro-acoustic

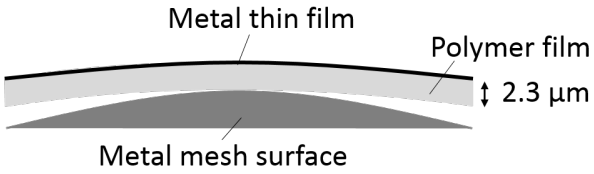

Figure 5.3: Illustration around a contact point between the diaphragm and the mesh metal surface in Fig. 5.1.

conversion efficiency.

The structure in [47] is similar to the proposed device. But this structure does not have the large gap below the mesh electrode and the maximum acoustic emission property was out of the scope.

5.1.2 Electrical circuit

Fig. 5.4 shows a proposed electrical circuit to drive the single element. The proposed circuit is composed of a Pch MOSFET, a Nch MOSFET, diodes, an inductor L, a capacitor C, and a resistor R. Since the switching of the both Pch and Nch MOSFET is conducted by PWM control and the LC resonance system is formed, the circuit realizes low-loss. C and R are equivalent to the transducer during driving, that is, the transducer itself acts as part of the drive circuit. In the mechanical structure, the value of C depends on the distance between the diaphragm and the mesh electrode. The value of R depends on the moveability of the diaphragm including on the presence or absence of wrinkles and the tension applied to the diaphragm. In order not to break the circuit, the value of L must satisfy $f \gg 1/\left(2\pi\sqrt{LC}\right)$ where f is the drive frequency.

The AC voltage V_1 applied to the transducer is generated by controlling the switch state of each MOSFET by PWM every half cycle of the drive cycle. The switch-on time of each MOSFET is set to be regarded as sufficiently long time compared with the time during the current flows to the transducer through the inductor. Diodes D_1 and D_4 connected to each MOSFET in parallel play a role to protect each MOSFET from breaking respectively when switching off the MOSFET.

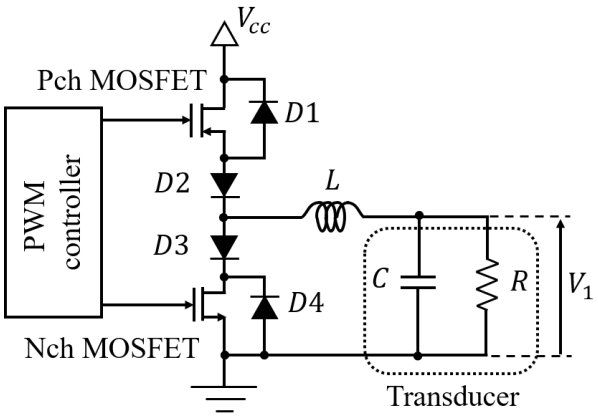

Figure 5.4: Proposed circuit. The transducer itself is used as a part of the circuit element.

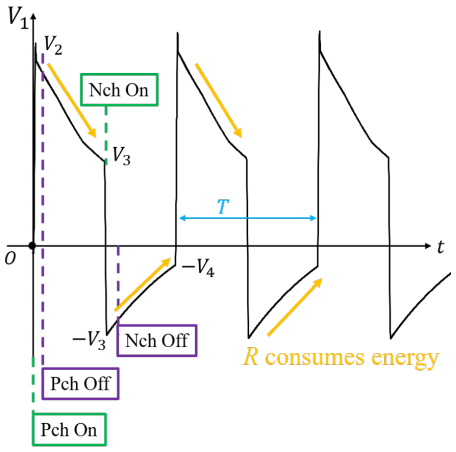

Figure 5.5: AC voltage waveform generated with the circuit in Fig. 5.4

Fig. 5.5 shows a concept of waveform generated in the proposed circuit. When only Pch MOSFET turns on, the V_1 becomes the value V_2 which doubles V_{cc} due to counter-electromotive force of the inductor when ignoring energy loss such as a wiring resistance and the MOSFET on-resistance. After turning off the switch of Pch MOSFET, V_2 is kept by diodes D_2 and D_4 when R does not exist. Since R actually exists and consumes energy stored in C, V_2 drops to V_3 until the Nch MOSFET turns on. Then, when Nch MOSFET is turned on, the value of V_3 swings to the reverse potential -V_3 due to the counter-electromotive force of the inductor. After turning off the switch of Nch MOSFET, -V_3 rises to -V_4 until the Nch MOSFET turns on for the same reason described above. The AC voltage of amplitude V_1 applied to the transducer is generated by repeating the above process.

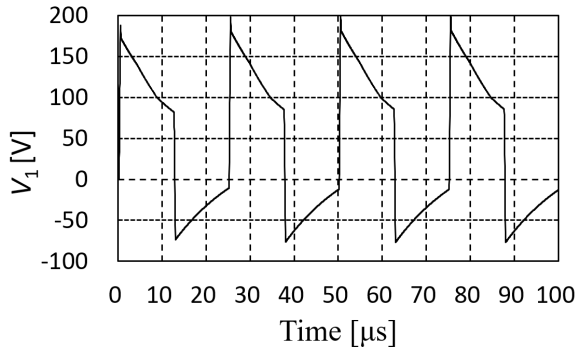

Figure 5.6: Simulation result of AC voltage generated in the proposed circuit.

The author conducted a simulation with LT SPICE. The value of the circuit element in the simulation was as same as actual manufactured one as shown in Fig. 5.14. The value of C and R are 66 pF, 270 kΩ respectively based on the value calculated from the experimental result described in Section 5.1.3. Additionally, resistors are inserted between the PchMOSFET and D_2, NchMOSFET and D_3 respectively in order not to exceed the rated current of the actually used MOSFET. The value of these resistors was set to 100 Ω because these values must be sufficiently smaller than the value of R in on order not to consume energy at the resistors. The value of inductor L was set to 220 μH and the switching on-time of both the Pch and the Nch MOSFET was set to 3.125 μs.

Fig. 5.6 shows the simulation result about voltage waveform of V_1. From this result, the proposed circuit can generate AC voltage of amplitude 150 V.

5.1.3 Evaluation of Single element

5.1.3.1 Drive element without proposed circuit

First, the author evaluated the generated sound pressure and the electro-acoustic conversion efficiency without the proposed circuit. Note that applied voltage was within the range not to discharge.

Fig. 5.7 shows the prototype transducer. The diaphragm was a gold-sputtered 2.3 μm-thick aramid film (Mictron, TORAY INDUSTRIES, INC.), and the metal mesh electrode was a

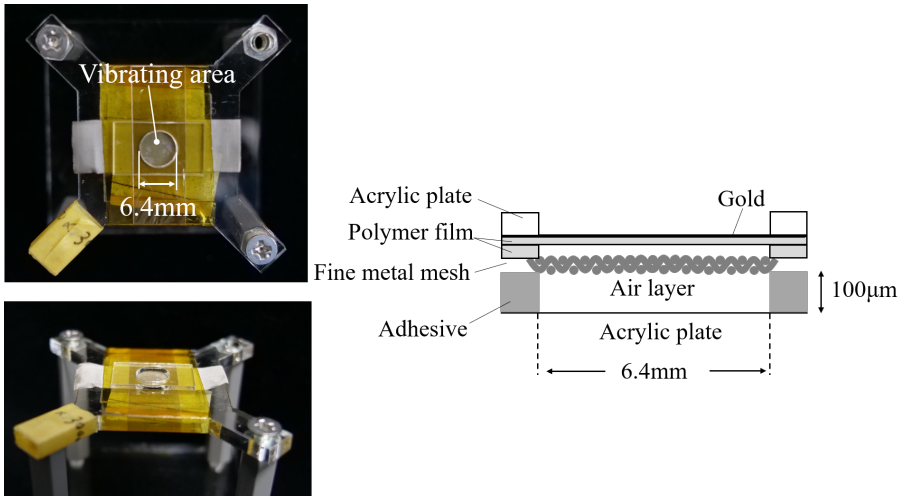

Figure 5.7: (left): Photograph of the prototype transducer. (right): Cross-section of its structure.

knit with 25 μm diameter conductive fibers and 26 μm opening (Fine Mesh #500, Sogyo Co.Ltd.). The movable part of the diaphragm was a circular area 6.4 mm in diameter. The author carefully designed the experimental setup so that sound waves from unexpected areas do not affect the measurement.

The author minimized the peripheral area where the diaphragm and the metal mesh are overlapped out of the vibration area, and such a peripheral area was covered by a 1 mm-thick acrylic plate with a 6.4 mm diameter aperture. In the peripheral area, a 12.5 μm-thick insulating film (Kapton 50EN, DU PONT-TORAY INDUSTRIES, INC.) was inserted in order to prevent unexpected discharge. For the base plate of the device, the author used an acrylic plate. The air layer thickness between the base plate and the metal mesh was set to 80 μm by using a sticky insulator (PureCell008, INOAC CORPORATION) as the spacer.

Fig. 5.8 shows the experimental setup. In the sound pressure measurement, the author used a standard microphone (4138-A015, Bruel & Kjaer) with an amplifier (NEXUS Conditioning Amplifier, Bruel & Kjaer) and the numerical RMS value displayed on an oscilloscope was visually read. To avoid the interference with reflected sound from the environments, the microphone was hung at 20 cm above the prototype transducer as shown in Fig. 5.8. The author confirmed that the reflected sound is negligible by measuring the sound pressure fluctuations with the position shift of the microphone around the original position. The

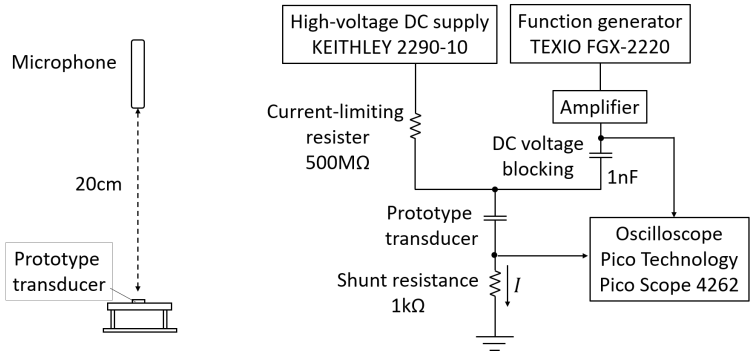

Figure 5.8: Experimental setup. (left): The microphone observes sound pressure at 20 cm from the device surface. (right): Measurement system of the phase difference between the AC voltage and the current.

electro-acoustic conversion efficiency η [%] was calculated by the effective electric power consumed at the transducer P_E [W] and vibrating velocity on the diaphragm surface v [m/s] .

$$\eta = Re\left[Z|v|^2\right]\frac{1}{P_E} \times 100 \tag{5.1}$$

$$P_E = V_{1rms} I_{rms} \cos\theta \tag{5.2}$$

where V_{1rms} [V] is the RMS amplitude of AC voltage, I_{rms} [A] is the RMS current through the transducer, θ [°] is the phase difference between V_1 and I. Note that vibrating velocity of the diaphragm is uniform in the plane. v can be obtained analytically from the measured value of spherically propagated sound field p and is given by following Eq. (5.3)[48]. p [Pa] is the measured RMS pressure obtained by the microphone at d [m] from the transducer surface, and $d = 0.2\,\mathrm{m}$ in this experiment.

$$\rho c v = \frac{p}{2\sin\frac{ka}{2}\left(\sqrt{\left(\frac{d}{a}\right)^2+1}-\frac{d}{a}\right) exp\left[j\left\{\frac{\pi}{2}-\frac{ka}{2}\left(\sqrt{\left(\frac{d}{a}\right)^2+1}+\frac{d}{a}\right)\right\}\right]} \tag{5.3}$$

where $Z[N\cdot \mathrm{s/m^3}]$ in Eq. (5.1) is a complex number and can be obtained by dividing the total sum of the forces which the diaphragm subjected from air (the integrated value of the pressure on the diaphragm surface) by the vibration velocity and is expressed as following

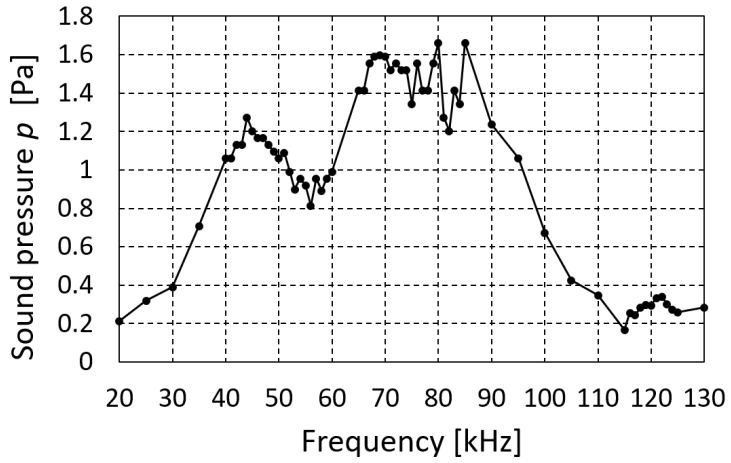

Figure 5.9: Frequency characteristic of the prototype transducer when applied DC voltage 650 V and AC voltage amplitude 15 V.

equation Eq. (5.4)[49].

$$Z = \rho c \left[\left\{ 1 - \frac{J_1(2ka)}{ka} \right\} + j \frac{S_1(2ka)}{ka} \right] \tag{5.4}$$

where ρ [kg/m^3] is the air density, c [m/s] is the acoustic velocity, a [m] is the radius of the vibrating area, k is the wavenumber of the sound, J_1 is the first-order Bessel function, and S_1 is the first-order Struve function. For example, $Z = (1.12 + 0.38\ j)\ \rho c$ when $\rho = 1.2\,\mathrm{kg/m^3}$, $c = 340\,\mathrm{m/s}$, $a = 3.2{\times}10^{-3}\mathrm{m}$, and frequency $f = 40\,\mathrm{kHz}$.

The author obtained the both waveforms of the applied AC voltage and the current by using the system as shown in Fig. 5.8 and calculated the efficiency η. Fig. 5.9 shows the obtained sound pressure p for $V_0 = 650$ V and $V_1 = 15$ V at driving frequencies from 20 kHz to 130 kHz. This result shows that the prototype transducer has low Q-value and covers a broad frequency band. Fig. 5.10 shows the phase difference θ between the AC voltage waveform and the current waveform. Fig. 5.11 shows the electro-acoustic energy conversion efficiency η calculated by Eq. (5.1), (5.2), (5.3), and(5.4). Fig. 5.11 shows $\eta = 58\,\%$ at 44 kHz.

Then, the author investigated the relation of the AC voltage to the generated sound pressure at 44 kHz, where the highest energy conversion efficiency was observed. Fig. 5.12 shows the

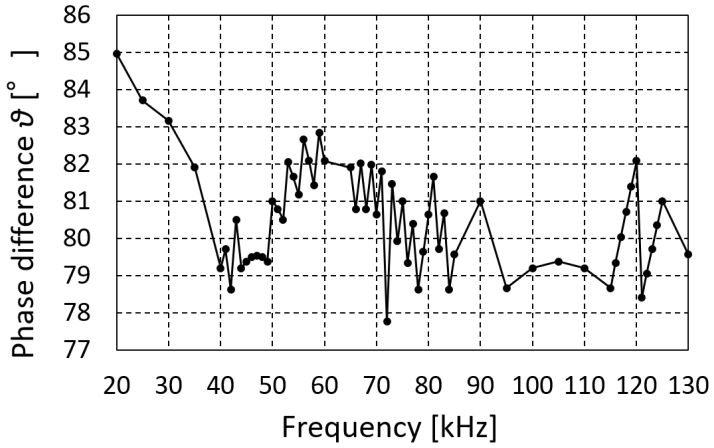

Figure 5.10: Phase difference between AC voltage and current when applied DC voltage 650 V and AC voltage amplitude 15 V.

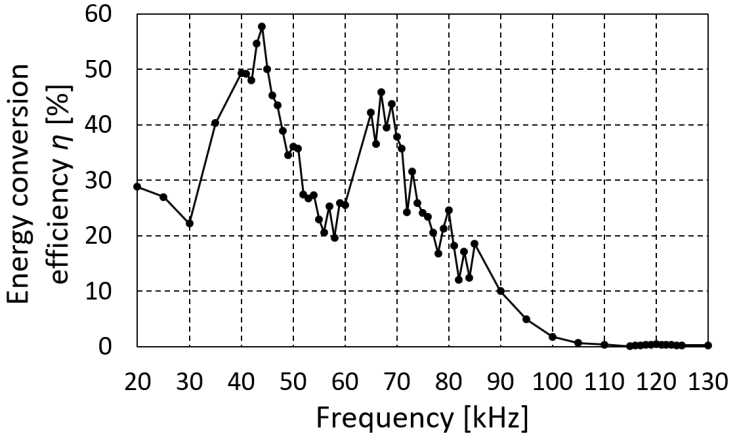

Figure 5.11: Electro-acoustic energy conversion efficiency when applied DC voltage 650 V and AC voltage amplitude 15 V.

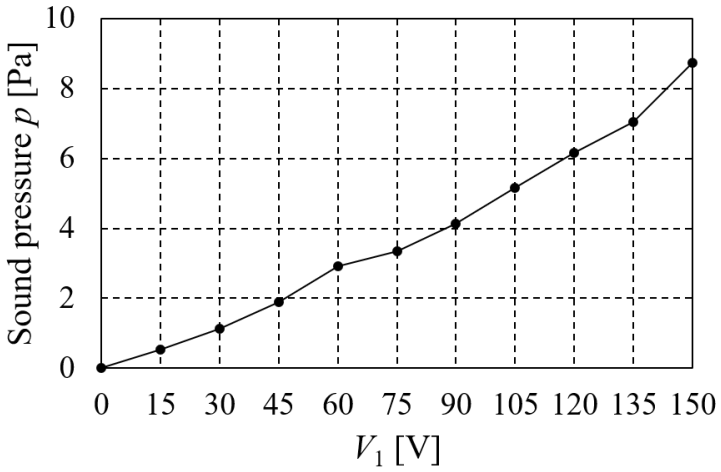

Figure 5.12: AC voltage amplitude V_1 contribution to generated sound pressure. The sound pressure was obtained at 20 cm.

measured sound pressure p for sine wave AC voltage amplitudes of V_1 from 0 to 150 V while the DC voltage was fixed to 500 V. The graph shows the maximum p was 8.7 Pa. The calculated η at this point was 55 % which was comparable to the case of $V_1 = 15$ V. This means that the energy conversion efficiency did not largely decrease for the high driving voltage.

The author obtained RMS sound pressure 21 Pa at 20 cm above the typical piezoceramics transducer with 10 mm diameter (T4010A1, Nippon Ceramic Co. Ltd.) when 40 kHz sinusoidal wave with an amplitude of 12 V was applied. Assuming that the transducer is equivalent to the diaphragm oscillating uniformly in a 10 mm circular radiation plane in diameter, the calculated result $|v|$ based on Eq. (5.3) is 1.09 times that at 44 kHz of the prototype device. The acoustic power per unit radiation area of the proposed device was calculated to be 85 % of the commercial device when this element is densely arranged and a plane wave is transmitted and assuming that the vibration speed does not change.

5.1.3.2 Drive element with proposed circuit

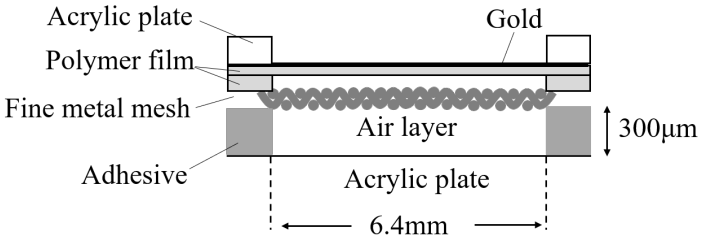

Figure 5.13: Cross-section of the prototype transducer used in section 5.1.3.2

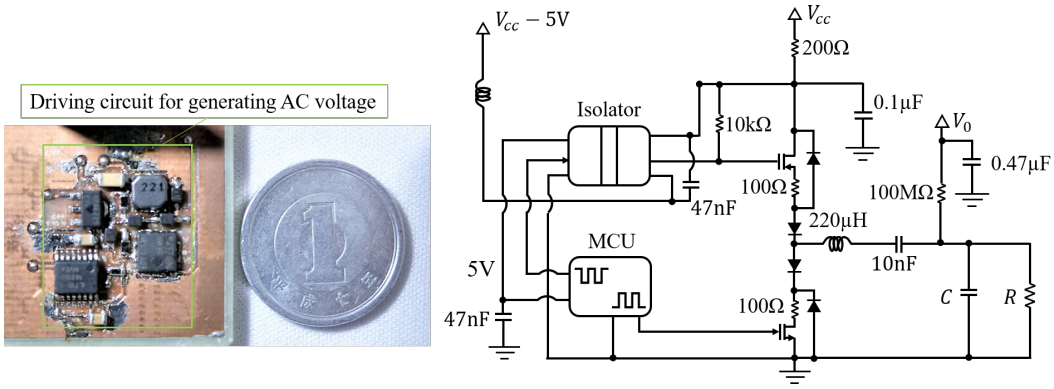

Figure 5.14: Fbaricated circuit. (left): Photo of the appearance. (left): Schematic of the circuit.

Next, the author obtained the energy efficiency of the transducer including the proposed circuit described in Section 5.1.2.

Fig. 5.13 shows the cross-section of the prototype transducer. The used materials and parameter were same as the structure described in section 5.1.3.1 except for the thickness of air layer. Fig. 5.14 shows the fabricated circuit. All electronic components were placed within 13 mm square.

First, the author confirmed the operation of the fabricated circuit by the experimental setup shown in Fig. 5.16. The circuit was driven under the same condition of the simulation described in section 5.1.2, and V_0 was 500 V. Fig. 5.15 shows the AC voltage waveform V_1 measured with an oscilloscope. This figure shows that a voltage waveform of 40 kHz has the same tendency as the simulation result. But the voltage variation when energy consumed in

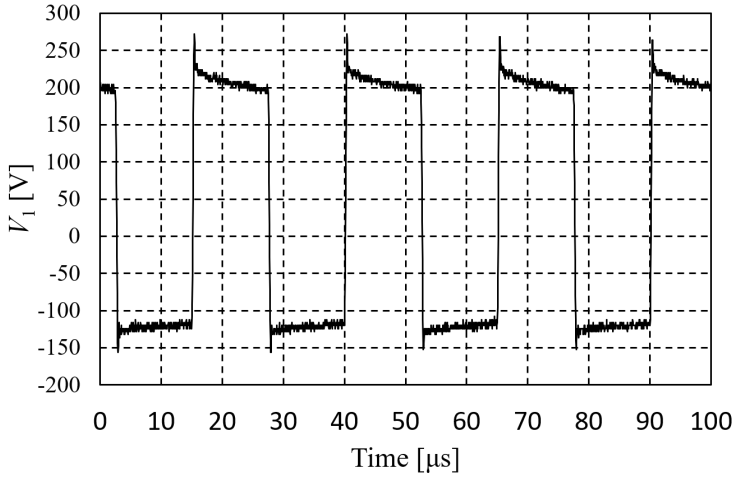

Figure 5.15: Obtained AC voltage measured at the prototype transducer.

R was smaller than that of the simulation. This means that the value of R of the transducer used in this experiment was larger than 270 kΩ. This is caused by the mechanical deflections including wrinkles in the diaphragm which arise at the time of fabricating the transducer as the author described in Section 5.1.2.

Then, the author obtained the energy efficiency of the transducer including the fabricated circuit within the range not to discharge. Fig. 5.16 shows the experimental setup. The sound pressure was obtained with an oscilloscope which connected to a standard microphone (4138-A015, Bruel & Kjaer) via an amplifier (NEXUS Conditioning Amplifier, Bruel & Kjaer). The microphone was hung at 20 cm above the prototype transducer to avoid the interference with reflected sound from the environments. The author confirmed the reflected sound is negligible by measuring the sound pressure fluctuations by the position shift of the microphone around the original position. The electric power supplied to the entire system P_E [W] was obtained by measuring the voltage drop between V_{CC} [V] and R_{sh} [Ω] placed between the fabricated transducer and GND. The author calculated P_E using the following equation.

$$P_E = \frac{1}{T}\int_0^T V_Z(t)\, I(t) dt = \frac{1}{T}\int_0^T \left(V_{CC}(t) - \Delta V(t)\right) \frac{\Delta V(t)}{R_{sh}} dt \tag{5.5}$$

where T [s] is the driving cycle, V_Z [V] is the voltage drop in the system composed of the

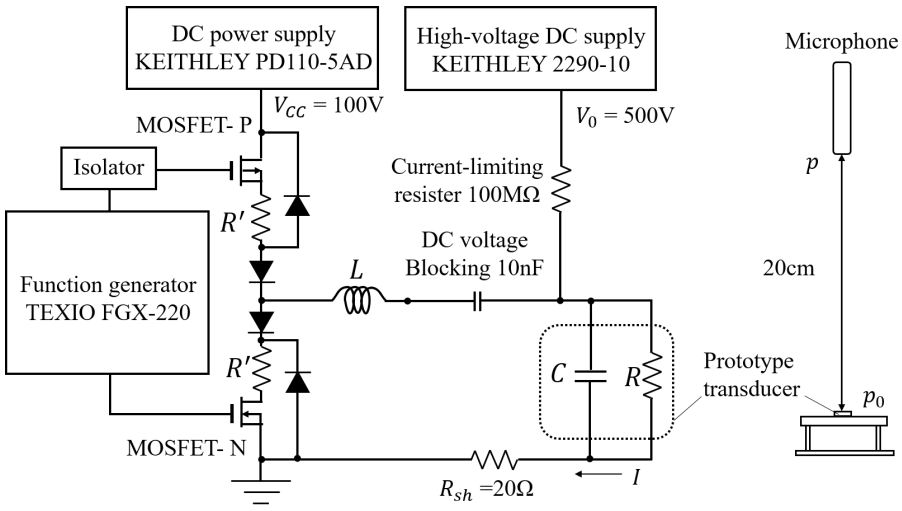

Figure 5.16: (left): Measurement system of electric power supplied to the entire system. (right): Measurement system of sound pressure.

circuit and the transducer, I [A] is the current. R_{sh} was 20 Ω in order to be $V_Z \gg \Delta V$. The circuit was driven under the same condition when confirming the operation of the fabricated circuit.

Fig. 5.17 shows the voltage waveform of V_Z. Fig. 5.18 shows the obtained voltage waveform at R_{sh}. P_E obtained from Eq. (5.5) were 15.4mW. At the same time, the author obtained $p = 5.9$ Pa. From Eq. (5.1), Eq. (5.3), and Eq. (5.5), the author obtained 37 % energy conversion efficiency including the fabricated circuit. In addition, the author confirmed that the fabricated circuit did not emanate heat even if it continued to drive for 3 hours.

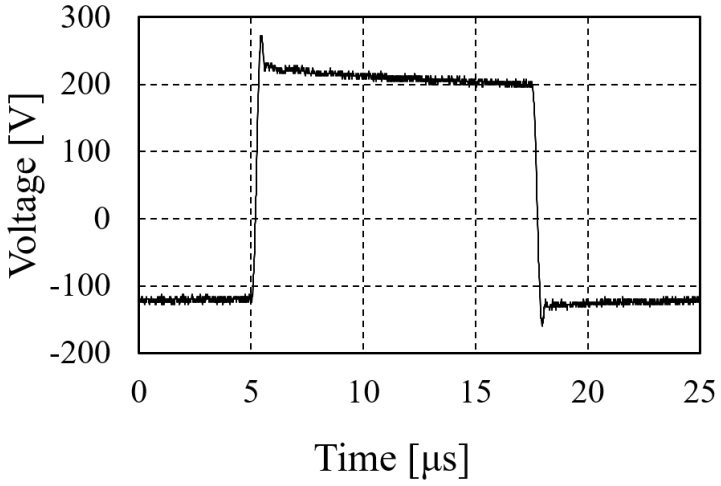

Figure 5.17: Obtained voltage waveform of V_Z.

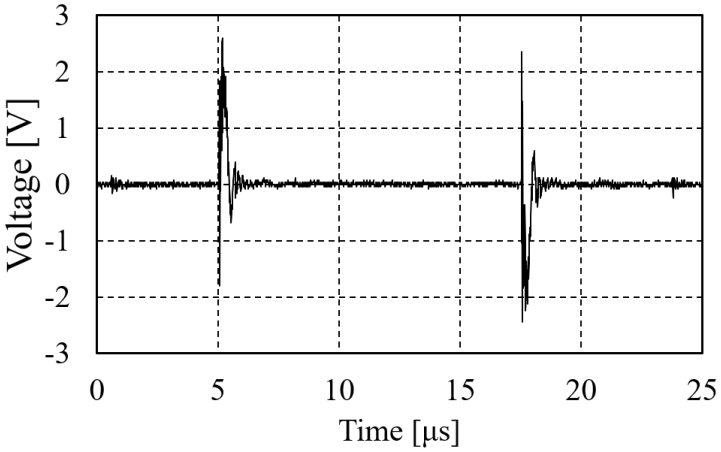

Figure 5.18: Obtained voltage waveform at R_{sh}.

5.1.4 Evaluation of phased array device

As a prototype, the author fabricated an 8×8 AUPA integrated with the structure with the metal mesh electrode and the proposed circuit, and measured a sound pressure distribution to observe a focal point of ultrasound. Note that the diameter and driving frequency of each element of fabricated AUPA are 10 mm-square and 40 kHz by reference to the piezoceramic transducer for AUPA (10 mm in diameter, 40 kHz).

Fig. 5.19 shows the actual appearance and Fig. 5.20 shows the prototype structure. The device is realized by laminating a series of polymer films with conductive layer on a substrate where the metal mesh electrodes corresponding to each element are dispersedly arranged. The substrate has the electrodes corresponding to each element on its front surface and the driving circuits for each element are provided on the back surface. These materials are bonded with sheet-adhesive. Each element generates ultrasound by applying AC voltage of amplitude V_1 with DC voltage V_0 between the diaphragm and the metal mesh electrode. The sound field generated by the device is determined by phase ϕ_i of V_1 applied to each element. The voltage supply to each metal mesh electrode is realized by contacting the mesh electrode to the electrode on the substrate surface where a superposed voltage of V_0 and V_1 appears via a conductive material such as a copper pin or silver paste.

The fabricated device is composed of two rigid substrates (substrate$A$, substrate$B$). The substrate$A$ has electrodes corresponding to each element on its front and back surface. The electrode size in both substrates is 10 mm-square . Copper pins (copper pillars, FINES CO., LTD.) with a 150 μm diameter and a 300 μm height are mounted on each electrode on the substrate one side and the author fabricated the element structure on this side. The diaphragm was a platinum-sputtered 2.3 μm-thick aramid film (Mictron, TORAY INDUSTRIES, INC.). The reason of changing from gold-sputtered in the previous experiments to platinum-sputtered was to prevent migration effect when applying voltage. The metal mesh electrode was knitted with 16 μm in a diameter conductive fibers and its perforations was 16 μm. The conduction between the electrode and the metal mesh was realized by hand soldering the copper pin and the mesh electrode. In addition, the author fabricated the frame which can apply tension to the diaphragm and hold it in order to prevent wrinkles

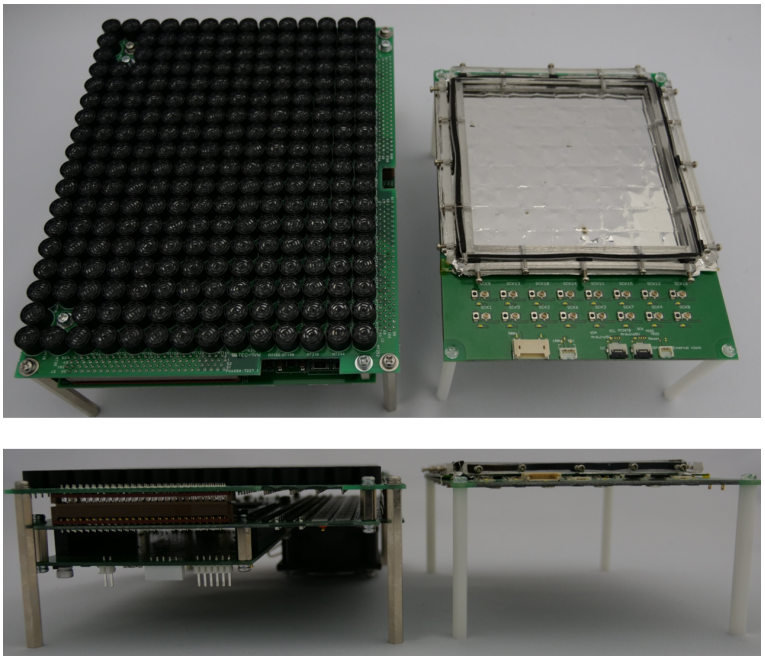

Figure 5.19: (left): Photo of the existing AUPA. (right): Photo of prototype device.

in the diaphragm. These materials are bonded with sheet-adhesive. The substrate$B$ has an electrode pattern of the same size at the same position as the substrate$A$ on one side and the driving circuit shown in Fig. 5.21 placed on the back side. The driving circuit with high density was achieved by making the substrate$B$ with an 11-layer. The device was fabricated by laminating the substrate$A$ with the element structure and the substrate$B$ with a conductive sheet-adhesive on each electrode.

Fig. 5.22 shows the experimental setup. The center of the prototype device was the measurement system origin $O\,(x, y, z)$ = (0, 0, 0 mm), and the device was driven to make a focus at a point (x, y, z) = (0, 0, 200 mm). The sound pressure distribution was measured by scanning the standard microphone (4138-A015, Bruel & Kjaer) attached to the 3-axis stage (OSMS26-300, SIGMAKOKI CO.,LTD.) to the x - y plane where z = 200 mm. The measurement resolution was 1 mm in the both x and y directions, and the measurement region was -40 mm $\leq x$, $y \leq$ 40 mm. The circuit was driven at the condition of V_0= 250 V, V_{CC} = 30 V in Fig. 5.14 and the signal to drive each element was determined by considering the responsiveness of each element to the input signal. In particular, the responsiveness was

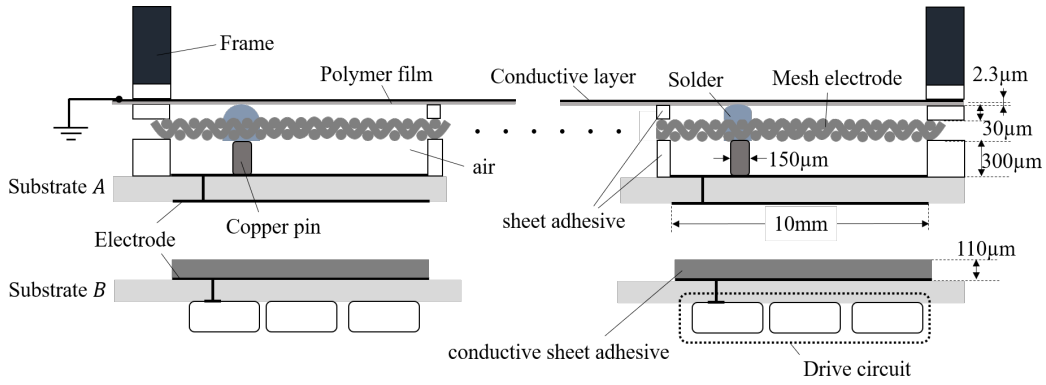

Figure 5.20: Cross-sectional view of the 8×8 phased array prototype using metal mesh electrode.

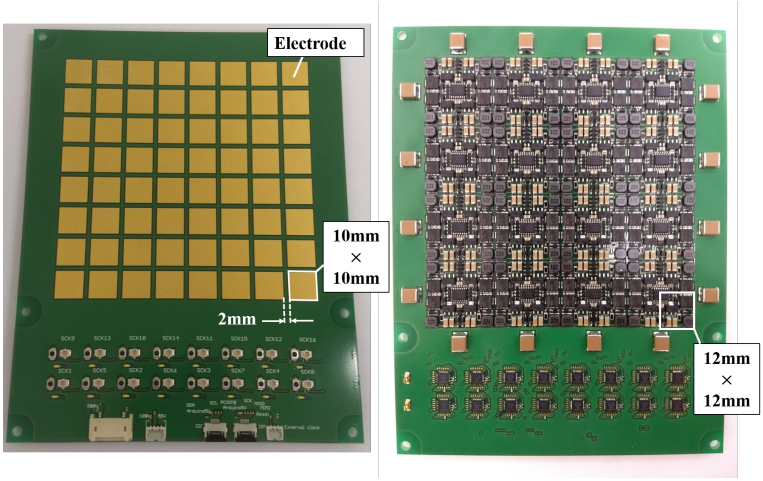

Figure 5.21: Photo of substrate B. The left one is the upper surface with electrode corresponding to each element, and the right one is the lower surface with drive circuit of each element.

calculated by the quadrature detection of the obtained temporal waveform and the temporal waveform which was to be acquired at the focal point scheduled position calculated from the input signal to the element.

Fig. 5.23 shows the experimental result. The maximum sound pressure was 9.7 Pa at $(x, y, z) = (6,\ 4,\ 200\,\mathrm{mm})$. The deviation of the focal position was thought to be due to the temporal change of responsiveness in each element. Fig. 5.24 shows the result of the phase difference of observed sound waves against the input signals of four elements randomly selected from the prototype device. This result suggests that the responsiveness to the input signal to the element tends to increase with the lapse of time. In addition, 45 hours after the first measurement, the deviation of the phases was from 4 % to 10 % of the driving frequency. From the above, the deviation of the focal position is caused by the difference in responsiveness between the element at the time of determining the driving signal and that at the time of forming the focus. In other words, the phase of the driving signal required for forming the focus was thought to be incorrect.

Furthermore, the actual obtained sound pressure was one digit smaller than 150 Pa (= 2.4 Pa×64 element which was to be obtained at the focus when assuming that the element directivity was ignorable. What though to be the cause is the reproducibility of the mechanical structure in each element such as the deviation of the electrode distance and of the diaphragm mobility. There were many elements in which the insulator surface of the diaphragm was not in contact with the mesh electrode during operation of the device. The ESF in this state drops compared to the single element described in Section 5.2 because of increasing the electrode distance. In addition, the diaphragm mobility in each element was though to be different because the tension applied to the diaphragm was anisotropic. These factors contribute to the reduction of the value of C, R, and V_1 in the circuit. As a result, generated sound pressure decreases.

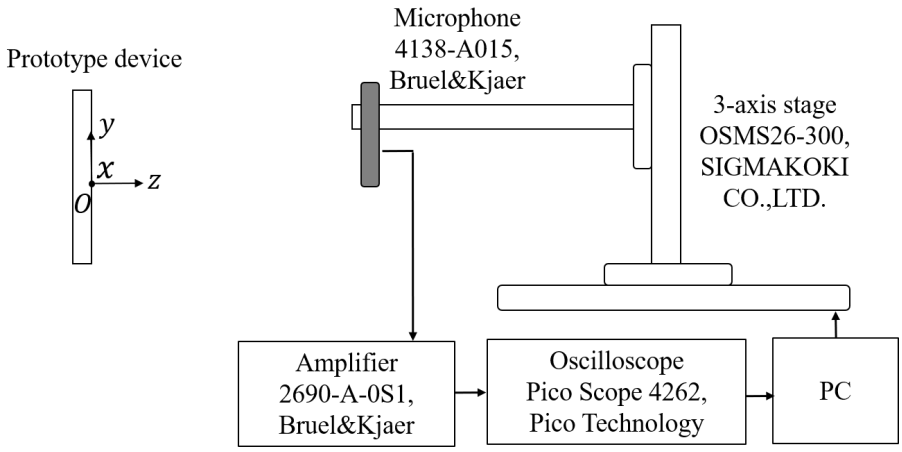

Figure 5.22: Schematic of experimental setup for measuring sound pressure distribution.

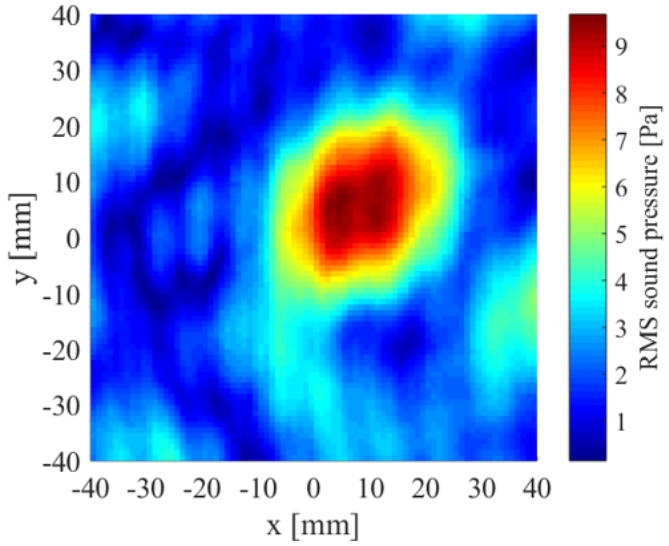

Figure 5.23: Measured sound pressure distribution at z =200 mm, when the device was driven to generate a focus at (x, y, z) = (0, 0, 200mm).

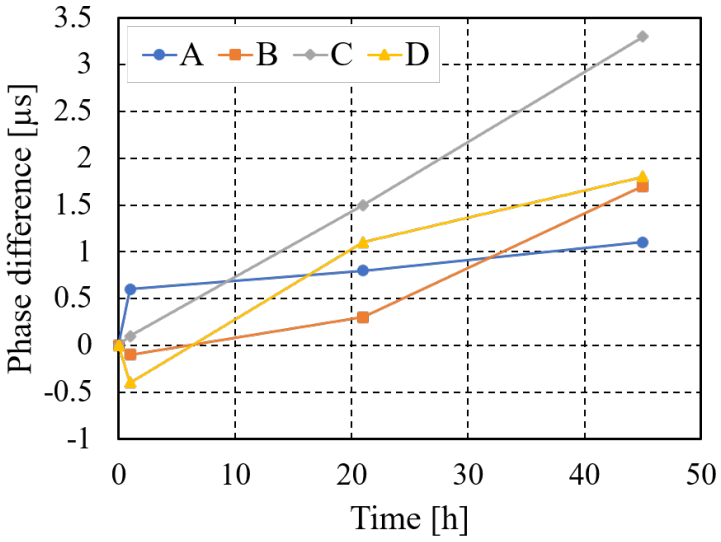

Figure 5.24: Experimental result on time variation of responsiveness to the input signal of 4 elements randomly selected from prototype devices, which were measured 1 hour, 21 hours, 45 hours after the first measurement.

5.1.5 Conclusion

In this section, the author proposed the structure using the metal mesh electrode with perforations where the air can travel freely. Although the mechanism of generating sound is not clarified, the author confirmed the effectiveness of the proposed method in a single element experiment. The experiment with the phased array device consisted of the mesh electrode revealed that the reproducibility of the mechanical structure in each element is a problem.

5.2 Perforated backplate electrode type device

In this section, the author proposes the structure with a perforated backplete electrode for the practical use.

5.2.1 Structure

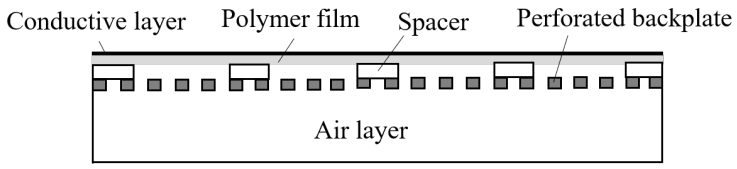

Figure 5.25: Cross-sectional view of the proposed structure of a single element.

Fig. 5.25 shows a proposed single element structure. This structure is realized by arranging periodically repeated spacers in one direction between a series of a polymer film with a conductive layer and the perforated backplate electrode. The polymer film as the diaphragm is fixed at the places contacted with the perforated backplate surface. The distance between the diaphragm and the backplate electrode surface is 10 μm to ensure the diagphram displacment when assuming the driving frequency is 40 kHz as described in Section 3.4. The air layer thickness on the back of the backplate electrode is the several 100 μm.

Although many structures with perforations provided in the diaphragm or the back plate have been proposed, they have been applied to sensing applications[23, 50]. Thus, the structure with perforations applicable for non-linear acoustic applications have not existed.

5.2.2 Dynamics

The proposed structure generates ultrasound by applying AC voltage. In order to prevent the pull-in phenomenon, the AC voltage generated from the driving circuit repeats charging/discharging the electric charge every half period of the driving frequency as described in Section 4.3. Note that the charging and discharging time is ignorable against the diaphragm movement.

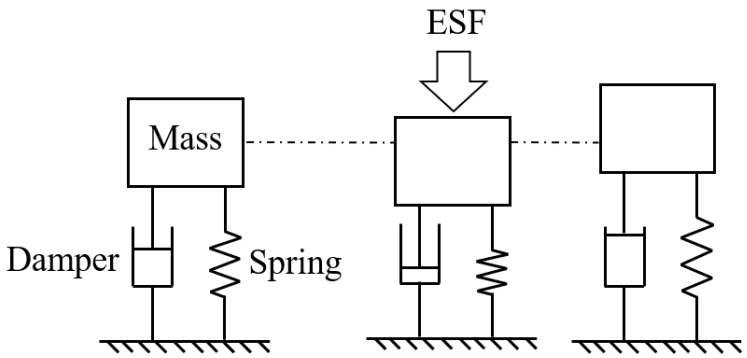

Figure 5.26: Equivalent mechanical system model to the proposed structure.

Here, the author describes the dynamics about one period in the structure. Assuming that all patterns in the element move synchronously against the applied AC voltage and that the same pattern continues in the depth direction for the sake of simplicity. The structure size is $L_m \times W$(width $\times$ depth).

First, the electric charge is stored in the diaphragm when applying V_1 between the diaphragm and the backplate electrode and stopping the supply of the electric charge. The electric charge stored in the diaphragm Q_0 is determined by the initial gaps D and V_1. The diaphragm is attracted by the ESF generated by Q_0. Then, discharging Q_0 by shorting between the diaphragm and the ground at the half period of the drive cycle, the diaphragm travels to the upper with restoring force acting on the diaphragm such as the diaphragm stiffness or the applied tension in the case of applying tension to the diaphragm. The structure generates ultrasound by repeating the above cycle.

Fig. 5.26 shows a mechanical system model expressing the above dynamics. This model consists of a mass, a spring, and a damper. The external force is ESF and it induces the vibration of the mass. The mass in the model is the diaphragm mass. The spring constant is determined by the air layer stiffness, the flexural rigidity, and the applied tension in the case of applying tension to the diaphragm. The attenuation coefficient of the damper is the sum of radiation impedance ρc and the air layer impedance in the structure. In order to achieve high efficiency, the value of the air layer impedance is necessary to be sufficiently smaller than ρc.

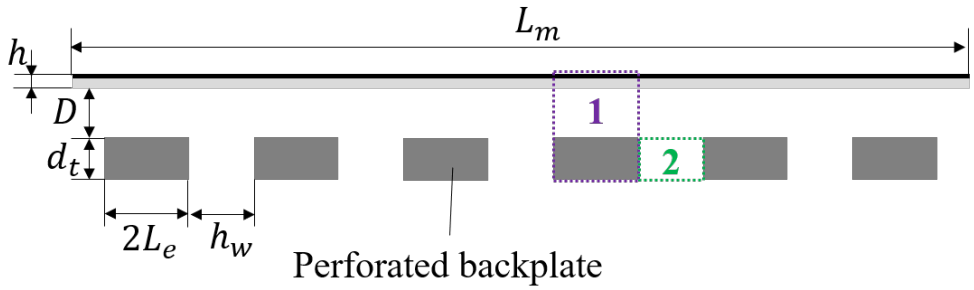

Figure 5.27: Cross-sectional view between the diaphragm and the perforated backplate electrode in Fig. 5.25.

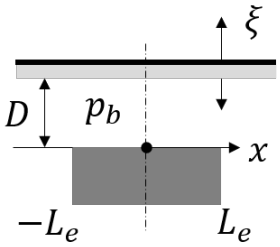

Figure 5.28: Enlarged illustration of the part1 in Fig. 5.27.

The air layer impedance can be designed by theoretical consideration. There are two air layer impedance to be considered as shown in Fig.5.27 assuming that the same pattern continues in the W direction for simplicity. One is Z_{AL} in the air layer between the diaphragm and the backplate electrode, where is part1 in Fig.5.27. The other is Z_t in the perforations where air travels through and part2 in Fig. 5.27.

First, the author describes Z_{AL}. Fig. 5.28 is an enlarged view of 1 in Fig. 5.27. Assuming that the diaphragm is a rigid plate and vibrates in the simple harmonic with the displacement amplitude ξ_0 [m]. The forced vibration equation in here is expressed as follows.

$$\left\{\frac{\partial^2}{\partial x^2} - \frac{\lambda}{\kappa}\Gamma(\beta))\right\} p_b = -\frac{\lambda}{D}\Gamma(\beta)\xi_0 e^{j\omega t} \tag{5.6}$$

where $\lambda = j\omega$, ω [rad/s] is an angular frequency, κ [kg/(m $\cdot$s^2)] is a bulk modulus of the air, and p_b [Pa] is the pressure in the air layer when the diaphragm vibrates. Boundary

conditions is as follows.

$$p_b|_{x=L_e} = 0 \tag{5.7}$$

$$\frac{\partial p_b}{\partial x}|_{x=0} = 0 \tag{5.8}$$

Let be a one-dimensional solution in Eq. (5.6) as follows.

$$p_b(x,t) = \left\{ Ae^{kx} + Be^{-kx} + \frac{\kappa}{D}\xi_0 \right\} e^{j\omega t} \tag{5.9}$$

Here, k and β are

$$k^2 - \frac{j\omega}{\kappa}\Gamma(\beta)) = 0 \Leftrightarrow k = \sqrt{\frac{j\omega}{\kappa}\Gamma(\beta)} = \frac{1+j}{\sqrt{2}}\sqrt{\frac{\omega}{\kappa}\Gamma(\beta)} \tag{5.10}$$

$$\beta \equiv D\sqrt{\frac{\rho\lambda}{\mu}} = D\sqrt{\frac{j\omega\rho}{\mu}} \tag{5.11}$$

where μ is a viscosity coefficient, and $\Gamma(\beta)$ can be approximated by $\Gamma(\beta) = \frac{12\mu}{D^2}$ in the case of $|\frac{\beta^2}{10}| \ll 1$. When $\rho = 1.2$ kg/m^3, $\mu = 1.8\times10^{-5}$ Pa·s, and $f = 40$ kHz, $\beta = 0.13$ in the case of $D = 1\times10^{-6}$ m and $\beta = 1.3$ in the case of $D = 10\times10^{-6}$ m. Thus, Eq. (5.10) can be approximated by

$$k = \frac{1+j}{\sqrt{2}}\frac{1}{D}\sqrt{\frac{12\mu\omega}{\kappa}} \tag{5.12}$$

From Eq.(5.7),

$$p_b|_{x=L_e} = Ae^{kL_e} + Be^{-kL_e} + \frac{\kappa}{D}\xi_0 = 0 \Leftrightarrow Ae^{kL_e} + Be^{-kL_e} = -\frac{\kappa}{D}\xi_0 \tag{5.13}$$

From Eq. (5.7) ,

$$\frac{\partial p_b}{\partial x}|_{x=0} = kA - kB = 0 \Leftrightarrow A = B \tag{5.14}$$

From Eq. (5.14), Eq. (5.13) is expressed as

$$A\left(e^{kL_e}+e^{-kL_e}\right)=-\frac{\kappa}{D}\xi_0 \tag{5.15}$$

Assuming $kL \ll 1$, Eq. (5.15) is approximated as

$$A=-\frac{\kappa}{2D}\xi_0\left\{1-\frac{(kL_e)^2}{2}\right\} \tag{5.16}$$

From Eq. (5.16), Eq. (5.9) is rewritten as

$$p_b(x,t)=\frac{\kappa}{D}\xi_0\frac{k^2}{2}\left(L_e^2-x^2\right)e^{j\omega t} \tag{5.17}$$

From Eq. (5.10), Eq. (5.17) is expressed as

$$p_b(x,t)=\frac{6j\omega\mu\left(L_e^2-x^2\right)}{D^3}\xi_0 e^{j\omega t} \tag{5.18}$$

The average sound pressure $\bar{p_b}$ in the part1 is expressed as follows.

$$\bar{p_b}=\frac{1}{L_e}\int_0^{L_e}p(x,t)dx=j\frac{4\mu\omega L_e^2}{D^3}\xi_0 e^{j\omega t} \tag{5.19}$$

The relationship between $\bar{p_b}$ and impedance Z_{AL} is expressed as following.

$$\bar{p_b}=j\omega Z_{AL}\xi_0 e^{j\omega t} \tag{5.20}$$

Since $\bar{p_b}$ in Eq. (5.19) is equal to that in Eq. (5.20), Z_{AL} is derived as

$$Z_{AL}=\frac{4\mu L_e^2}{D^3} \tag{5.21}$$

Fig. 5.29 shows the numerically calculation result based on Eq. (5.21) about the ratio of Z_{AL} and ρc. The value of the contour on the graph $log_{10}\left(Z_{AL}/\rho c\right)=0$ means that Z_{AL} is equal to ρc. For instance, when $L_e=25\,\mu$m and $D=5\,\mu$m, 50 % of energy is consumed in this part. The smaller ratio value is desirable in order to achieve high efficiency.

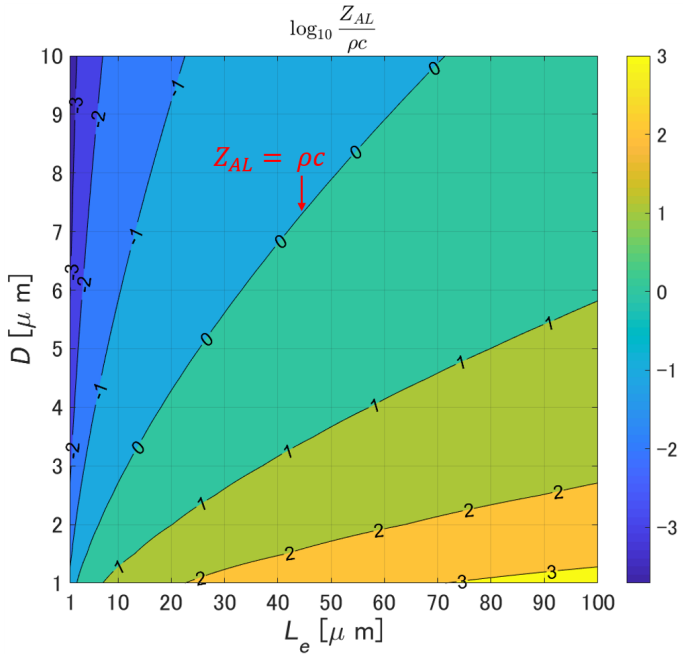

Figure 5.29: Numerically calculation result about the ratio of ρc and Z_{AL} when $\mu = 1.8\times10^{-5}$ Pa·s.

Then, the author describes Z_t. Z_t is expressed as follows[51].

$$Z_t = \frac{12\mu D_t}{h_w} \tag{5.22}$$

where D_t [m] is the backplate thickness and h_w[m] is the perforation size. Fig. 5.30 shows the numerically calculation result about the ratio of Z_t and ρc based on Eq. (5.22). The value of the contour on the graph $log_{10}\,(Z_t/\rho c) = 0$ means that Z_t is equal to ρc. This value have same means as in the case of Z_{AL}, that is, the smaller ratio value is desirable in order to achieve high efficiency.

The author considered the electrode dimensions from the aspect of energy efficiency. Increasing the ratio of perforations on the backplate contributes to generating ultrasound with high efficiency, while the ESF decreases. The diaphragm displacement in the direction of the backplate electrode is determined by the ESF magnitude and the restoring force of the the diaphragm. Therefore, the author considered the diaphragm length L_m which can cause the desired average displacement by the ESF generated with the above electrode dimensions.

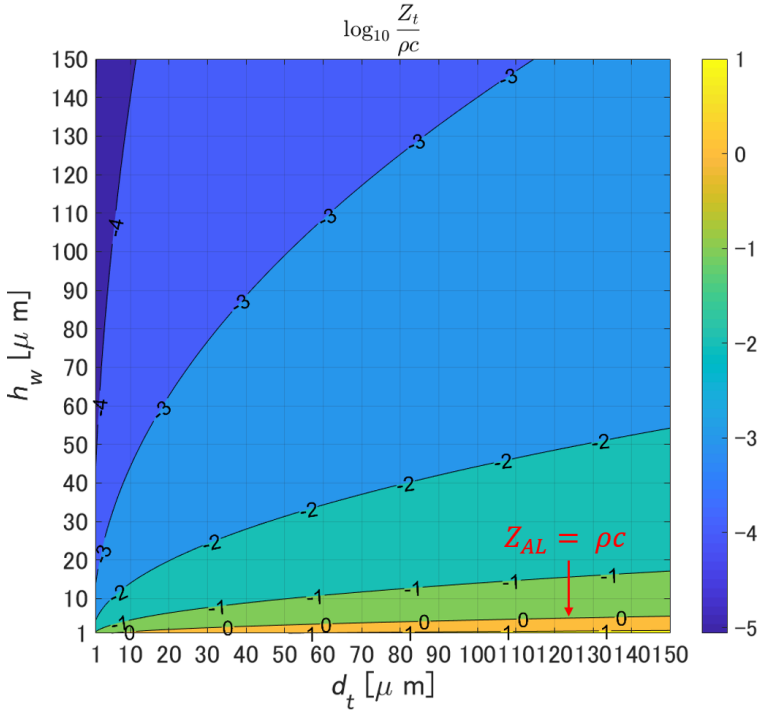

Figure 5.30: Numerically calculation result about the ratio of ρc and Z_t when $\mu = 1.8\times10^{-5}$ Pa·s.

when voltage V_1 [V] is applied to the structure of Fig. 5.27, the ESF F_e [N/m] generated between the diaphragm and the perforated electrode is expressed as follows.

$$F_e = \frac{1}{2}\varepsilon\left(\frac{V}{D}\right)^2 \frac{2L_e}{2L_e + h_w} L_m \tag{5.23}$$

Assuming F_e acts in the center of the diaphragm, the average displacement of the diaphragm $\bar{\xi}$ [m] is expressed as

$$\bar{\xi} = \frac{F_e L_m^3}{32Eh^3} \tag{5.24}$$

where E [Pa] is Young's modulus of the diaphragm, h [m] is the diaphragm thickness. From Eq. (5.23) and Eq. (5.24), L_m is obtained as

$$L_m = \sqrt[4]{\frac{2E\bar{\xi}h^3}{\frac{1}{2}\varepsilon\left(\frac{V}{D}\right)^2 \frac{2L_e}{2L_e+h_w}}} \tag{5.25}$$

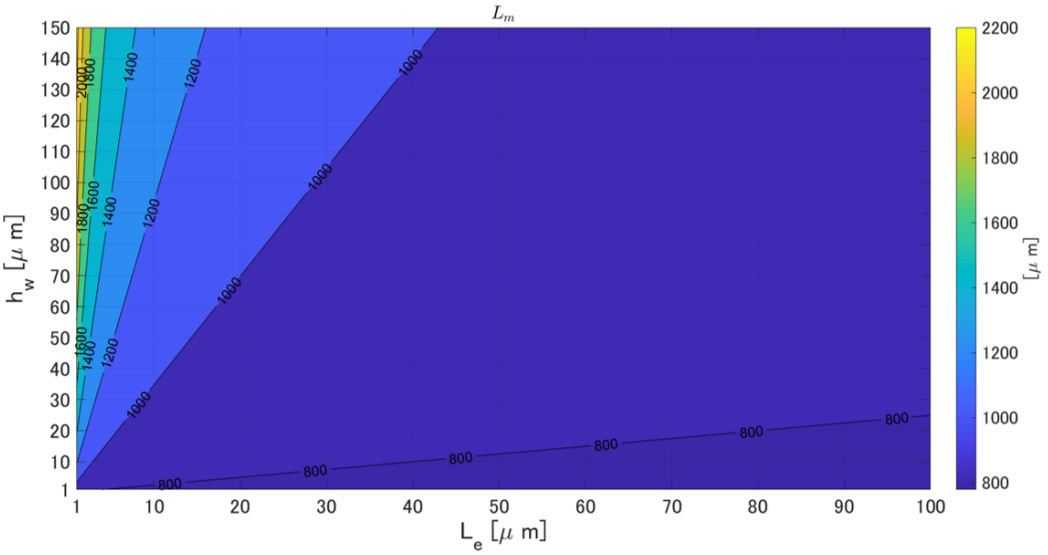

Figure 5.31: Numerically calculation result about the diaphragm length against the backplate electrode dimension.

Fig. 5.2.2 shows the numerically calculation result about the diaphragm length L_m assuming that $V_1 = 100\,\mathrm{V}$, $E = 4\,\mathrm{GPa}$, $h = 4\,\mu\mathrm{m}$, $D = 10\,\mu\mathrm{m}$, $\bar{\xi} = 5\,\mu\mathrm{m}$. From this figure, L_m needs about 1000 μm when $L_e = 25\,\mu\mathrm{m}$, $h_w = 80$ μm to obtain $\bar{\xi} = 5\mu\mathrm{m}$. Eq. 5.25 shows that L_m is proportional to the 1/4 power of ESF. Thus, L_m can be shorter than $1000\,\mu\mathrm{m}$ when higher voltage is applied to the structure with the same dimension above. For example, when applying $300\,\mathrm{V}$, L_m is about $600\,\mu\mathrm{m}$.

Next, the author considers the force required to lift the air when after the diaphragm deformed in the direction of the backplate electrode and the ESF disappeared. In the case of applying the tension to the diaphragm, the tension magnitude contributes to the displacement of the diaphragm and the frequency response. Note that the flexural rigidity of the diaphragm is ignorable compared to the tension.

Fig. 5.32 shows the model assuming that the center of the diaphragm deformed by ξ_{max} [m]. The diaphragm size is L_m[m] $\times$ W[m]. Here consider the case of generating p_0 [Pa] by lifting the diaphragm in this state with the tension T [N]. The force required for the diaphragm to lift the air F_{air} [N] is expressed as

$$F_{air} = W L_m p_0 \tag{5.26}$$

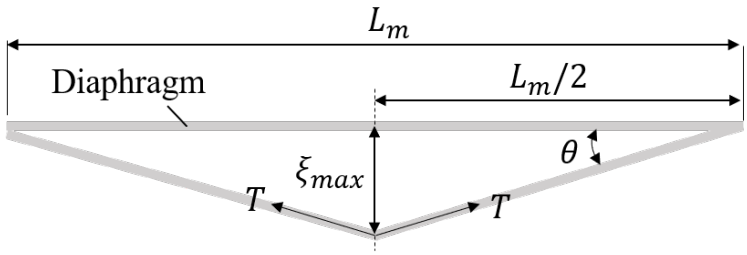

Figure 5.32: Mechanical model of the diagram with tension when the center of the diaphragm is displaced by ξ_{max}.

The vertical force of the tension T_v [N] is expressed as follows when assuming $\xi_{max} \ll L_m$.

$$T_v = 2T \sin\theta \approx 2T \tan\theta = \frac{4T\xi_{max}}{L_m} \tag{5.27}$$

When the tension lifts the air and generates p_0, $F_{air} = T_v$. From Eq. (5.26) and Eq. (5.27), the tension per unit length is expressed as

$$\frac{T}{W} = \frac{p_0 L_m^2}{4\xi_{max}} \tag{5.28}$$

The tension value obtained from Eq. (5.28) is the minimum required force to generate p_0. For example, in the case of $L_m = 900\,\mu$m, $\xi_{max} = 10\,\mu$m, $p_0 = 1\,$kPa, $T/w = 25\,$N/m is needed at least. In addition, the diaphragm movement after discharging the electric charge depends only on the tension. This means that the tension amplitude contributes to the diaphragm displacement.

5.2.3 Mechanical design

The author describes a mechanical design for the actual fabrication. The proposed structure for fabrication consists of four layers as shown in Fig. 5.33. The top layer is the diaphragm, which is the aluminum-evaporated PPS film (Torelina, TORAY INDUSTRIES, INC.) whose thickness $h = 4\,\mu$m and Young's modulus is $E = 4\,$GPa. The other layers is fabricated by etching SUS304 (Young's modulus $E = 193\,$GPa). Part$A$ is a frame that supports the diaphragm and determines the initial gap D between the diaphragm and the backplate electrode. In the paper, D is $10\,\mu$m. Part$B$ is the backplate electrode with perforations.

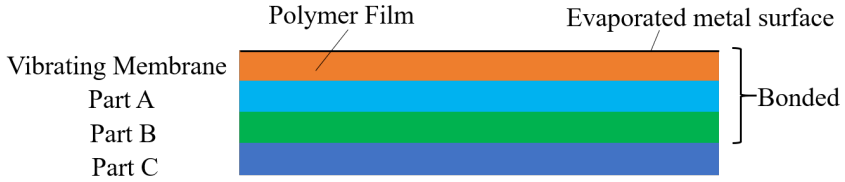

Figure 5.33: Structure for actual fabrication. The perforations in the Part$B$ are omitted.

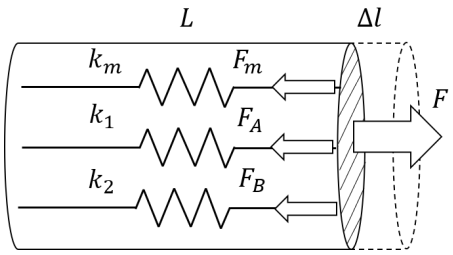

Figure 5.34: Physics model equivalent to the case where an external force F is applied to the structure where the diaphragm, Part$A$, and Part$B$ are bonded.

Part$C$ is a frame that supports the other parts and its size is same as the Part$A$. In this paper, the thickness of the Part$C$ is 300 μm. The diaphragm, Part$A$, Part$B$ are bonded. The element structure is realized by placing the bonded structure on Part$C$. The tension applied to the diaphragm is achieved by pulling the bonded structure.

Each part of the dimensions was designed to satisfy following three conditions. The first is applying the uniform tension to the the diaphragm. The second is reducing the energy loss in the structure as the author described above. The third is the diaphragm length to be able to pull in the direction of the bacplate electrode as the author described above.

Here, the author describes the first condition. Fig. 5.34 shows the model equivalent to the case when an external force is applied to the bonded structure consisted of the diaphragm, Part$A$, Part$B$. Where k_m, k_A, and k_B [N/m] are spring constant of the diaphragm, Part$A$, and Part$B$ respectively, F [N] is the external force applied to the bonded structure, Δl [m] is strain length of the structure, T, F_A, and F_B [N] is the restoring force at each part. At this time, the following relational expression holds.

$$F = T + F_A + F_B = (k_m + k_A + k_B)\Delta l \tag{5.29}$$

Assuming that k_A=αk_m, k_B=βk_m, Eq. (5.29) is expressed as

$$F = (1 + \alpha + \beta)\, k_m \Delta l \tag{5.30}$$

The ration of tension applied to the diaphragm T and the external force F is expressed as

$$\frac{F}{T} = \frac{(1 + \alpha + \beta)\, k_m \Delta l}{k_m \Delta l} = 1 + \alpha + \beta \tag{5.31}$$

Thus, in order to apply T to the diaphragm, the external force F needs to be $(1 + \alpha + \beta)$ times its force. The most desirable case is that the external force F directly becomes the tension T to the diaphragm, that is, $\alpha, \beta \ll 1$. Since the Young's modulus of SUS304 is about 50 times that of PPS film, the above specification is considered to be difficult. Thus, the author aimed to design the spring constant of Part$A$, Part$B$ for the same order as that of the diaphragm. In addition, Part$B$ needs bending rigidity in order not to move when the ESF is applied to it.

The author decided the dimension of each part to satisfy by simulations. Fig. **, Fig.**, and Fig. **, show the decided dimensions of each part respectively. The author used ANSYS 19.1 (ANSYS, Inc.) for the simulation. First, the author describes the spring constant of Part$A$, Part$B$. Here, the author introduces "square-shaped spring constant" to compare the spring constant of each part. Assuming that the size of each structure is $l \times w$, the square-shaped spring constant $k_A|_{square}$ and $k_B|_{square}$ [N/m] of each part can be obtained as follows.

$$k_A|_{square}, k_B|_{square} = \frac{F}{2\Delta\bar{l}} \frac{l}{w} \tag{5.32}$$

where $\Delta\bar{l}$ is the average strain in the tensile direction. The Square-shaped spring constant of the diaphragm $k_m|_{square}$ [N/m] is expressed as

$$k_m|_{square} = hE \tag{5.33}$$

Since the $h = 4\,\mu$m and the Young's modulus $E = 4\,$GPa, $k_m|_{square}$ is 1.6 $\times 10^4$ N/m.

Fig. 5.38 and 5.39 show the shape and size of Part$A$ and Part$B$ used for the simulation respectively. The simulations for both parts were performed by fixing one endpoint and applying 1N on the side surface. Fig. 5.40 and Fig. 5.41 show the result of Part$A$ and Part$B$ respectively. At this time, the average strain $\Delta\bar{l}$ in the tensile direction of each part was 3.1551 $\times 10^{-5}$ m and 4.7378 $\times 10^{-5}$ m. From Eq. (5.32), $k_A = 0.83 \times 10^4$ N/m , $k_B = 1.212 \times 10^4$ N/m are obtained. Thus, external force $F = 4.47 \times T$ [N] is needed in order to apply T [N] to the diaphragm.

Fig. 5.42 shows the simulation result about the flexural rigidity of Part$B$. The conditions were that the two side surfaces was fixed and the lower surface was applied 1471 Pa. The value of 1471 Pa is the pressure actually applied to the diaphragm when applied voltage is 300 V and the initial distance between the diaphragm and the backplate electrode is 10 μm. The average displacement was 5.6972 $\times 10^{-8}$ at the result. These values can be neglected compared to $D = 10$ μm. From the above results, the author judged that the shape and the size of Fig. 5.35, and Fig. 5.35 are useful.

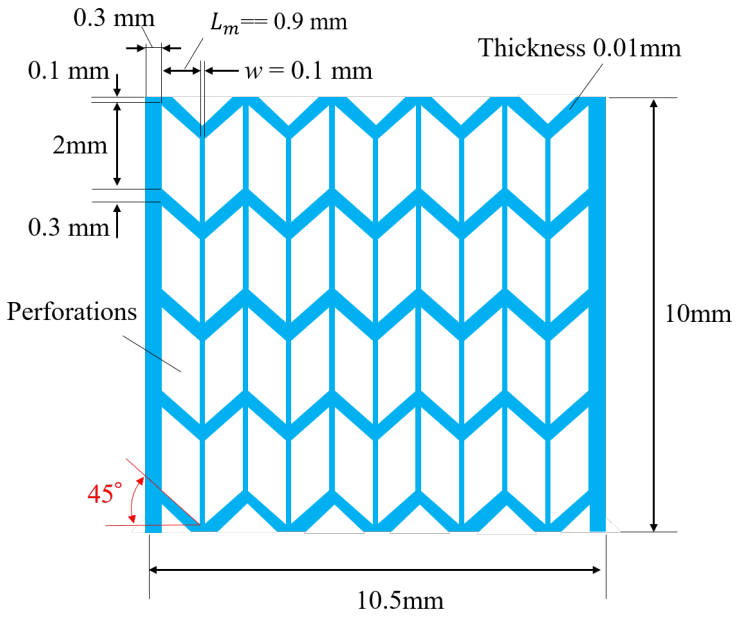

Figure 5.35: Dimension and shape of Part$A$.

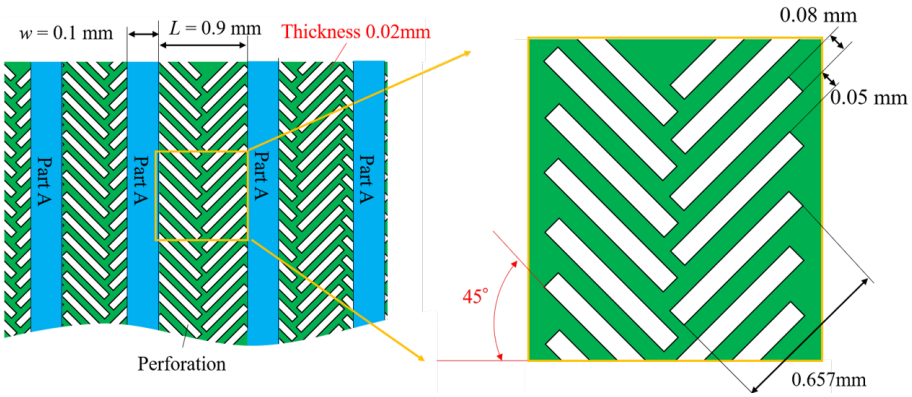

Figure 5.36: Dimension and shape of Part$B$.

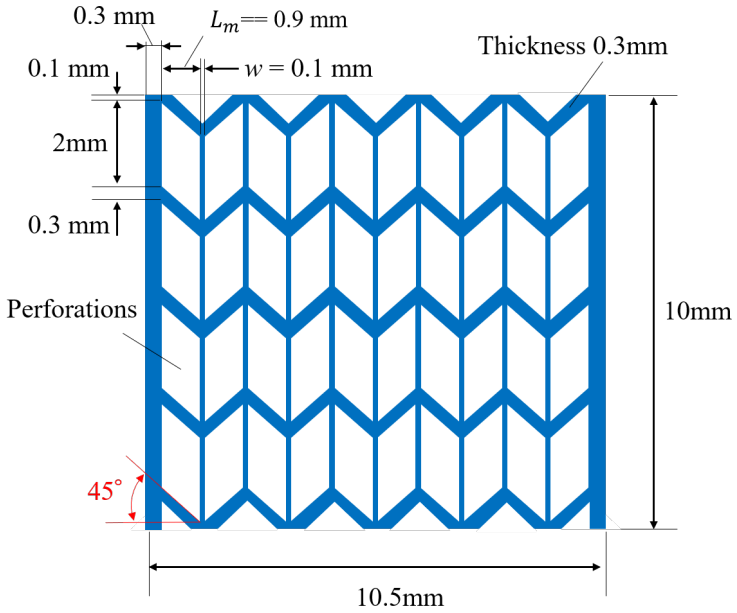

Figure 5.37: Dimension and shape of Part$C$.

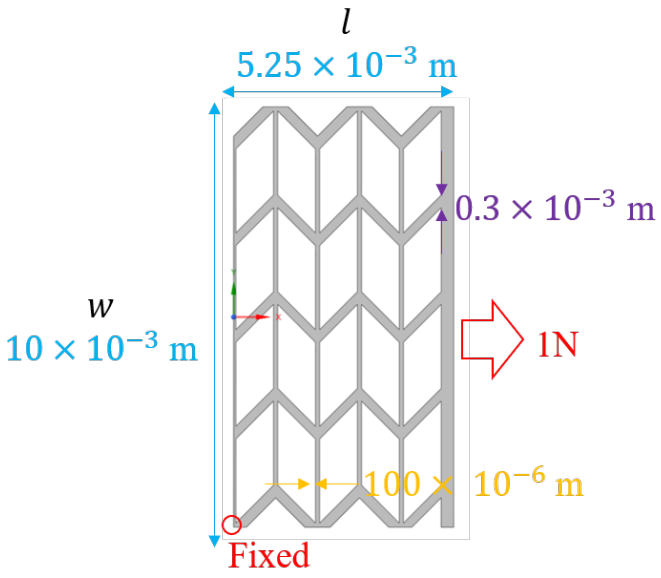

Figure 5.38: Shape and size of Part$A$ for a simulation.

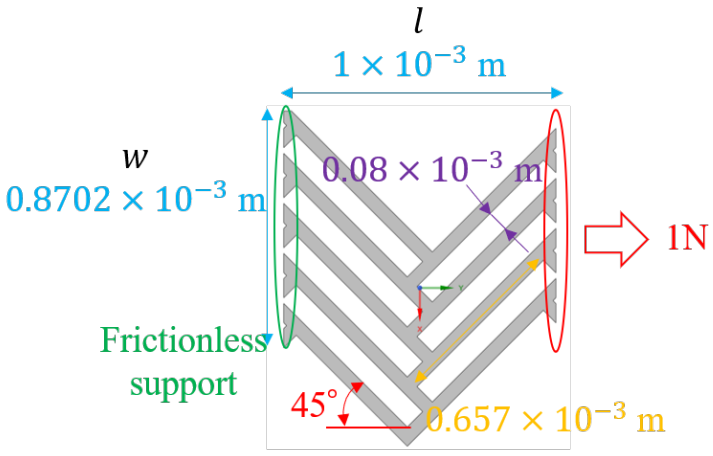

Figure 5.39: Shape and size of Part$B$ for a simulation.

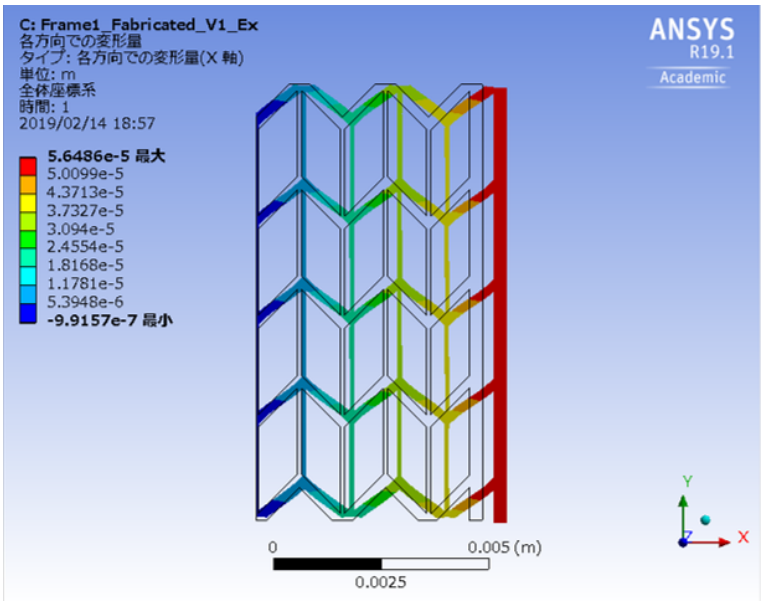

Figure 5.40: Simulation result of the strain under the conditions in Fig. (5.38). The average strain $\Delta\bar{l}$ in the tensile direction was 3.1151 $\times 10^{-5}$ m.

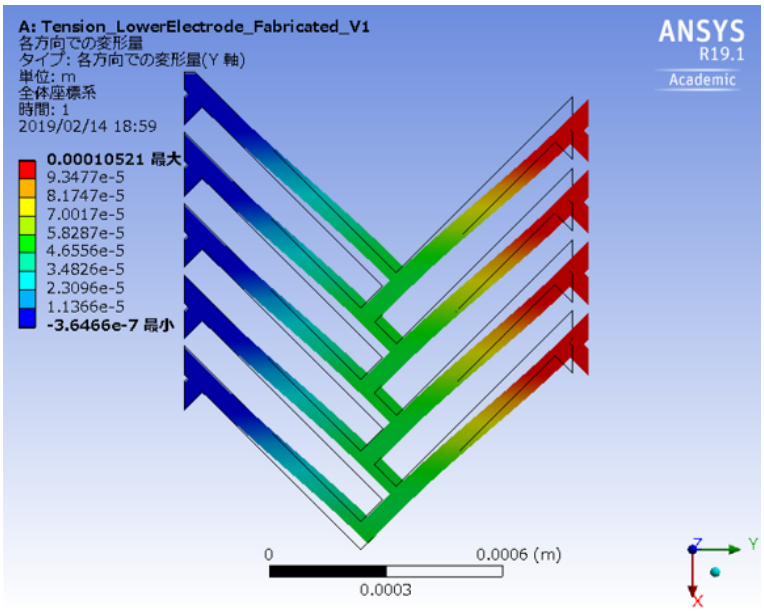

Figure 5.41: Simulation result of the strain under the conditions in Fig. (5.39). The average strain $\Delta\bar{l}$ in the tensile direction was 4.7378 $\times 10^{-5}$ m.

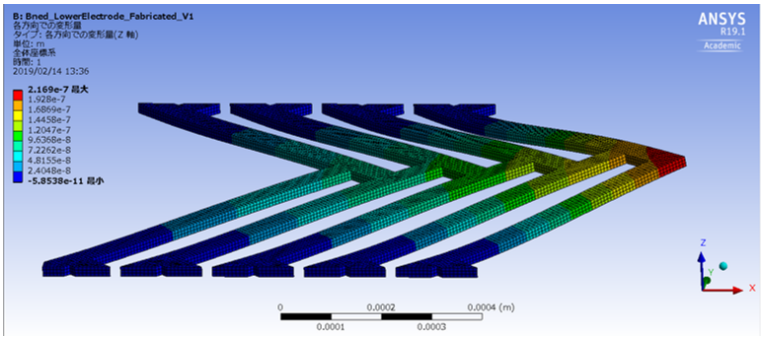

Figure 5.42: Simulation result of the flexural rigidity in Fig. (5.39).

5.2.4 Experimental results

This subsection will describe experiments divided into two types roughly. The one is the experiment using the fabricated structure by laminating a diaphragm on the stainless-steel structure composed of part$A$, B and C via an adhesive. The other is an experiment using the fabricated structured by directly laminating the diaphragm on the stainless-steel structure without using adhesive. The same stainless-steel structure was used in both experiments.

Fig. 5.43 shows the photograph of the stainless structure and Fig. 5.44 shows the enlarged photograph taken with the microscope. This structure was made by crimping each structure which has perforations made by etching (SHIN-EI SANGYO CO., LTD). The perforation patterns in each part were identical with that described in the simulation. The thickness of Part$A$, B, and C were set to 10 μm, 20 μm, 300 μm respectively. The fabricated structure

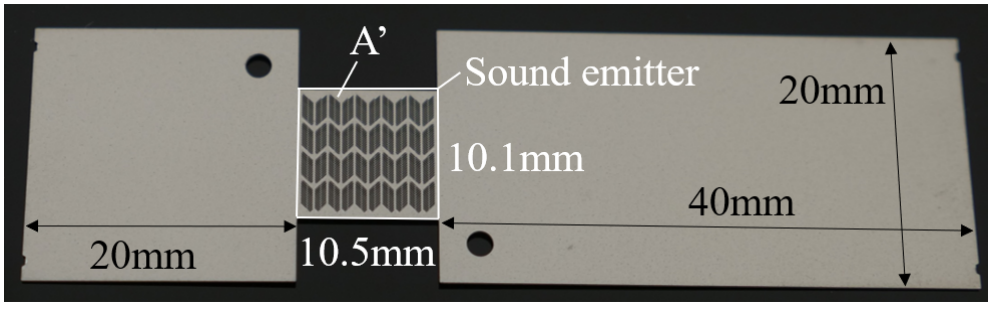

Figure 5.43: Photograph of stainless-steel structure composed of Part A, B, and C

was different in two points from that described in the simulation due to fabrication process problems. The first different point is the shape of Part$A$ and C where is A' in Fig. 5.43. In

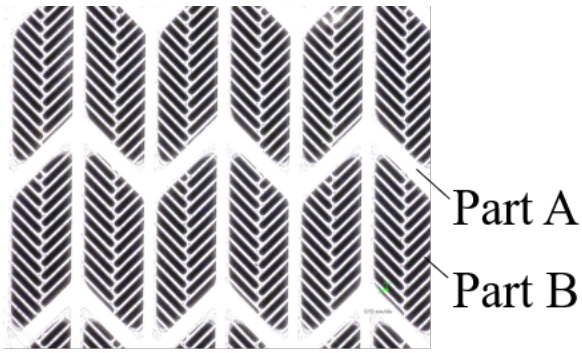

Figure 5.44: Enlarged photo of Fig. 5.43.

the simulation, the shape of Part$A$ and C was without the segment A' so that uniform tension was applied to the diaphragm when the integrated structure composed of the diaphragm and the stainless-steel structure was applied external force. The second point is that the stainless-steel structure was fabricated by adhering not only Part$A$ and B but also Part C.

5.2.4.1 The case of diaphragm fixed to the stainless structure with adhesive

Fig. 5.45 shows the prototype transducer and its cross-section. The diaphragm, 4 μm-thick PPS film coated with nickel, was laminated on the stainless-steel structure via an adhesive applied only in the longitudinal direction of stainless-steel Part$A$ in Fig. 5.43. The movable area of the diaphragm was set to 10.1 mm $\times$ 10.5 mm. The peripheral area where the diaphragm and stainless-steel structure are overlapped out of the vibration area was covered by a 1 mm-thick acrylic plate with a 10.1 mm $\times$ 10.5 mm aperture so that sound waves from unexpected areas do not affect the measurement. In addition, a 12.5 μm-thick insulating film (Kapton 50EN, DU PONT-TORAY INDUSTRIES, INC.) was inserted in the peripheral area to prevent unexpected discharge. For the base plate of the device, the author used an acrylic plate.

The author conducted experiments using the prototype transducer with the setup shown in Fig. 5.46. In the sound pressure measurement, the author used a standard microphone (4138-A015, Bruel & Kjaer) with an amplifier (NEXUS Conditioning Amplifier, Bruel & Kjaer) and obtained the numerical RMS value read visually on the oscilloscope. The micro-

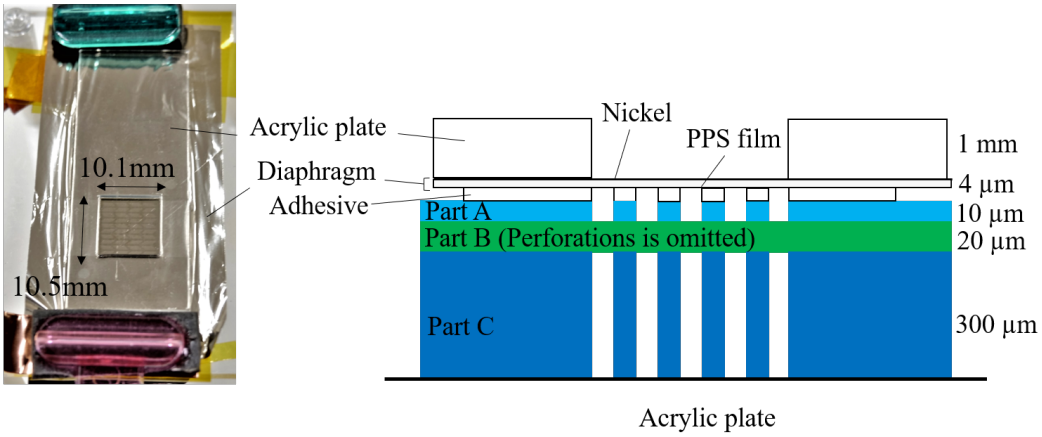

Figure 5.45: (left): Photograph of the prototype transducer. (right): Cross-section of the structure.

phone was set at 20 cm above the prototype transducer as shown in Fig. 5.46 to avoid the interference with reflected sound from the environments. The author confirmed the reflected sound is negligible by measuring the sound pressure fluctuations with the position shift of the microphone around the original position.

The driving method described in Section 4.3 was realized by using the circuit as shown in Fig. 5.46. The circuit switches the Pch/Nch MOSFET to apply the electric charge to 1/8 of the drive cycle T [s] and discharge the electric charge after $T/2$ so that aimed voltage was applied to the diaphragm in the initial state. In this experiment, the author aimed to apply 100 V to the diaphragm and set 100 V at DC power supply (PD110-5AD, TEXIO CORPORATION) in Fig. 5.46. The prototype device was driven from 20 kHz to 100 kHz.

Fig. 5.47 shows the RMS sound pressure observed at 20 cm above the prototype. This sound pressure is about one-hundredth of the desired sound pressure. The sound pressure can be improved by increasing the applied voltage because the generated sound pressure increases with the square of the applied voltage theoretically. However, from this experimental result, even if 300 V is applied, the desired sound pressure cannot be obtained with the prototype in this experiment. One possible factor for this cause is the thickness of adhesive between the diaphragm and stainless structure. The ESF applied to the diaphragm is determined by the applied voltage and the distance D between the diaphragm and the backplate electrode (Part$B$). It is desirable that the adhesive thickness is close to 0 μm to strengthen the ESF

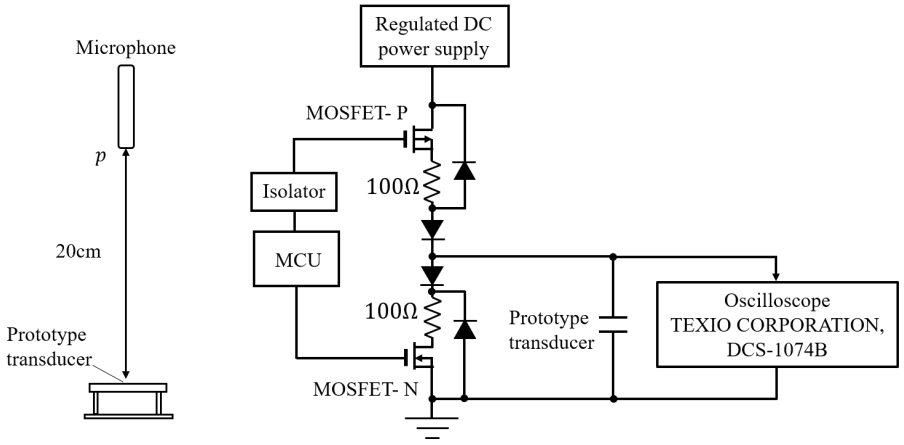

Figure 5.46: Experimental setup. (left): Microphone observes sound pressure at 20cm from the device surface. (right): Measurement system of voltage applied to the transducer.

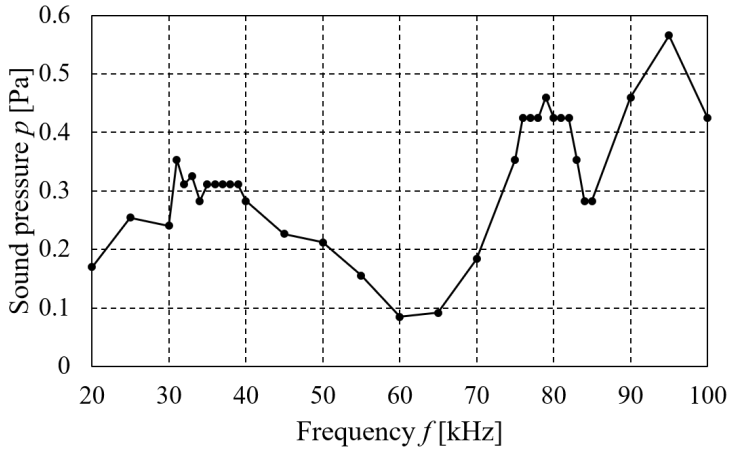

Figure 5.47: Frequency characteristic of the prototype transducer when applied voltage 100 V.

under the condition that the applied voltage is constant. In the prototype, D is more than $10\,\mu$m due to the adhesive thickness, although the actual thickness is unknown. Thus, it is considered that the ESF was smaller than the expected one, which leads the decrease of generated sound pressure. Therefore, the author fabricated a transducer which is the diaphragm laminated on a stainless steel structure without the adhesive and conducted experiments using the transducer. The experiment details will be described next subsection, and here the author considers the size of the diaphragm used in the following experiments because there is a possibility that the diaphragm pulls in when the diaphragm is placed on the stainless structure as the device in Fig. 5.45.

Fig. 5.48 shows the equivalent model of the above prototype transducer. C_t[F] is the capacitance of the sound emitter part and C_p[F] = NC_0 = const. is the capacitance of the part out of the sound emitter part. Assuming that the initial distance between the diaphragm and the backplate electrode is D [m] and its size is S [m^2], C_t is expressed as

$$C_t = \varepsilon \frac{S}{D} \tag{5.34}$$

Let consider the ESF applied to diaphragm when V [V] is applied to only t_1 [s] for a very short time and the electric charge Q_0 [C] is accumulated in those capacitors. Then Q_0 is expressed as

$$Q_0 = (C_t + C_p)V = const. \tag{5.35}$$

The ESF generated by accumulated charge causes the diaphragm to approach the backplate electrode from d [m] to $d - \Delta d$ [m]. Assuming that the capacitance of the sound emitter part changes from C_t to C_t'[F] and the voltage across the capacitors has changed from V to V' [V], the following equation is lead.

$$Q_0 = (C_t' + C_p')V' = const. \tag{5.36}$$

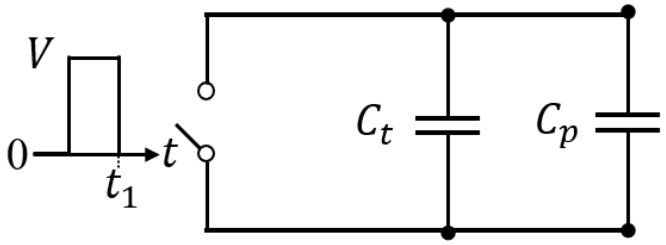

Figure 5.48: Circuit model for the electric charge accumulated in the device in Fig. 5.45.

From Eq. (5.35) and Eq.(5.36),

$$(C_t + C_p)V = (C_t' + C_p')V' = const. \Leftrightarrow \frac{V'}{V} = \frac{C_t + C_p}{C_t' + C_p} \tag{5.37}$$

Here, substitute $C_t' = \varepsilon S/(d - \Delta d)$ for 5.37,

$$\frac{C_t'}{C_t} = \frac{d}{d^{\Delta}d} \Leftrightarrow C_t' = \frac{D}{D - \Delta D} C_t \tag{5.38}$$

From Eq. (5.37) and Eq.(5.38),

$$\frac{V'}{V} = \frac{1 + N}{\frac{D}{D-\Delta D} + N} \Leftrightarrow V' = \frac{(1 + N)(d - \Delta D)}{(1 + N)D - N\Delta D} V \tag{5.39}$$

Let F be the ESF generated by accumulating electric charges only in the sound emitting part, which is constant regardless of distance between the diaphragm and the backplate electrode. Let F' be the ESF generated in the diaphragm when the diaphragm moves Δd while the electric charge is supplied with from C_p. The relationship between F and F' is as follows.

$$\frac{F'}{F} = \left(\frac{(1 + N)D}{(1 + N)D - N\Delta D} \right)^2 \tag{5.40}$$

For example, when D=10 μm, $\Delta D = 5\,\mu$m, $N = 13$ (the size of sound emitter part is 100 m^2, the size out of the sound emitter part is 1200 m^2 in the above prototype), F' is $3.48F$. Thus, the pull-in phenomenon can occur when the part out of sound emitter part exists.

5.2.4.2 The case of diaphragm not fixed to the stainless structure with adhesive

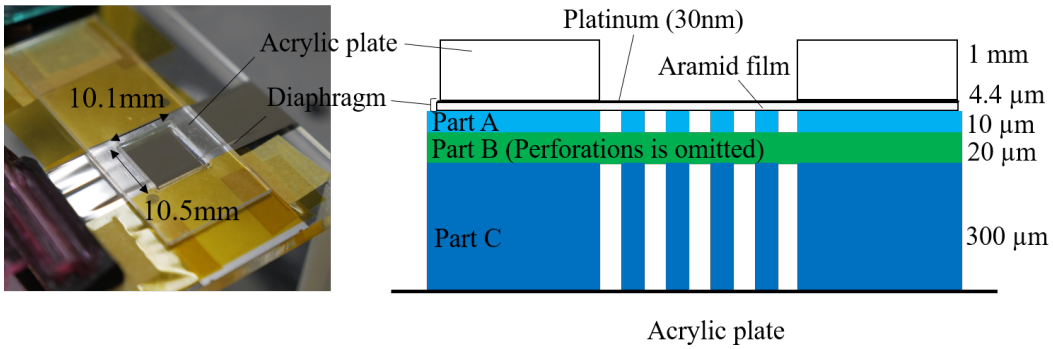

Figure 5.49: (left): Photograph of the prototype transducer without adhesive. (right): Cross-section of the structure.

Fig. 5.49 shows the prototype transducer and its cross-section. The author used a 4.4 μm-thick aramid film (Mictron, TORAY INDUSTRIES, INC.) deposited with 30 nm-thick platinum for the diaphragm. The size of the diaphragm was placed to be the same size as the size of the movable part, 10.1 mm $\times$ 10.5 mm, as shown in the Fig. 5.49 aiming at constant charge accumulated in the diaphragm. After placing the diaphragm, the author inserted an 12.5 μm-thick insulating film (Kapton 50EN, DU PONT-TORAY INDUSTRIES, INC.) between the diaphragm and the stainless steel structure in order not to prevent discharge. In addition, the author put a 1 mm-thick acrylic plate with a 10.1 mm $\times$ 10.5 mm aperture on the prototype transducer so that sound waves from unexpected areas do not affect the measurement as previously mentioned.

The experimental setup and the driving method were same as Fig. 5.47 except for the regulated DC power supply. In this experiment, the author used the regulated DC power supply (PWR801H, KIKUSUI ELECTRONICS CORP.). Here, the author describes two kinds of experiments conducted under two conditions of the diaphragm with/without the tension. The author fabricated the transducer twice for each condition. Note that the tension applied to the diaphragm is not quantified due to hand sticking.

First, the author investigated the influence of the tension to frequency characteristics. The experiments were conducted twice under both conditions. The author aimed to apply 100 V to the diaphragm and set 100 V at DC power supply. Fig. 5.50 shows the RMS sound

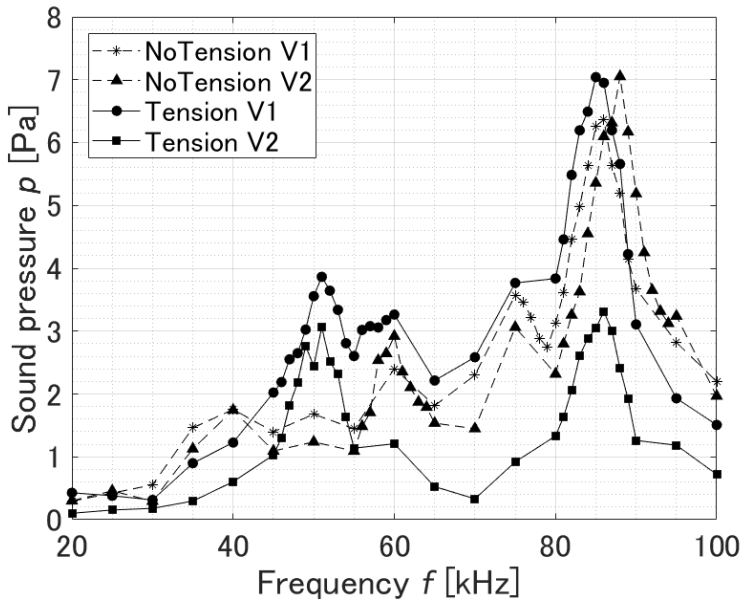

Figure 5.50: Frequency characteristic of the prototype transducer of Fig. 5.49 when applied voltage is shown in Fig. 5.51.

pressure observed at 20 cm above the prototype driven from 20 kHz to 100 kHz. This sound pressure values were obtained by Fourier transformation. Fig. 5.51 shows the measured RMS voltage applied to the prototype. Fig. 5.50 shows that the prototype transducer has two peaks. One is 51 kHz and it is considered that the tension contributes to this frequency. Another peak is around 86 kHz regardless of presence or absence of the applied tension.

Here, consider the resonance frequency by using a simple model consisted of only the stiffness of the air layer with thickness D formed by Part$C$ and the mass of the diaphragm as shown in Fig. 5.52. Z_m and Z_{ALC} in Fig. 5.52 are the acoustic impedance of the diaphragm and the acoustic impedance of the air layer respectively and are expressed as follows.

$$\begin{aligned} Z_m &= j\omega\rho_m h \\ Z_{ALC} &= -j\rho_{air} c cot(\kappa D) \end{aligned} \tag{5.41}$$

Where h is the diaphragm thickness, ρ_m is diaphragm density, ρ_{air} is air density, and κ is wavenumber. The frequency when these reactance components are equal is the resonance

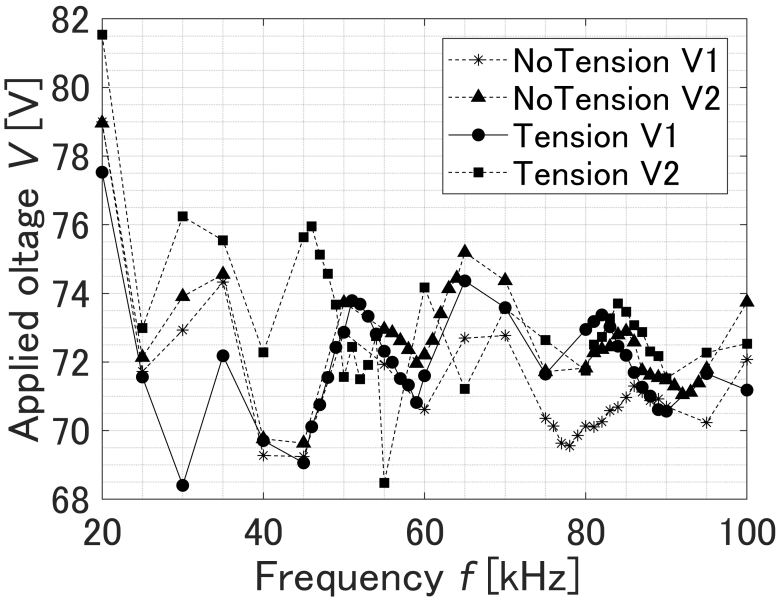

Figure 5.51: Applied voltage (RMS value) to drive prototype transducer of Fig. 5.49.

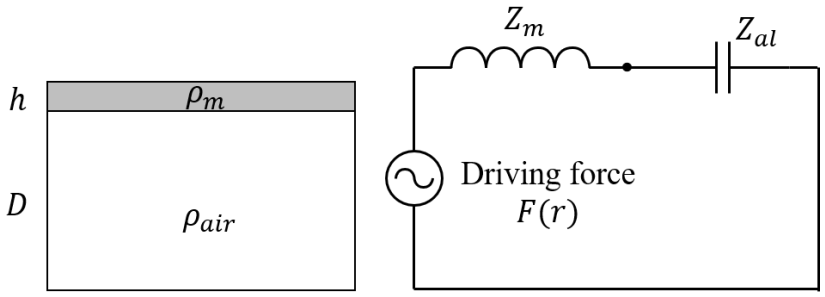

Figure 5.52: Physics model to determine the resonant frequency. (left): Mechanical model. (right): Equivalent circuit of the mechanical model.

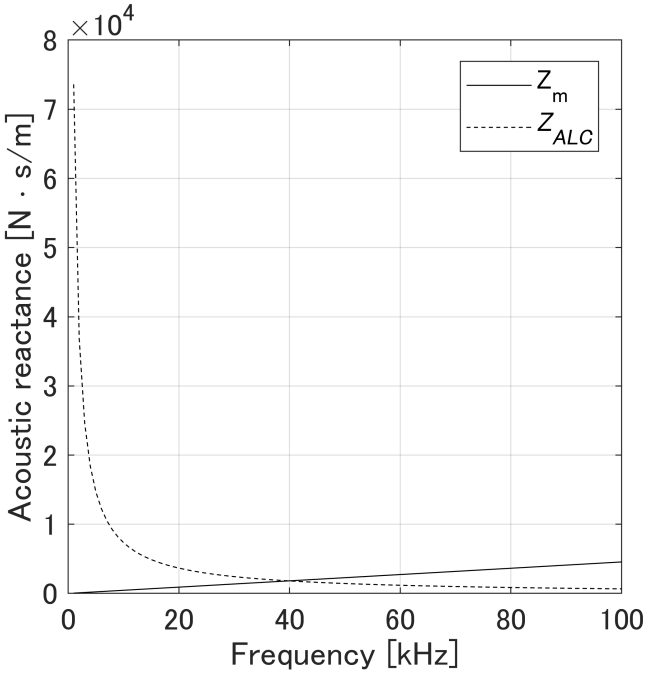

Figure 5.53: Numerically calculation result of resonant frequency obtained from Eq. (5.41).

frequency. Fig. 5.53 shows the numerically calculation result of each reactance components in the condition of the above prototype. This result shows that the resonant frequency is around 40 kHz. Therefore, the reason for resonant frequency around 86 kHz is not clear. It is necessary to reveal the motion mechanism of the strucuture analytically and experimentally.

From Fig. 5.50, the desired sound pressure was likely to be obtained using the transducer in this experiment as the applied voltage increases. Thus, the author investigated the relationship between the applied voltage and the generated sound pressure. In this experiment, the author used the second device (V2 in Fig. 5.50) above the experiment under both tension conditions. The drive frequency were two peaks in each device in the above experiment, that is, the frequency was 60 kHz and 88 kHz in the case of absence of the tension, and 51 kHz and 86 kHz in the case of presence of the tension. The experimental setup and driving method were the same as the above experiment and the maximum applied voltage was 300 V.

Fig. 5.54 shows the RMS sound pressure observed at 20 cm above the each prototype. The sound pressure value in Fig. 5.54 were obtained by Fourier transformation and the applied voltage value is RMS value. Fig. 5.55 shows the RMS sound pressure at the each prototype

surface calculated using Eq. 5.3. Note that the author adopted the value of a in Eq.5.3 is the value when the circular area of radius a is equal to the area of 10.1 mm × 10.5 mm[52]. Fig. 5.56 is the average displacement of the diaphragm at each frequency calculated from Eq. (3.3) assuming that the diaphragm vibrates uniformly.

Fig. 5.54 shows that maximum RMS sound pressure at 20 cm above the transducer (diaphragm with applied tension) was 31.2 Pa at 51 kHz when the applied voltage is maximum. At this time, the acoustic power per square centimeter of the transducer is calculated as 37.7 mW. This value meets the target specification of 24 mW/cm^2.

The generated sound pressure at 51 kHz increased with about the square of the applied voltage as with the principle while the sound pressure at the other frequency did not increase as same as at 51 kHz. In addition, Fig. 5.56 shows that the average displacement of the diaphragm tends to become smaller as the driving frequency becomes higher. The reasons for these phenomena is not clear and must be revealed analytically and experimentally. If the reasons become clear, it will be able to fabricate high-frequency devices with higher output than the existing one, for example, 80 kHz devices.

5.2.5 Conclusion

In this subsection section, the author described the structure substituting for that composed of mesh electrode described in Section 5.1.

The author determined the perforaion size in backplate electrode by theoretical consideration and simulation. The experiment using fabricated transducer shows that the proposed transducer met the required specifications, however, the mechanism for emitting sound is not obvious. In addition, the electro-acoustic energy conversion efficiency is also not obvious. Future works are to reveal these factors analytically and experimentally and fabricate AUPA based on the proposed structure.

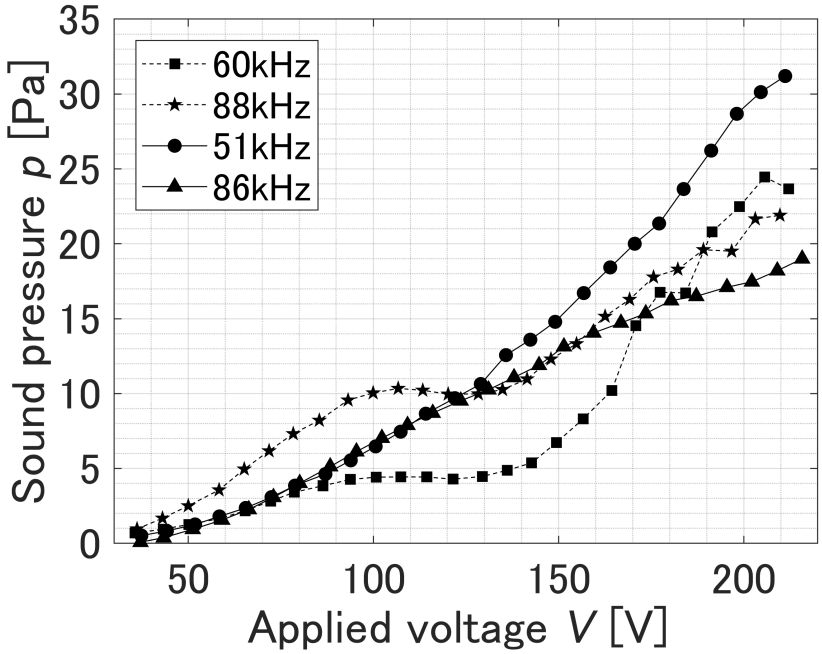

Figure 5.54: Applied voltage RMS-amplitude V contribution to sound pressure. Sound pressure was obtained at 20 cm.

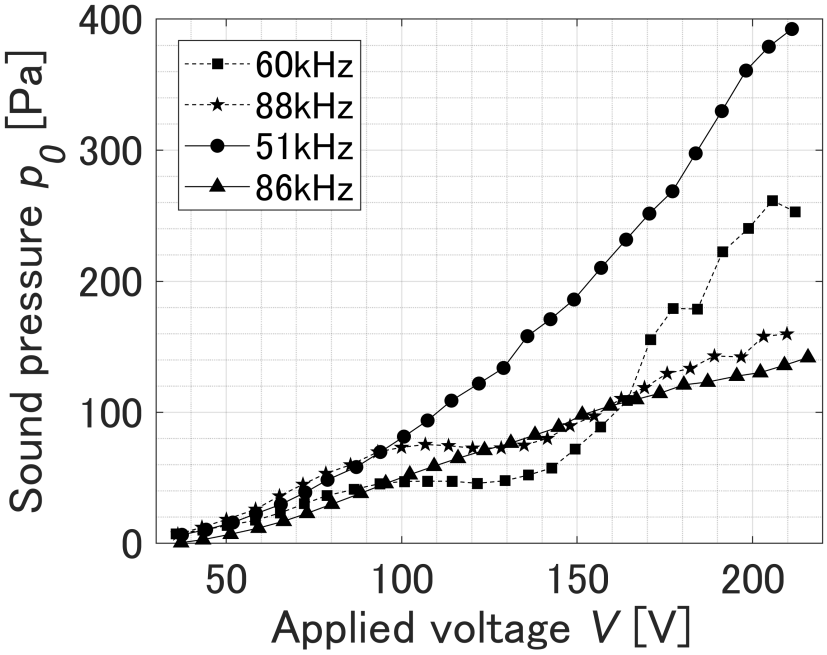

Figure 5.55: Applied voltage RMS-amplitude V contribution to the sound pressure on the diaphragm surface.

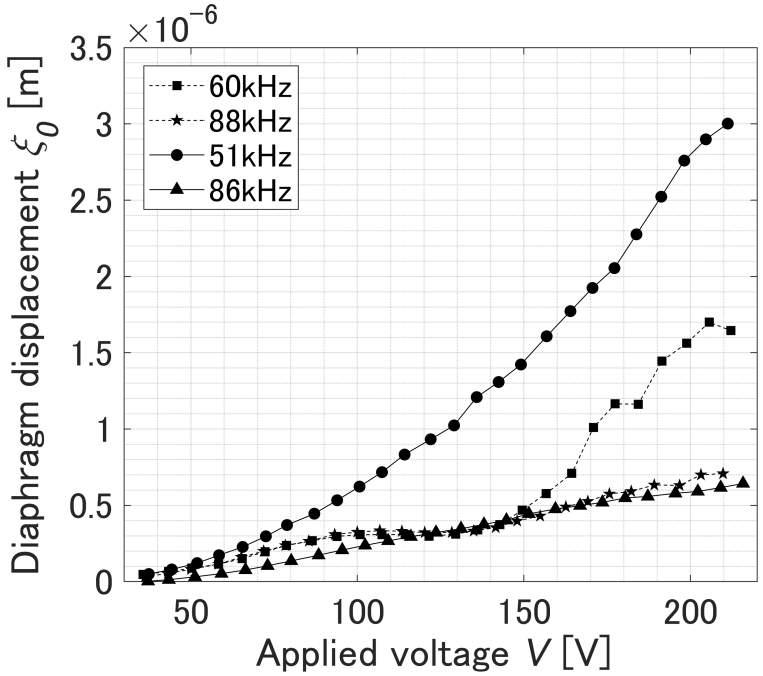

Figure 5.56: Applied voltage RMS-amplitude V contribution to the average displacement of the diaphragm.

Chapter 6

Conclusion

The goal of this research is to realize sheet shaped ultrasound phased array (AUPA) for nonlinear acoustic application, especially for the tactile presentation. This thesis mainly described acoustic transducers based on capacitive type to achieve the goal and showed the feasibility to achieve the goal.

In chapter 1, the author described the current status of nonlinear acoustic applications, the inevitability of sheet shaped AUPAs, and what kinds of new application developments are expected by the sheet shaped AUPAs. Then, the author referred to the existing airborne ultrasound transducer and revealed that the AUPAs for the above applications have not been realized.

In chapter 2, the author described the principle of tactile presentation using the AUPAs and clarified specifications required for development AUPAs.

In chapter 3, the author described the problems in intensity enhancement of sound pressure with the capacitive type.

In chapter 4, the author outline to solve the problems described in Chapter 3.

In chapter 5, the author proposed two kinds of acoustic transducers based on the solutions and evaluated fabricated the transducers in experiments.

One is the transducer using the metal mesh electrode. This type showed the effectiveness in

a single element although the mechanism of generating sound is not clarified. In addition, the author proposed and fabricated a compact and highly efficient drive circuit that can be placed on the back of each element, and showed the effectiveness of the circuit. After that, the author fabricated the phased array device using the above structure with the metal mesh electrode and the circuit. The experiment with the prototype device revealed that the reproducibility of the mechanical structure in each element was a problem.

The other is the transducer using the perforated backplate electrode. The shape of the electrode was decided based on theoretical and analytical consideration. The experiment using this transducer showed the effectiveness than that using the metal mesh electrode although the mechanism of generating sound is not clarified. The mechanism of this transducer must be revealed for two reasons. One reason is to prevent variations in the mechanical structure of each element when arrayed. The other reason is that there is a possibility to fabricate high-frequency AUPAs with higher output than the existing one, for example, 80 kHz.

List of publications

Journal Articles

1. 神垣貴晶, 二宮悠基, 篠田裕之, “高効率・高出力な静電駆動型空中超音波振動子の開発,”計測自動制御学会論文集, Vol. 54, No. 3, pp. 340-345, 2018.

International Conference

1. Takaaki Kamigaki, Yuki Ninomiya, and Hiroyuki Shinoda, “Electrostatically Driven Airborne Ultrasound Transmitter with Fine Mesh Electrode,” *in Proc. 2018 International Flexible Electronics Technology Conference (IFETC)*, pp. 1-3, Aug. 7-9, 2018, Ottawa, Canada.

2. Takaaki Kamigaki, Akihito Noda, and Hiroyuki Shinoda, “Thin and Flexible Airborne Ultrasound Phased Array for Tactile Display,” *in Proc. SICE Annual Conference 2017*, pp. 736-739, Sep., 2017, Kanazawa, Japan.

3. Kentaro Yoshida, Takaaki Kamigaki, Seki Inoue, Keisuke Hasegawa, Yasutoshi Makino, and Hiroyuki Shinoda, “HaptoCloneAR (Haptic-Optical Clone with Augmented Reality) for Mutual Interactions with Midair 3D Floating Image and Superimposed 2D Display,” *Asia Haptics 2016*, Kashiwanoha, Nov. 29-Dec. 1, 2016

Domestic Conference

1. 水谷沙耶, 神垣貴晶, 鈴木颯, 高橋諒子, 松林篤, 藤原正浩, 牧野泰才, 篠田裕之, “非接触触覚刺激の時空間変調パターンによる知覚強度の比較,”第 23 回バーチャルリアリティ学会大会, 33A-4, 東北大学青葉山新キャンパス, 仙台, Sep. 19-21, 2018.

2. 神垣貴晶, 二宮悠基, 篠田裕之,“静電駆動による薄型空中超音波フェーズドアレイ,”第 35 回センシングフォーラム資料, pp. 17-20, Aug., 2018, 山口大学, 山口.

3. 神垣貴晶, 篠田裕之, “薄型空中超音波フェーズドアレイのための高効率な小型駆動回路の開発,”第 18 回計測自動制御学会システムインテグレーション部門講演会論文集, pp. 303-306, Dec., 2017., 仙台.

4. 神垣貴晶, 二宮悠基, 篠田裕之,“薄型空中超音波フェーズドアレイのための高出力・高効率な静電駆動型振動子,”第 34 回センシングフォーラム資料, pp. 142-146, Sep., 2017, 熊本大学, 熊本.

5. 二宮悠基, 神垣貴晶, 篠田裕之, “シート状空中超音波フェーズドアレイの共振周波数調整機構,”ロボティクス・メカトロニクス講演会 2017 講演論文集, 2P1-O01, May, 2017, 福島

6. 神垣貴晶, 野田聡人, 牧野泰才, 篠田裕之,“シート状空中超音波フェイズドアレイのための振動子の開発とその評価,”第 17 回計測自動制御学会システムインテグレーション部門講演会論文集, pp. 48-51, Dec., 2016, 札幌.

7. 神垣貴晶, 井上碩, 門内靖明, 野田聡人, 牧野泰才, 篠田裕之, “シート状空中超音波フェイズドアレイ,”第 33 回センシングフォーラム資料, pp. 240-243, Sep., 2016, 近畿大学・和歌山キャンパス, 和歌山.

Patents

1. 特願 2017-148364, 超音波発生デバイス, [発明者] 篠田裕之, 神垣貴晶, 二宮悠基, [出願人] 国立大学法人東京大学, 2017 年 7 月 31 日出願

2. 特願 2016-169625, 超音波発生デバイス, [発明者] 篠田裕之, 神垣貴晶, [出願人] 国立大学法人東京大学, 2016 年 8 月 31 日出願

Awards

1. 第 18 回計測自動制御学会システムインテグレーション部門講演会優秀講演賞

Refereces

[1] S. Inoue, Y. Makino, and H. Shinoda, "Scalable architecture for airborne ultrasound tactile display," in *International AsiaHaptics conference*. Springer, 2016, pp. 99–103.

[2] https://www.ultrahaptics.com/products-programs/touch-development-kit/.

[3] B. Bayram, E. Hæggstrom, G. G. Yaralioglu, and B. T. Khuri-Yakub, "A new regime for operating capacitive micromachined ultrasonic transducers," *ieee transactions on ultrasonics, ferroelectrics, and frequency control*, vol. 50, no. 9, pp. 1184–1190, 2003.

[4] S. Olcum, F. Y. Yamaner, A. Bozkurt, and A. Atalar, "Deep-collapse operation of capacitive micromachined ultrasonic transducers," *IEEE transactions on ultrasonics, ferroelectrics, and frequency control*, vol. 58, no. 11, pp. 2475–2483, 2011.

[5] P. J. Westervelt, "Parametric acoustic array," *The Journal of the Acoustical Society of America*, vol. 35, no. 4, pp. 535–537, 1963.

[6] W.-S. Gan, J. Yang, and T. Kamakura, "A review of parametric acoustic array in air," *Applied Acoustics*, vol. 73, no. 12, pp. 1211–1219, 2012.

[7] M. Yoneyama, J.-i. Fujimoto, Y. Kawamo, and S. Sasabe, "The audio spotlight: An application of nonlinear interaction of sound waves to a new type of loudspeaker design," *The Journal of the Acoustical Society of America*, vol. 73, no. 5, pp. 1532–1536, 1983.

[8] Y. Ochiai, T. Hoshi, and I. Suzuki, "Holographic whisper: Rendering audible sound spots in three-dimensional space by focusing ultrasonic waves," in *Proceedings of the 2017 CHI Conference on Human Factors in Computing Systems*. ACM, 2017, pp. 4314–4325.

[9] T. Iwamoto, M. Tatezono, and H. Shinoda, "Non-contact method for producing tactile sensation using airborne ultrasound," in *International Conference on Human Haptic Sensing and Touch Enabled Computer Applications*. Springer, 2008, pp. 504–513.

[10] T. Hoshi, M. Takahashi, T. Iwamoto, and H. Shinoda, "Noncontact tactile display based on radiation pressure of airborne ultrasound," *IEEE Transactions on Haptics*, vol. 3, no. 3, pp. 155–165, 2010.

[11] M. Fujiwara, K. Nakatsuma, M. Takahashi, and H. Shinoda, "Remote measurement of surface compliance distribution using ultrasound radiation pressure," in *World Haptics Conference (WHC), 2011 IEEE*. IEEE, 2011, pp. 43–47.

[12] K. Hasegawa, L. Qiu, A. Noda, S. Inoue, and H. Shinoda, "Electronically steerable ultrasound-driven long narrow air stream," *Applied Physics Letters*, vol. 111, no. 6, p. 064104, 2017.

[13] Y. Ochiai, T. Hoshi, and J. Rekimoto, "Pixie dust: graphics generated by levitated and animated objects in computational acoustic-potential field," *ACM Transactions on Graphics (TOG)*, vol. 33, no. 4, p. 85, 2014.

[14] A. Marzo, S. A. Seah, B. W. Drinkwater, D. R. Sahoo, B. Long, and S. Subramanian, "Holographic acoustic elements for manipulation of levitated objects," *Nature communications*, vol. 6, p. 8661, 2015.

[15] https://www.bosch-presse.de/pressportal/de/en/ces-2017-the-internet-of-things-is-getting-personal-%E2%80%93-bosch-focuses-on-intelligent-assistants-83584.html.

[16] https://www.press.bmwgroup.com/global/article/detail/T0266649EN/the-bmw-group-at-ces-2017-in-las-vegas-bmw-holoactive-touch:-an-innovative-operating-concept-for-the-interior-of-the-future?language=en.

[17] M. Royer, J. Holmen, M. Wurm, O. Aadland, and M. Glenn, "Zno on si integrated acoustic sensor," *Sensors and Actuators*, vol. 4, pp. 357–362, 1983.

[18] Y. Kato, T. Sekitani, Y. Noguchi, T. Yokota, M. Takamiya, T. Sakurai, and T. Someya, "Large-area flexible ultrasonic imaging system with an organic transistor active matrix," *IEEE Transactions on Electron Devices*, vol. 57, no. 5, pp. 995–1002, 2010.

[19] W. Brown Jr, "Theory of conical sound radiators," *The Journal of the Acoustical Society of America*, vol. 13, no. 1, pp. 20–22, 1941.

[20] E. Wente, "A condenser transmitter as a uniformly sensitive instrument for the absolute measurement of sound intensity," *Physical Review*, vol. 10, no. 1, p. 39, 1917.

[21] W. Kuhl, G. Schodder, and F.-K. Schröder, "Condenser transmitters and microphones with solid dielectric for airborne ultrasonics," *Acta Acustica united with Acustica*, vol. 4, no. 5, pp. 519–532, 1954.

[22] M. I. Haller and B. T. Khuri-Yakub, "A surface micromachined electrostatic ultrasonic air transducer," *IEEE transactions on ultrasonics, ferroelectrics, and frequency control*, vol. 43, no. 1, pp. 1–6, 1996.

[23] A. Buhrdorf, L. Tebje, O. Ahrens, O. Glitza, and J. Binder, "Capacitive micromachined ultrasonic transducer (cmut) array for the frequency range below 500 khz," in *Ultrasonics Symposium, 2000 IEEE*, vol. 1. IEEE, 2000, pp. 915–918.

[24] D.-C. Pang and Y.-H. Chiang, "A transparent capacitive micromachined ultrasonic transducer (cmut) array for finger hover-sensing dial pads," in *Solid-State Sensors, Actuators and Microsystems (TRANSDUCERS), 2017 19th International Conference on*. IEEE, 2017, pp. 2171–2174.

[25] M.-W. Chang, H.-C. Deng, D.-C. Pang, and M.-Y. Chen, "6f-6 a novel method for fabricating sonic paper," in *Ultrasonics Symposium, 2007. IEEE*. IEEE, 2007, pp. 527–530.

[26] X. Zhuang, D.-S. Lin, Ö. Oralkan, and B. T. Khuri-Yakub, "Fabrication of flexible transducer arrays with through-wafer electrical interconnects based on trench refilling with pdms," *Journal of Microelectromechanical Systems*, vol. 17, no. 2, pp. 446–452, 2008.

[27] D.-C. Pang and C.-M. Chang, "Development of a novel transparent flexible capacitive micromachined ultrasonic transducer," *Sensors*, vol. 17, no. 6, p. 1443, 2017.

[28] H. Shinoda, T. Nakajima, K. Ueno, and N. Koshida, "Thermally induced ultrasonic emission from porous silicon," *Nature*, vol. 400, no. 6747, p. 853, 1999.

[29] M. Heath and D. Horsell, "Multi-frequency sound production and mixing in graphene," *Scientific reports*, vol. 7, no. 1, p. 1363, 2017.

[30] S. Aoyagi, Y. Kamiya, and S. Okabe, "Development of powerful airborne ultrasonic transmitter for robot metrology," *Japanese Journal of Applied Physics*, vol. 31, no. S1, p. 263, 1992.

[31] Y. Monnai, K. Hasegawa, M. Fujiwara, K. Yoshino, S. Inoue, and H. Shinoda, "Haptomime: mid-air haptic interaction with a floating virtual screen," in *Proceedings of the 27th annual ACM symposium on User interface software and technology*. ACM, 2014, pp. 663–667.

[32] Y. Makino, Y. Furuyama, S. Inoue, and H. Shinoda, "Haptoclone (haptic-optical clone) for mutual tele-environment by real-time 3d image transfer with midair force feedback," in *Proceedings of the 2016 CHI Conference on Human Factors in Computing Systems*. ACM, 2016, pp. 1980–1990.

[33] R. Takahashi, K. Hasegawa, and H. Shinoda, "Lateral modulation of midair ultrasound focus for intensified vibrotactile stimuli," in *International Conference on Human Haptic Sensing and Touch Enabled Computer Applications*. Springer, 2018, pp. 276–288.

[34] W. Frier, D. Ablart, J. Chilles, B. Long, M. Giordano, M. Obrist, and S. Subramanian, "Using spatiotemporal modulation to draw tactile patterns in mid-air," in *International Conference on Human Haptic Sensing and Touch Enabled Computer Applications*. Springer, 2018, pp. 270–281.

[35] T. Carter, S. A. Seah, B. Long, B. Drinkwater, and S. Subramanian, "Ultrahaptics: multi-point mid-air haptic feedback for touch surfaces," in *Proceedings of the 26th annual ACM symposium on User interface software and technology*. ACM, 2013, pp. 505–514.

[36] B. Long, S. A. Seah, T. Carter, and S. Subramanian, "Rendering volumetric haptic shapes in mid-air using ultrasound," *ACM Transactions on Graphics (TOG)*, vol. 33, no. 6, p. 181, 2014.

[37] S. Inoue, Y. Makino, and H. Shinoda, "Active touch perception produced by airborne ultrasonic haptic hologram," in *World Haptics Conference (WHC), 2015 IEEE*. IEEE, 2015, pp. 362–367.

[38] G. Korres and M. Eid, "Haptogram: ultrasonic point-cloud tactile stimulation," *IEEE Access*, vol. 4, pp. 7758–7769, 2016.

[39] H. E. Bass, L. C. Sutherland, A. J. Zuckerwar, D. T. Blackstock, and D. M. Hester, "Atmospheric absorption of sound: Further developments," *The Journal of the Acoustical Society of America*, vol. 97, no. 1, pp. 680–683, 1995. [Online]. Available: https://doi.org/10.1121/1.412989

[40] M. Ito, D. Wakuda, S. Inoue, Y. Makino, and H. Shinoda, "high spatial resolution midair tactile display using 70 khz ultrasound," in *International Conference on Human Haptic Sensing and Touch Enabled Computer Applications*. Springer, 2016, pp. 57–67.

[41] K. Hasegawa and H. Shinoda, "Aerial vibrotactile display based on multiunit ultrasound phased array," *IEEE Transactions on Haptics*, 2018.

[42] M. Bao, *Analysis and design principles of MEMS devices*. Elsevier, 2005, pp. 181–184.

[43] J. I. Seeger and S. B. Crary, "Stabilization of electrostatically actuated mechanical devices," in *Solid State Sensors and Actuators, 1997. TRANSDUCERS'97 Chicago., 1997 International Conference on*, vol. 2. IEEE, 1997, pp. 1133–1136.

[44] R. Puers and D. Lapadatu, "Electrostatic forces and their effects on capacitive mechanical sensors," *Sensors and Actuators A: Physical*, vol. 56, no. 3, pp. 203–210, 1996.

[45] E. S. Hung and S. D. Senturia, "Extending the travel range of analog-tuned electrostatic actuators," *Journal of microelectromechanical systems*, vol. 8, no. 4, pp. 497–505, 1999.

[46] M. A. Rosa, D. De Bruyker, A. R. Völkel, E. Peeters, and J. Dunec, "A novel external electrode configuration for the electrostatic actuation of mems based devices," *Journal of Micromechanics and Microengineering*, vol. 14, no. 4, p. 446, 2004.

[47] P. Mattila, J. Stor-Pellinen, J. Ignatius, J. Hietanen, and M. Luukkala, "Capacitive ultrasonic transducer with net backplate," *Measurement Science and Technology*, vol. 11, no. 8, p. 1119, 2000.

[48] S. T.Hayasaka, *ONKYOU SINDOU RON*. Maruzen Co.,Ltd., 1974, pp. 612–616.

[49] S. T.Hayasaka, *ONKYOU SINDOU RON*. Maruzen Co.,Ltd., 1974, p. 626.

[50] J. Bergqvist, "Finite-element modelling and characterization of a silicon condenser microphone with a highly perforated backplate," *Sensors and Actuators A: Physical*, vol. 39, no. 3, pp. 191–200, 1993.

[51] S. T.Hayasaka, *ONKYOU SINDOU RON*, 1974, pp. 734–735.

[52] S. T.Hayasaka, *ONKYOU SINDOU RON*, 1974, pp. 627–629.

[53] S. T.Hayasaka, *ONKYOU SINDOU RON*, 1974, p. 714.

Appendix A

Appendix: A prototype that triggered the research

This section describes the device with the parallel-plate structure, which can be fabricated by laminating flexible materials. First, generated sound pressure and energy efficiency in the structure are revealed by a physics model. Then, the evaluation of fabricated single transducer and an phased array device are described.

A.1 Physics model

Fig. A.1 shows the model consisted of the diaphragm with radius a[m], and air layer thickness with D[m]. The applied voltage between the diaphragm and the backplate electrode is a superposition of DC voltage V_0 [V] and AC voltage amplitude V_1 [V]. Note that the mechanical oscillation is axial symmetry, the model is a parallel-plate electrically with uniform charge in the diaphragm, and the fringing effect is ignorable.

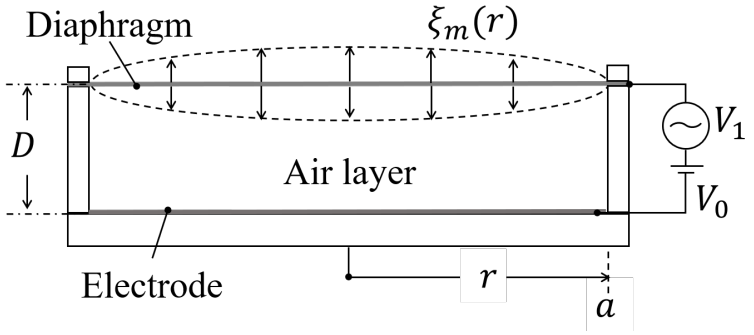

Figure A.1: Illustration of target physics model.

A.1.1 Generated sound pressure with Basic Structure

First, the author describes the generated sound pressure. The relationship between the ESF for operating the diaphragm P [N/m^2], and the electric displacement ξ_e [m] is expressed as

$$P = j\omega Z \Leftrightarrow \xi_e = \frac{P}{j\omega Z} \tag{A.1}$$

where Z is the sum of the acoustic impedance of the air $Z_a(= \rho c)$[(kg/m^3)(m/s)] and mechanical impedance of the target system Z_m[(kg/m^3)(m/s)]. The relationship between F and the accumulated electric charge is expressed as follows.

$$P = -\frac{(Q_0 + Q_1)^2 - Q_0^2}{2\varepsilon} = -\frac{Q_0^2 + 2Q_0Q_1}{2\varepsilon} \tag{A.2}$$

where Q_0 [C/m^2] is offset charge by V_0, Q_1 [C/m^2] is the varied charge by V_1, and ε[F/m] is the air permittivity. The relationship between the voltage applied to the structure, the accumulated electric charge, and the electrode distance is expressed as follows.

$$V_0 + V_1 = \frac{D + \xi_e}{\varepsilon}(Q_0 + Q_1) \tag{A.3}$$

From $V_0 = DQ_0/\varepsilon$ and Eq. (A.3), V_1 is expressed as

$$V_1 = \frac{1}{\varepsilon}(DQ_1 + \xi_e Q_0 + \xi_e Q_1) \tag{A.4}$$

Eq. (A.1) and Eq. (A.2), the relationship between the diaphragm displacement ξ_e and the electric charge Q_0, Q_1 as following.

$$\xi_e = \frac{-1}{j\omega\varepsilon Z}\frac{Q_1 + 2Q_0}{2\varepsilon}Q_1 \tag{A.5}$$

Eq. (A.4) and Eq. (A.5) lead the relationship between the V_1 and the electric charge including Q_0 and Q_1 as following.

$$V_1 = \frac{Q_1}{\varepsilon}\left\{D + \frac{-1}{j\omega Z}\frac{(Q_1 + 2Q_0)(Q_0 + Q_1)}{2\varepsilon}\right\} \tag{A.6}$$

Eq. (A.5) and Eq. (A.6) lead the relation equation between the V_1 and ξ_e as follows.

$$\begin{aligned}\xi_e &= \frac{-1}{j\omega\varepsilon Z}\frac{Q_1 + 2Q_0}{2\varepsilon}\frac{V_1}{\left\{D + \frac{-1}{j\omega Z}\frac{(2Q_0+Q_1)(Q_0+Q_1)}{2\varepsilon}\right\}} \\ &= \frac{2Q_0 + Q_1}{\omega Z\left\{\frac{(Q_0+Q_1)(2Q_0+Q_1)}{\omega\varepsilon Z} - j2D\right\}}V_1\end{aligned} \tag{A.7}$$

The generated sound pressure p_0 is obtained from Eq. (A.1) and Eq. (A.7), and is expressed as

$$p = j\omega\xi_e Z_a = \frac{Z_a}{Z}\frac{j(2Q_0 + Q_1)}{(\frac{(Q_0+Q_1)(2Q_0+Q_1)}{\omega\varepsilon Z} - j2D)}V_1 \tag{A.8}$$

At the same time, current I [A/m^2] flowing to the diaphragm is expressed as

$$\begin{aligned}I &= j\omega Q_1 \\ &= j\omega\frac{2Q_0 + Q_1}{\omega Z\left\{\frac{(Q_0+Q_1)(2Q_0+Q_1)}{\omega\varepsilon Z} - j2D\right\}}V_1 \\ &= 2\epsilon\omega\frac{V_1}{\omega Z\left\{\frac{(Q_0+Q_1)(2Q_0+Q_1)}{\omega\varepsilon Z} - j2D\right\}}\end{aligned} \tag{A.9}$$

Therefore, the electrical impedance Z_e is expressed as

$$Z_e = \frac{V_1}{I} = \frac{1}{2\omega\varepsilon}\left\{\frac{(Q_0 + Q_1)(2Q_0 + Q_1)}{\omega\varepsilon Z} - j2D\right\} \tag{A.10}$$

From Eq. (A.8), it is needed that the electro-acoustic energy conversion efficiency Z_a/Z is heightened in order to increase the generated sound pressure.

A.1.2 Electro-Acoustic Energy Conversion Efficiency

In this section, let obtain the electro-acoustic energy conversion efficiency Z_a/Z in Eq. (A.8), that is, obtain the mechanical impedance Z_m. Note that consider only the viscosity of the air layer and loss due to the heat conduction.

The equation of forced oscillation of the diaphragm and air layer are respectively given as follows[53].

$$\left(\nabla^2 - \frac{\sigma}{T}\lambda^2\right)\xi_m = \frac{p_b}{T} - \frac{P(r)}{T}e^{j\omega t} \tag{A.11}$$

$$\left\{\nabla^2 - \frac{\lambda}{\kappa}\Gamma\left(\beta\right)\right)\right\} p_b = -\frac{\lambda}{D}\Gamma(\beta)\xi_m \tag{A.12}$$

The boundary conditions at $r = a$ as follows

$$\begin{cases} \xi_m = 0 \\ \dfrac{\partial p_b}{\partial r} = 0 \end{cases} \tag{A.13}$$

where $\lambda = j\omega$, ω [rad/s] is angular frequency, σ [kg/m^2] is the surface density of the diaphragm, T [N/m] is the tension to the diaphragm, κ [kg/(m $\cdot$s^2)] is the bulk modulus of the air, $P(r)$[N/m] is driving force, ξ_m[m] is the mechanical displacement of the diaphragm, and p_b [Pa] is the pressure in the air layer when the diaphragm vibrates. ∇^2, β, $\Gamma\left(\beta\right)$ is expressed as follows

$$\nabla^2 = \frac{d^2}{dr^2} + \frac{1}{r}\frac{1}{dr} \tag{A.14}$$

$$\Gamma(\beta) = \frac{12\mu}{d^2}\frac{\beta^3 \sinh\beta}{12(2 - 2\cosh\beta + \beta\sinh\beta)} \tag{A.15}$$

$$\beta \equiv D\sqrt{\frac{\rho\lambda}{\mu}} \tag{A.16}$$

where β is the ratio of the mass effect and viscous effect in air layer, $\Gamma(\beta)$ is the braking action of the air layer. Now, let consider only the stationary component as the forced vibration solution. Let each solution of ξ_m, p_b be as follows

$$\xi_m = \sum_m B_m J_0(\alpha_m y)\, e^{\lambda t} \tag{A.17}$$

$$p_b = \sum_n D_n J_0(\alpha_n y)\, e^{\lambda t} \tag{A.18}$$

where $y \equiv \frac{r}{a}$, α_m is 0-th order root of the bessel function of the first kind, and α_n is 1-th order root of the bessel function of the first kind. Let expand distribution of $F(r)$ be as follows

$$F(r) = \sum_m A_m J_0(\alpha_m y) \tag{A.19}$$

When the driving force uniformly acts on the diaphragm, the expansion coefficient A_m is given as

$$A_m = \frac{2F}{\alpha_m J_1(\alpha_m)} \tag{A.20}$$

Of the various modal partial vibrations occur in the system, let pay attention only to the fundamental mode vibration component corresponding to $m = n = 1$. Based on the above, organization of Eq. (A.11) and Eq. (A.12) leads respectively as follows

$$\left(-\frac{\alpha_{m1}^2}{a^2} - \frac{\sigma}{T}\lambda^2\right) B_1 J_0(\alpha_{m1} y) = \frac{1}{T} D_1 j_0(\alpha_{n1} y) - \frac{1}{T} A_1 J_0(\alpha_{m1} y) \tag{A.21}$$

$$\left(\frac{\alpha_{n1}^2}{a^2} - \frac{\lambda}{\kappa}\Gamma(\beta)\right) D_1 J_0(\alpha_{n1} y) = -\frac{\lambda}{D}\Gamma(\beta) B_1 J_0(\alpha_{m1} y) \tag{A.22}$$

Applying the coefficient B_1 and D_1 obtaining from Eq. (A.21) and Eq. (A.22) to the Eq. (A.17) and Eq. (A.18) leads each solution as follows

$$\xi_m = \frac{\left\{ \frac{{\alpha_{n1}}^2}{a^2} + \frac{\lambda}{\kappa}\,(\beta) \right\}}{\left(T\frac{{\alpha_{m1}}^2}{a^2} + \sigma\lambda^2 \right)\left\{ \frac{{\alpha_{n1}}^2}{a^2} + \frac{\lambda}{\kappa}\,(\beta) \right\} + \frac{\lambda}{D}\,(\beta)} A_1 J_0(\alpha_{m1} y) e^{\lambda t} \tag{A.23}$$

$$p_b = \frac{\frac{\lambda}{D}\,(\beta)}{\left(T\frac{{\alpha_m}^2}{a^2} + \sigma\lambda^2 \right)\left\{ \frac{{\alpha_{n1}}^2}{a^2} + \frac{\lambda}{\kappa}\,(\beta) \right\} + \frac{\lambda}{D}\,(\beta)} A_1 J_0(\alpha_{m1} y) e^{\lambda t} \tag{A.24}$$

Assuming that the air layer thickness is sufficiently thin and $|\frac{\beta^2}{10}| << 1$, $\Gamma(\beta)$ can be approximated to $\frac{12\mu}{D^2}$. Therefore, the velocity distribution $\dot{\xi_m}$ is given as follows

$$\dot{\xi_m} = \frac{1}{\frac{1}{\lambda C_1} + M_1\lambda + \frac{1}{\lambda c_1 + \frac{1}{r_1}}} A_1 J_0(\alpha_{m1} y) e^{\lambda t} \tag{A.25}$$

Note that

$$\begin{cases} C_1 = \dfrac{a^2}{T{\alpha_{m1}}^2} \\ M_1 = \sigma \\ c_1 = \dfrac{D}{\kappa} \\ r_1 = \dfrac{12\mu a^2}{{\alpha_{n1}}^2 D^3} \end{cases} \tag{A.26}$$

From the above, the mechanical impedance Z_m is expressed as

$$Z_m = \frac{F\,(r)}{\dot{\xi_m}} = \frac{1}{\lambda C_1} + \lambda M_1 + \frac{1}{\lambda c_1 + \frac{1}{r_1}} = Z_{mf} + Z_{ma} \tag{A.27}$$

Note that

$$\begin{cases} Z_{mf} = \dfrac{1}{\lambda C_1} + \lambda M_1 \\ Z_{ma} = \dfrac{1}{\lambda c_1 + \frac{1}{r_1}} \end{cases} \tag{A.28}$$

Fig. A.2 shows the equivalent circuit of the element. In order to generate ultrasound with high efficiency, $Z_m \to 0$ is desirable. where Z_{mf} is the impedance determined by the state of the diaphragm, which depends on the film to be used and the tension applied to it. The

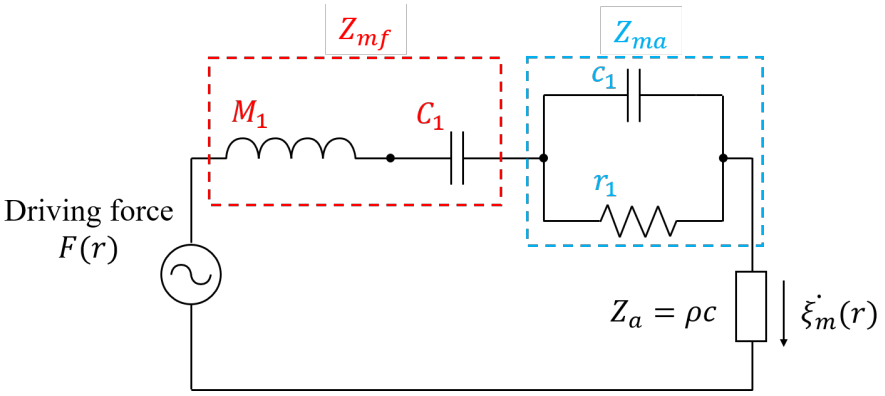

Figure A.2: Equivalent circuit model for the physics model of Fig. A.1.

tension T required for the diaphragm at resonance is given as follows

$$T = \sigma \left(\omega \frac{a}{\alpha_{m1}} \right)^2 = \sigma \left(2\pi f \frac{a}{\alpha_{m1}} \right)^2 \tag{A.29}$$

Z_{ma} is the impedance value determined by the state of the air layer, which is composed of resistance component due to the air viscosity and the air stiffness. The resistance component due to the air viscosity can be closed to 0 by adjusting a and D. The energy loss due to the thermal conduction is determined by the bulk modulus κ constituting of the air stiffness. κ relates to the speed of volume change of the gas and an exothermic phenomenon occurs when the gas is compressed. The bulk modulus of the air κ which is trapped in the thin air layer is given as

$$\kappa \equiv \gamma P_{a_0} \frac{1}{1 + \frac{\gamma - 1}{\chi} \frac{e^{\chi} - e^{-\chi}}{e^{\chi} + e^{-\chi}}} \tag{A.30}$$

Note that,

$$\chi = \frac{D}{2} \sqrt{\frac{j\omega\gamma}{\upsilon}} \tag{A.31}$$

where γ is the ratio of the specific heat at the constant pressure to the specific heat at the constant volume, $\nu[\mathrm{m}^2/\mathrm{s}]$ is the thermometric conductivity. Since imaginary part in Eq. (A.30)means the energy loss due to thermal conduction, D is decided in order to the imaginary part.

A.1.3 Numerical Calculation

In order to determine actual fabricating conditions, the author conducted a numerical calculation based on the theoretical formula under the conditions shown in Table A.1. The resonant frequency was from 40 kHz to 100 kHz in the step of 10 kHz. Assuming that the diaphragm was 5 nm of gold-sputtered 12 μm-thick aramid film and had a radius of 3.2 mm, which was used for actual fabrication. In addition, the tension T was assumed to be applied with tension determined by Eq. (A.29) at each frequency.

Fig. A.3 and Fig. A.4 show the energy conversion efficiency and the energy loss by heat conduction respectively. From these results, the air layer thickness was decided to 100 μm.

Table A.1: Conditions of each parameter used for numerical calculation

Aramid film density [kg/m^3]	1.5×10^{3}
Surface density of diaphragm [kg/m^2]	18×10^{3}
Density of gold [kg/m^3]	19.3×10^{3}
Surface density of gold [kg/m^2]	96.5×10^{-6}
Radius of diaphragm a [m]	3.2×10^{-3}
0th order root of bessel function of the first kind α_{m1}	2.405
1th order root of bessel function of the first kind α_{n1}	3.8317
Air temperature [°C]	20
Air density ρ [kg/m^3]	1.204
Thermal conductivity of air ν [m^2/s]	21.24
Viscosity coefficient of air μ [kg/ (m $\cdot$ s)]	18.23×10^{-6}
Ratio of specific heat at constant pressure to that at constant volume γ	1.3986
Atmospheric pressure p_a [pa]	101.3×10^{3}

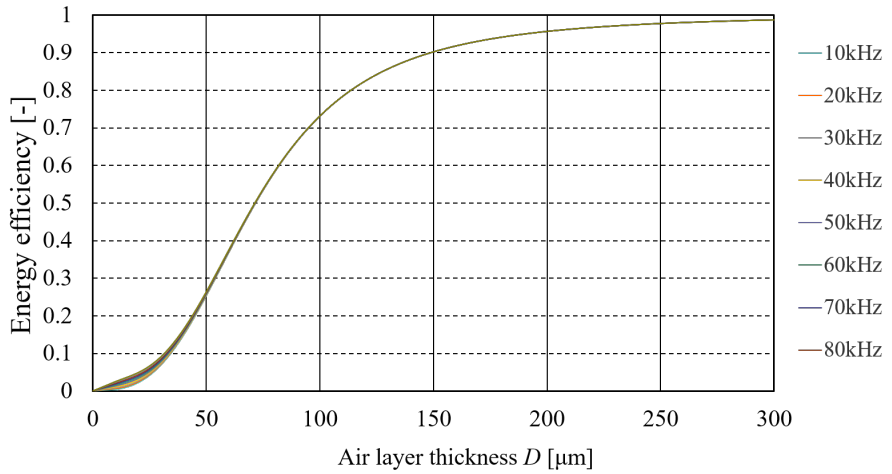

Figure A.3: Numerical calculation result about the loss by heat conduction against the air layer thickness D

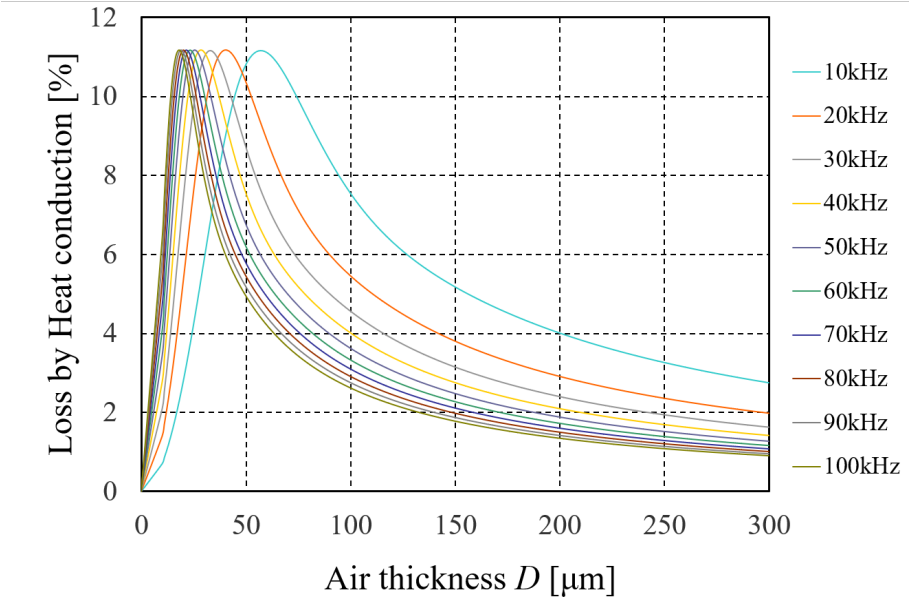

Figure A.4: Numerical calculation result about the loss by heat conduction against the air layer thickness D

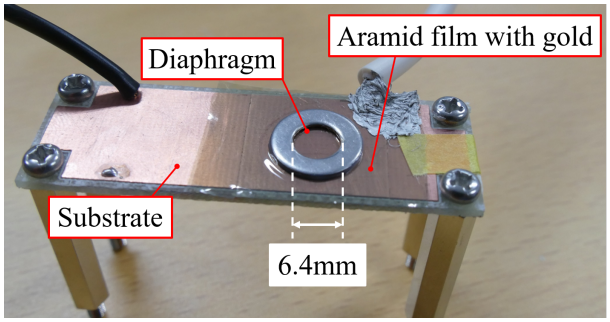

Figure A.5: Photograph of the fabricated transducer.

A.2 Evaluation of Single Element

Fig. A.5 shows the actual appearance of fabricated single element. The diaphragm was 5 nm of gold-sputtered 12 μm-thick aramid film (Mictron, TORAY INDUSTRIES, INC.). The film was applied tension in the range where the film does not tear. The thickness of the air layer between the diaphragm and the substrate was 100 μm and the diameter of the movable part was 6.4 mm. The author investigated the frequency characteristic by measuring sound pressure. The author used a standard microphone (4138-A015, Bruel & Kjaer) with an amplifier (NEXUS Conditioning Amplifier, Bruel & Kjaer) and obtained the numerical RMS value visually read on the oscilloscope (TDS 2001C, Tektronix Inc.). The microphone was hung at 10 cm above the prototype transducer. Fig. A.6 shows the experimental result about the frequency characteristic when V_0 = 420 V, V_1= 20 V was applied. The results suggests that the resonant frequency of the prototype was around 40 kHz. Fig. A.7 shows the numerical calculation result of the frequency characteristic based on theoretical equation when the resonant frequency was 40 kHz under the same conditions in the experiment. Thus, the experimental results similar to that of the theory in the spectral waveform were obtained. However, the observed value was about 1/10 smaller than the simulation value, even considering the energy diffusion by the spherical wave. This cause was due to the filter setting of the amplifier connected to the microphone.

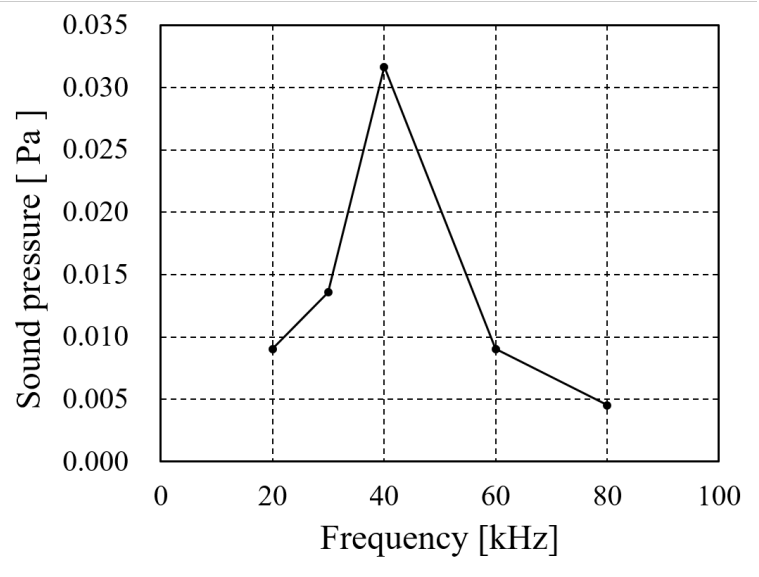

Figure A.6: Obtained frequency characteristics of the prototype transducer.

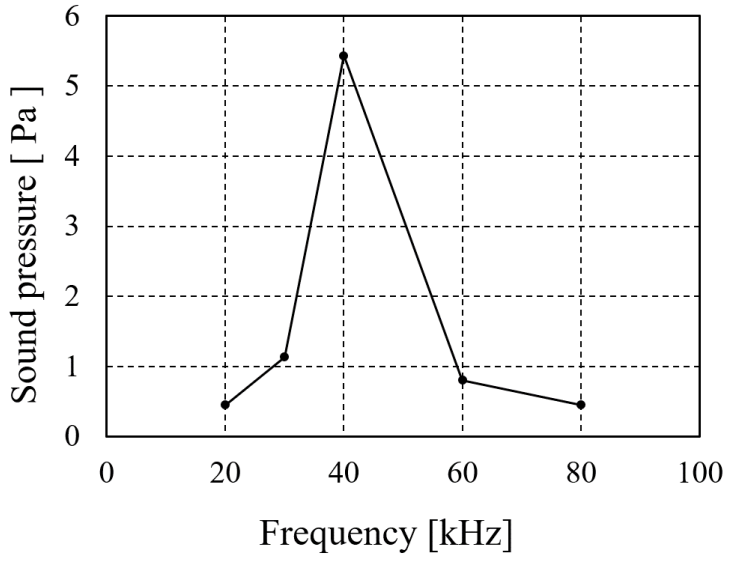

Figure A.7: Numerical calculation result of frequency characteristics based on Eq. (A.8)

A.3 Prototype phased array device with parallel-plate structure

From the section A.2, it was found that an single element can be fabricated by laminating flexible materials. Then, the author confirmed whether the proposed method can realize a phased array device. As a prototype, we fabricated an 8×8 phased array integrated with electrical circuit driving each element. Note that the diaphragm was not applied tension to vibrate at the intended frequency.

Fig. A.8 shows the actual appearance of the prototype and Fig. A.9 shows a cross-section of the device. The diaphragm is commonly supplied with DC voltage V_0 and emits ultrasound into the air is driven by the ESF generated by AC voltage V_1 ($\ll V_0$) applied between the top and the bottom substrate. The device thickness is 1.3 mm including the following three parts: a stainless-steel frame, a vibrating membrane, and a substrate. These parts are fixed with 100-μm-thick adhesive sheets (Nitoms, Inc., T284). The vibrating diaphragm is a gold-sputtered 12.5-μm-thick polyimide film (DU PONT-TORAY CO., LTD., Kapton). The air layer thickness D is 100 μm. To individually control each element, separate square conductor patches are formed on the upper side of the substrate. The size of each patch is 1 cm×1 cm, and electrode interval is 0.6 mm as shown in Fig. A.10. Each driver circuit to generate AC voltage of amplitude V_1 is directly implemented on the lower side of the substrate at each corresponding transducer patch as shown in Fig. A.10. Fig. A.11 shows the composition of driver circuit for single element. V_1 is generated by switching Nch MOSFET. The input signal to the gate of MOSFET generated in MCU, which determines the phase difference ϕ_N in Fig. A.9. By shifting phase ϕ_N of each element, the device creates a focal point in the air. The program to send the input signal is written in MCUs in advance and driving is started by an external trigger as shown in Fig. A.12.

The author measured sound pressure distribution to observe a focal point of ultrasound. The center of the device was the measurement system origin O (x, y, z) = (0, 0, 0 mm). We measured two-dimensional (x-y plane) sound pressure distribution 50 mm above the device using a microphone (4138-A015, Bruel & Kjaer) when the prototype device was driven to

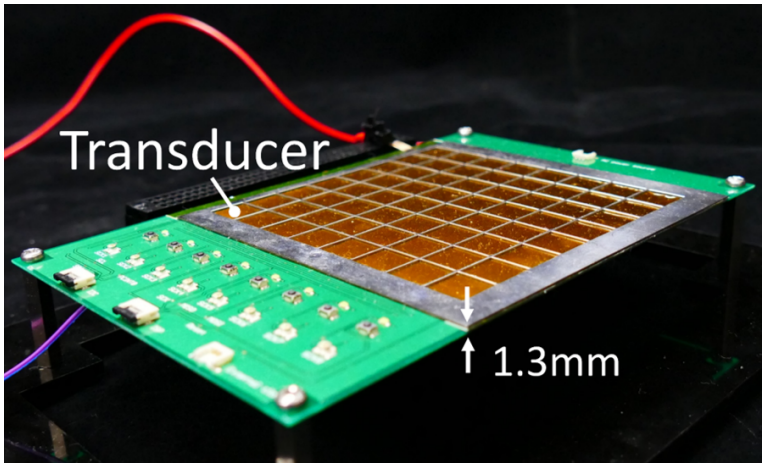

Figure A.8: Photograph of the prototype device.

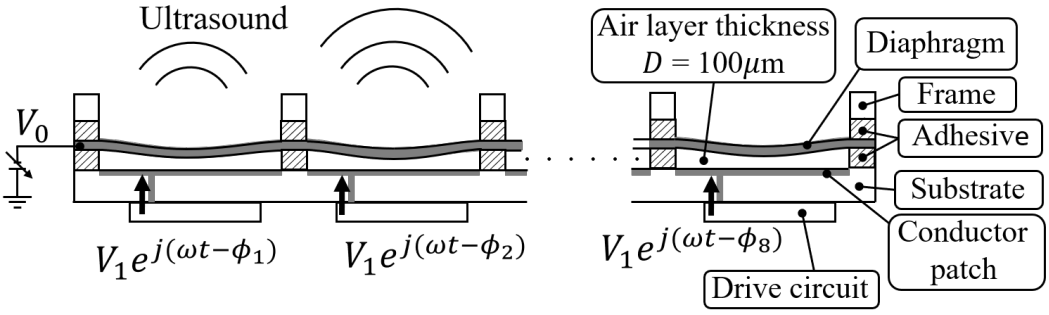

Figure A.9: A cross-sectional diagram of the 8 8 phased array prototype. The variables ω, t, N, ϕ_N respectively mean frequency, time, the number of elements and phase difference.

make a focus at a point $(x,\ y,\ z) = (0,\ 0,\ 50\,\text{mm})$. In the 64-element array, we used 53 elements excluding 11 defected elements that did not generate detectable ultrasound in a preliminary inspection experiment as shown in Fig. A.14. The applied voltage V_0 and V_1 were $-400\,\text{V}$ and $5\,\text{V}$ respectively, and drive frequency was $40\,\text{kHz}$.

Fig. A.15 shows the experimental result. The sound pressure was maximized at the intended focal point, $(x,\ y) = (0,\ 0\,\text{mm})$, and was $2.6\,\text{Pa}$. Some unexpected sidelobes were also generated. The reason for these sidelobes would be the absence of some waves that would deconstructively interfere with the lobes, due to the defected elements. To generate sound pressure as same as the existing AUTD, about 120,000 elements will be required under the same drive conditions as the above experiment.

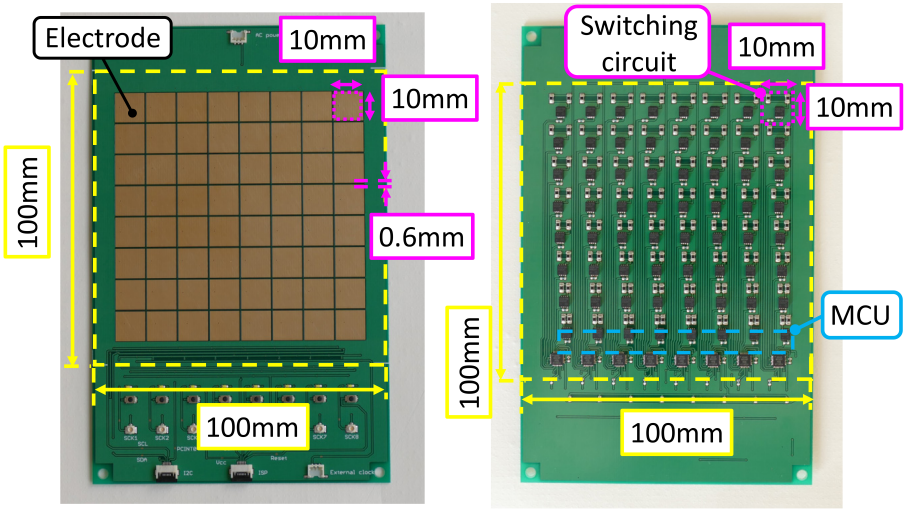

Figure A.10: Photograph of substrate for the prototype device. The left is upper side of the substrate and the right is lower side of the substrate.

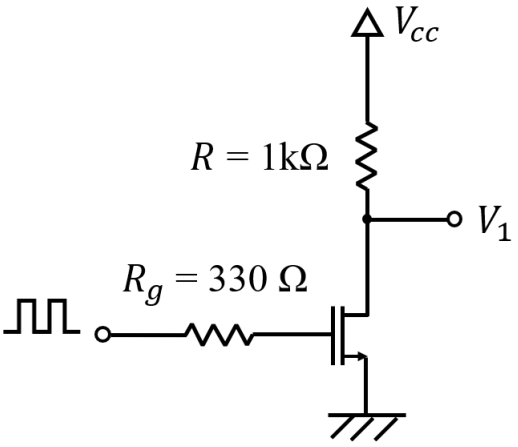

Figure A.11: The drive circuit configuration of each element.

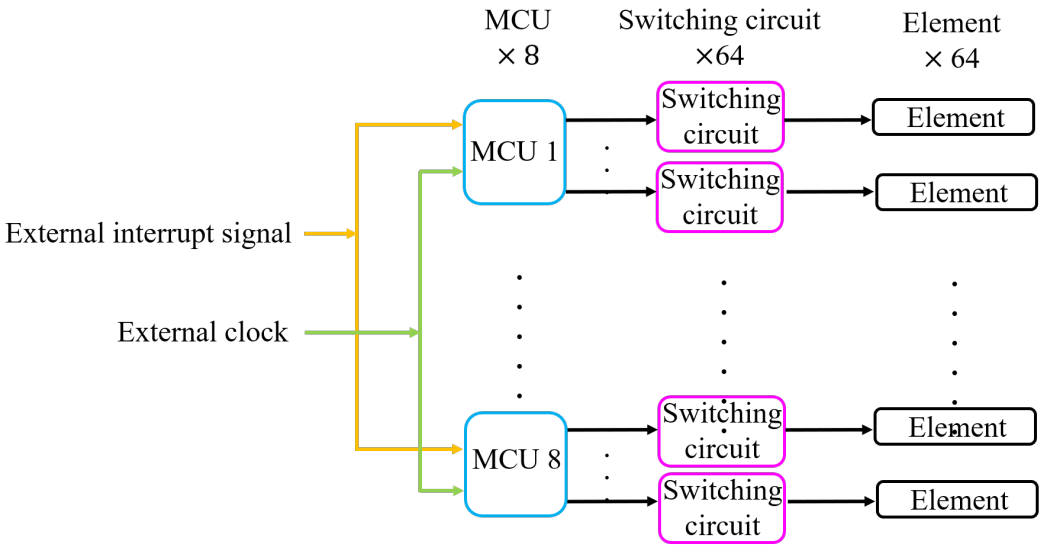

Figure A.12: The flowchart to drive each transducer.

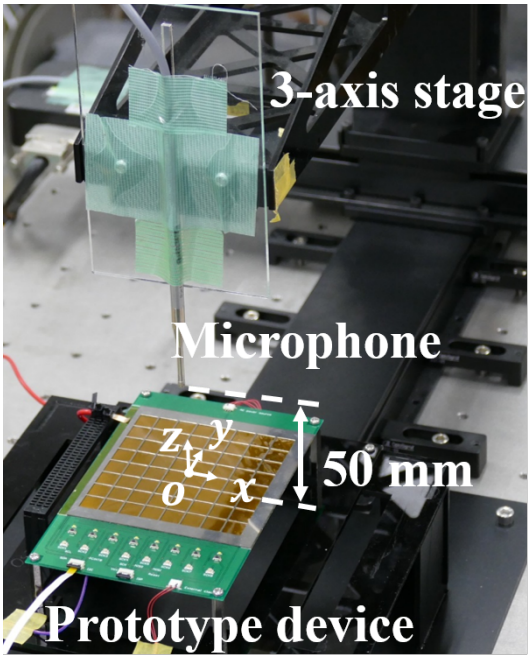

Figure A.13: Experimental setup for measuring sound distribution.

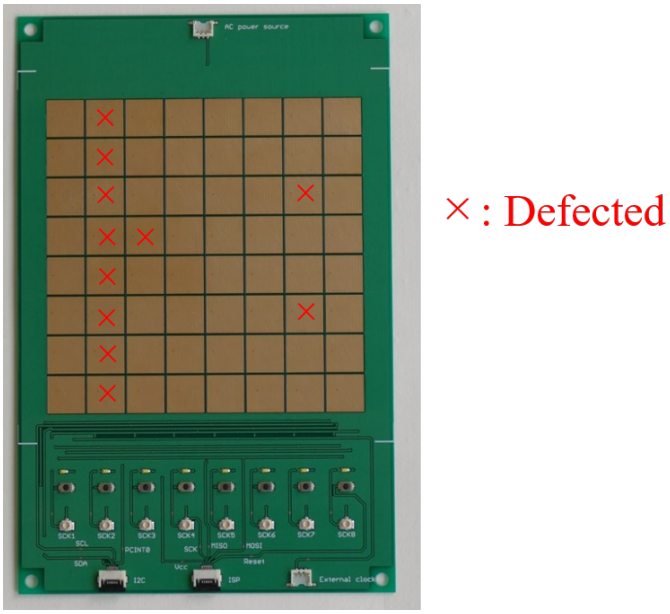

Figure A.14: Defected elements in the prototype device due to break MCU.

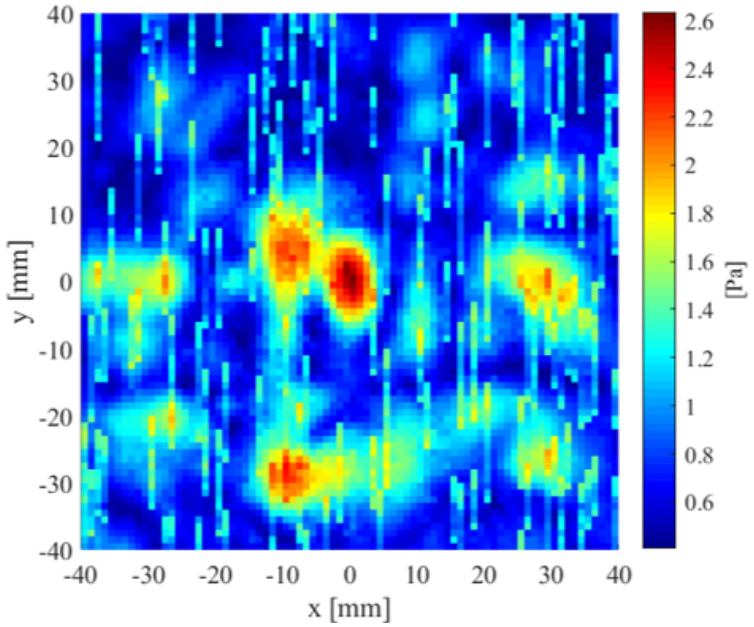

Figure A.15: Measured sound pressure distribution at z =50 mm, when the device was driven to generate a focus at (x, y, z) = (0, 0, 50 mm).